

# **A novel non-invasive optical method for quantitative visualization of pH and oxygen dynamics in soils**

Kumulative Dissertation zur Erlangung des Doktorgrades der Naturwissenschaften

(Dr. rer. nat.)

Wissenschaftsdisziplin Geoökologie

der Mathematisch – Naturwissenschaftlichen Fakultät

der Universität Potsdam



vorgelegt von

**Dipl. Ing. Nicole Rudolph-Mohr**

Potsdam, im März 2013

Published online at the  
Institutional Repository of the University of Potsdam:  
URL <http://opus.kobv.de/ubp/volltexte/2013/6699/>  
URN <urn:nbn:de:kobv:517-opus-66993>  
<http://nbn-resolving.de/urn:nbn:de:kobv:517-opus-66993>

## Table of contents

Content .....	i
Summary .....	iv
Zusammenfassung .....	v
<b>1. General introduction .....</b>	<b>1</b>
1.1. Thematic context and motivation .....	2
1.2. State of the art .....	5
1.2.1. Imaging in soil science .....	5
1.2.2. Optical imaging using sensors .....	8
1.3. Objectives and thematic structure of the thesis .....	15
<b>2. Spatio-temporal mapping of local soil pH changes induced by roots of lupin and soft-rush .....</b>	<b>23</b>
2.1. Introduction .....	24
2.2. Material and methods .....	26
2.2.1. Fluorescence sensor imaging .....	26
2.2.2. Plant growth experiments .....	29
2.3. Results .....	30
2.3.1. Sensor calibration .....	30
2.3.2. Root growth .....	31
2.3.3. Dynamics of soil pH around the roots .....	32
2.3.4. Variation in pH along the root length .....	33
2.3.5. Temporal variability in near-root pH .....	34
2.3.6. Rhizosphere pH dynamics in narrow-leaved lupin .....	35
2.4. Discussion .....	36
<b>3. Dynamic oxygen mapping in the root zone by fluorescence dye imaging combined with neutron radiography .....</b>	<b>42</b>
3.1. Introduction .....	44
3.2. Material and methods .....	46
3.2.1. Fluorescence oxygen imaging .....	46
3.2.2. Neutron radiography .....	48
3.2.3. Experimental set-up .....	50

3.3. Results .....	53
3.3.1. Homogeneous porous media .....	53
3.3.2. Homogeneous porous media with plant roots .....	54
3.3.3. Layered porous media with plant roots .....	57
3.4. Discussion .....	59
3.5. Conclusions .....	62
<b>4. Simultaneous visualization of oxygen depletion zones and water content distribution in artificial soil structures .....</b>	<b>66</b>
4.1. Introduction .....	67
4.2. Material and methods .....	69
4.2.1. Fluorescence imaging .....	69
4.2.2. Kinetics of pyrogallol autooxidation .....	71
4.2.3. Experimental description .....	72
4.3. Results and discussion .....	74
4.4. Conclusions .....	78
<b>5. Coupled denitrification and anaerobic biodegradation monitored using nitrate- sensitive fluorescence imaging .....</b>	<b>83</b>
5.1. Introduction .....	84
5.2. Experimental section .....	85
5.2.1. Preparation of the nitrate-sensitive membrane .....	85
5.2.2. Growth medium and inoculums .....	86
5.2.3. Set up and operation of the flow cell .....	86
5.2.4. Chemical analyses .....	86
5.2.5. Fluorescence imaging of nitrate .....	87
5.2.6. Nitrate tracer calibration .....	87
5.2.7. Reactive transport modeling .....	88
5.2.8. Biological analyses .....	89
5.3. Results and discussion .....	90
5.3.1. Chemical analyses at sample ports .....	90
5.3.2. Nitrate concentration in the flow cell .....	90
5.3.3. Numerical simulations .....	92
5.3.4. Microbial analysis .....	93

5.3.5. Microbial community structure .....	94
5.3.6. Extent and character of anaerobic biodegradation .....	95
5.3.7. Potential of RBOE as a nitrate sensor .....	96
5.4. Conclusions .....	97
<b>6. General discussion and conclusions .....</b>	<b>101</b>
6.1. General remarks .....	102
6.2. Evaluation of the fluorescence imaging method .....	103
6.3. Outlook .....	105
6.3.1. Sensor improvements .....	105
6.3.2. Applications currently tested .....	106
6.4. Synthesis .....	107
<b>C0Spatio-temporal mapping of local soil pH changes induced by roots of lupin and soft-rush – Supporting information .....</b>	<b>109</b>
Curriculum Vitae .....	113
Danksagung .....	114

## Summary

In soils and sediments there is a strong coupling between local biogeochemical processes and the distribution of water, electron acceptors, acids and nutrients. Both sides are closely related and affect each other from small scale to larger scales. Soil structures such as aggregates, roots, layers or macropores enhance the patchiness of these distributions. At the same time it is difficult to access the spatial distribution and temporal dynamics of these parameter. Noninvasive imaging techniques with high spatial and temporal resolution overcome these limitations. And new non-invasive techniques are needed to study the dynamic interaction of plant roots with the surrounding soil, but also the complex physical and chemical processes in structured soils. In this study we developed an efficient non-destructive *in-situ* method to determine biogeochemical parameters relevant to plant roots growing in soil. This is a quantitative fluorescence imaging method suitable for visualizing the spatial and temporal pH changes around roots. We adapted the fluorescence imaging set-up and coupled it with neutron radiography to study simultaneously root growth, oxygen depletion by respiration activity and root water uptake. The combined set up was subsequently applied to a structured soil system to map the patchy structure of oxic and anoxic zones induced by a chemical oxygen consumption reaction for spatially varying water contents. Moreover, results from a similar fluorescence imaging technique for nitrate detection were complemented by a numerical modeling study where we used imaging data, aiming to simulate biodegradation under anaerobic, nitrate reducing conditions.

## **Zusammenfassung**

In Böden und Sedimenten sind biogeochemische Prozesse und die Verteilung von Größen wie Wasser, Elektronenakzeptoren, Säuregehalte und Nährstoffe in enger Weise miteinander gekoppelt. Diese wechselseitige Beeinflussung ist skalenübergreifend und reicht von sehr kleinen bis zu größeren Skalen. Die in realen Böden vorhandene Struktur z. Bsp. Aggregate, Pflanzenwurzeln, Schichten und Makroporen bedingen eine starke räumlich Heterogenität und zeitliche Dynamik dieser Größen. Gleichzeitig sind Verteilung und Dynamik sehr schwer zu beobachten, zumindest ohne ihre gleichzeitige Störung. Bildgebende Verfahren bieten eine sehr gute räumliche und zeitliche Auflösung und ermöglichen die Darstellung dieser Größen. Um die dynamische Wechselwirkung zwischen Pflanzenwurzeln und Boden, aber auch die komplexen physikalisch – chemischen Prozesse in Böden zu verstehen, sind neue bildgebende Verfahren notwendig. Ziel dieser Arbeit war es, eine neue nicht-invasive Methode zu entwickeln, die es ermöglicht biogeochemische Parameter in der Wurzelzone zu visualisieren. Innerhalb dieser Studie wurde ein quantitatives bildgebendes Verfahren entwickelt, das die räumlichen und zeitlichen Dynamiken des pH Wertes in der Rhizosphäre erfasst. Diese auf Fluoreszenzemissionen basierende Methode wurde ebenso für Sauerstoffdetektion entwickelt und mit Neutronen Radiographie kombiniert um gleichzeitig Aussagen über Wurzelwachstum, Sauerstoffzehrung durch Wurzelatmung und Wurzelwasseraufnahme treffen zu können. Die kombinierte bildgebende Methode wurde dann in einem künstlichen Boden genutzt um Nischen und Übergangsbereiche von Sauerstoff bei variierenden Wassergehalten zu charakterisieren. Das große Potential von bildgebenden Verfahren zeigt sich bei Modellierungsstudien. In dieser Studie wurden Bilddaten als Eingabeparameter für die Simulierung von denitrifizierendem biologischem Schadstoffabbau genutzt.





# Chapter 1

## General introduction

*This cumulative PhD thesis presents a new approach in monitoring biogeochemical variables in the soil continuum. The variables include oxygen, pH, and soil water content. Especially in the root zone of plants, these variables are highly dynamic and interrelated: For example, high water content may cause reduced oxygen supply due to slower oxygen diffusion in the water filled pore space. Therefore, it is of high interest to non-invasively map these quantities simultaneously. In this thesis work, I developed and applied new imaging methods for mapping these parameters in dynamic regions with a high spatial and temporal resolution. Dynamic regions of interest were the soil – plant root interface and the heterogeneity of soil with focus on the influence of aggregation and layering on diffusive oxygen transport mechanisms. The imaging set up includes a novel fluorescence imaging method but also a combination of fluorescence imaging and neutron radiography which was done for the first time.*

*The first introductory chapter addresses the thematic context of the thesis and starts with outlining the motivation. A brief summary about the importance of oxygen, pH and water content measurements in soil science follows. I will give an overview of the non-invasive imaging techniques applicable to soil and soil - plant systems. The overview is continued by a detailed description of fluorescence imaging including possible applications and how and why it works. The chapter closes with a short description of the main ideas that define the thematic structure of this thesis.*

**Keywords:** *biogeochemical parameter, fluorescence, optical imaging, soil heterogeneity*

## 1.1 Thematic context and motivation

Soil is a complex medium with high spatial and temporal environmental variability at a wide range of scales. Soils develop as a critical zone between the biosphere, hydrosphere, atmosphere, and lithosphere (Rennert et al. 2012). The different contacting organic, inorganic, and biological components define a complex and large biogeochemical interface (BGI) to the soil's liquid and gaseous phases (Young and Crawford 2004). This BGI is three-dimensional of varying thickness and continuously transformed by the interplay of soil biota (Totsche et al. 2012). Biogeochemical interfaces in soil can exhibit biological, chemical and physical gradients concerning from a scale of nanometers to decimeters. These gradients affect processes in soil, e.g. water retention (Whalley et al. 2005), or root growth (Hinsinger et al. 2009). In 2007, the German Research Foundation (DFG) has addressed the need of an intensive research on the architecture of biogeochemical interfaces in soils and on the complex interplay and interdependencies of chemical, biological, and physical processes on BGI's by establishing the Priority Program SPP 1315 "Biogeochemical Interfaces in Soil" (Totsche et al. 2010). Understanding and visualization the architecture of biogeochemical interfaces in soil have been identified as emerging challenge in soil science (Totsche et al. 2010). The present work is part of this DFG Priority Program and addresses different biogeochemical interfaces with focus on developing new imaging techniques able to visualize them and their dynamic character. This work focuses on (1) BGI's formed by the interplay of soil structure, oxygen and water content distribution at the scale of mm and cm. Aggregates and layers are of major interest because they partly control the spatial distribution and bioavailability of solutes and gases in soil (Totsche et al. 2012) and (2) BGI's built at the root – soil interface. This area is highly dynamic in space and time due to the interrelated pattern of root respiration, root exudation and root water uptake (Gregory & Hinsinger 1999, Wenzel 2001).

Soil structure or spatial heterogeneity dominates almost all properties of soils and hence, its functioning (Dexter 1997). Aggregates, layers, preferential flow paths, macro pores of former root channels, active plant roots, and wettability differences creating soil structure and influencing each other. Mechanical impedance in compacted soils for example slowly decreases root elongation rates (Handbury & Atwell 2005). Besides, compacted soil, aggregates, and layer of finer grained material are more susceptible to waterlogging after rain events, and hypoxia is likely to limit root growth (Bengough et al. 2011). plants change their rhizosphere properties. Moradi et al. (2012) showed that polymeric substances released by lupin roots increased water repellency in the rhizosphere. In turn, soil wettability affects

hydrological processes like infiltration or preferential flow (Goebel et al. 2004). In more detail, especially aggregates and layers are important structural features. Soils, even sandy soils with some salts tend to form aggregates (Horn & Peth 2009). Aggregation is crucial for the movement of water, gas and solutes because it enhances soil aeration, infiltration and storage of water (Carminati et al. 2008). Aggregate formation occurs during swelling and shrinking (Horn & Peth 2009) and is basically the conglomeration of soil particles that are bound together by physical, chemical and biological processes (Horn & Schmucker 2005). Under normal conditions, water is stored by capillarity within aggregates and layers. This waterlogging may impair oxygen supply in the inner part of the aggregates and layers and affect the biological activity and mineralization of plant nutrients (Lipiec et al. 2007). Moreover, oxygen diffusion to sinks (soil microbial respiration or plant root respiration) takes place in the interaggregate pores and is controlled by the concentration gradients resulting from respiration (Horn & Peth 2009). The limited oxygen transport in the inner parts of the aggregates is due to the higher water content and therefore limited diffusion. Soils with strong layering show similar behavior, the change from finer pores to larger pores produce layered water distribution patterns (Oswald et al. 2008). Furthermore, the occurrence of layers with lower diffusivity only few centimetres thick have been reported to reduce gas diffusion fluxes by several orders of magnitude (Kristensen et al. 2010). These examples indicated the necessity to measure water content and oxygen distribution simultaneously.

Roots are of great importance with strong effects on soil structure and the distribution

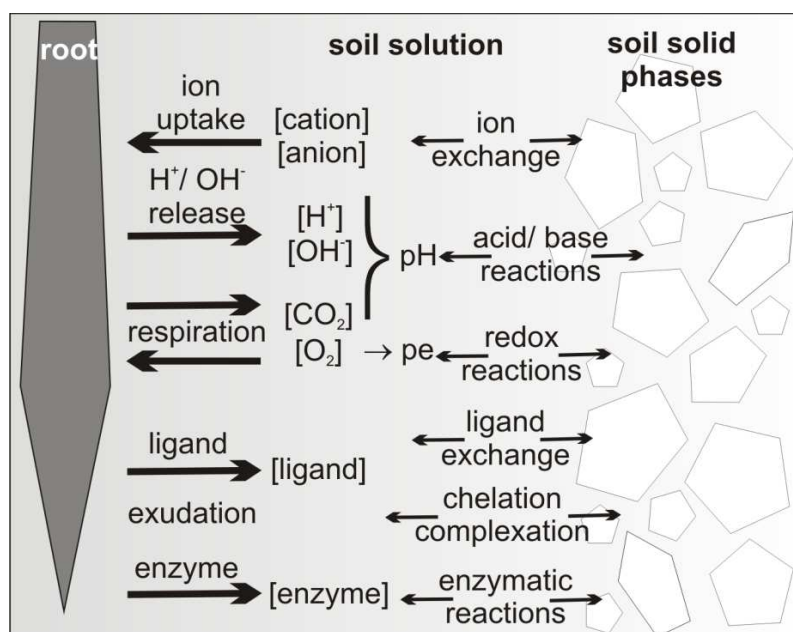


Figure 1: Schematic representation of root functions involved in changes in physical properties occurring in the rhizosphere (Hinsinger et al., 2005)

of biogeochemical parameters. Specific flora covering the land is a major determining factor of soil wettability due to changes in litter amount and composition, root development, and associated rhizospheric organisms (Eynard et al. 2006) which in turn affects soil structure. Two main biogeochemical parameters influenced by

plant roots are soil oxygen concentration and soil pH. Oxygen is a sensitive parameter in terms of root growth because low oxygen values decrease root elongation (Hanbury & Atwell 2005). In oxygen deficient environments there may be a trade-off between root morphology and physiology to balance the need for nutrient and water capture and retain adequate oxygen supply to the root system for root function (Hodge et al. 2009). Highlighting the soil oxygen distribution, root/rhizosphere respiration can account for as little as 10% to greater than 90% of total in situ soil respiration depending on vegetation type and season of the year (Hanson et al. 2000). However, respiration is a primary function which can substantially impact soil pH due to the subsequent increase in soil CO<sub>2</sub> (Hinsinger et al. 2009). Rhizosphere pH has been reported to be up to 1 – 2 pH units below or above bulk soil pH (Blossfeld & Gansert 2007, Hinsinger et al. 2003). However, most of the literature on spatial pH changes in the rhizosphere has been conducted under rather artificial conditions by using agar gels or hydroponic solutions and still the temporal component has been poorly documented (Hinsinger et al. 2009). This lack of information highlights the requirements to research approaches (1) the need of new non-destructive *in situ* imaging techniques (2) the reversibility of the imaging method to capture the spatiotemporal heterogeneity and (3) the need to observe the response of the root - soil interface under more realistic or real soil conditions.

Heterogeneity in soil is a general feature with influences on physical, chemical and biological properties which enhances the patchiness of biogeochemical parameters like oxygen, pH and water content. The impact of soil structure, how it controls or modulates the distribution, flow and retention of water, solutes, gases and biota, in agricultural and natural ecosystems, is relatively unquestioned (Young et al. 2001). Since most of these processes are dynamic non-destructive, non-invasive methods to observe them are desirable. Moreover, due to the destructive character of conventional methods, it is difficult to assess the spatial and temporal dynamics of the variables of interest. Blossfeld and Gansert (2007) pointed out that it is necessary to avoid any disturbance of the natural conditions of the biogeochemical micro-patterns by the measuring technique itself. Watt et al. (2006) highlighted the need of understanding the response in space and time of plants and plant communities to heterogeneity in soils. As shown earlier by authors' quantitative non-invasive imaging techniques to map dynamics of pH and oxygen in the rhizosphere of aquatic plants were presented for fully saturated conditions (Blossfeld & Gansert 2007, Jensen et al. 2005). In contrast to wetland plants, which are extensively studied, little has been documented for changes in partly saturated systems. Recently, Blossfeld et al. (2010) monitored the pH dynamics in the rhizosphere of different plant roots in unsaturated, trace-metal-contaminated

soils. Neutron radiography is a very sensitive tool to non-invasively map the water content distribution. In the last years the application in plant – soil systems is of increasing use (Esser et al. 2010, Menon et al. 2007, Tumlinson et al. 2008). The combination of both methodologies provides the unique possibility to map the interrelated pattern of oxygen, pH and water dynamics without disturbing the gradients.

## **1.2 State of the art**

### **1.2.1 Imaging in soil science**

A variety of non-destructive, non-invasive laboratory techniques are utilized for the measurement of the distribution of biogeochemical parameters in porous media and in root – soil systems. Common imaging methods used in soil science are optical imaging using UV or visible light, X-ray computed tomography, neutron radiography and magnetic resonance. Neutron radiography is of widespread use for industrial materials like fuel cells or batteries, biological materials like plants, geological materials like rocks and stones or archaeological objects (Strobl et al. 2009). Nevertheless, neutron imaging facilities are expensive with limited accessibility. Neutron radiography can only be performed in special laboratories while MRI and X-ray tomography are common imaging methods in hospitals and laboratories.

A variety of optical methods are used to image different parameters like flow and reactive transport in porous media, water content distribution, bacterial growth or distribution of roots. The most common use visible and fluorescent light (Werth et al. 2010). Measuring the water content in an artificial porous media can be done with light transmission (Niemet & Selker 2001) or light reflection imaging (Lazik et al. 2008). In 2001, Wenzel et al. introduced a novel rhizobox which in combination with photography yields root distribution, growth and morphology. Recently, Schmidt et al. (2011) used flat scanners in combination with image analysis to display areas of oxidation and reduction in paddy soils. Fluorescence imaging itself is based on light re-emission but additionally uses tracers within the porous media to measure for example water content (Bridge et al. 2007) or the oxygen distribution inside a plume during biodegradation of acetate (Huang et al. 2003) or of phenol (Rees et al. 2007). Yarwood et al. (2002) made use of the bioluminescence of *Pseudomonas fluorescens* to obtain noninvasively information about bacterial growth in a transparent artificial porous media. Moreover, fluorescence imaging can be used to quantitative measure colloidal transport in porous media (Bridge et al. 2006). However, the major disadvantage of light

reflection and light transmission measurements is the strictly limited application to transparent and therefore artificial media (hydroponic solutions, agar, glass beads).

Confocal laser scanning microscopy (CLSM) is another optical imaging method with the capability of three-dimensional imaging. If only the optically accessible upper layer of the porous media is of interest, sample preparation, measurements, and image analysis can be carried out with a cost- and time-saving set up (Muehl et al. 2012). Zevi et al. (2005) used CLSM to measure position, thickness, and contact angles of films and bulk liquid elements. Muehl et al. (2012) visualized the effect of wettability on area and connectivity of the water phase using CLSM and developed a segmentation strategy to enable water films and bulk water to be differentiated.

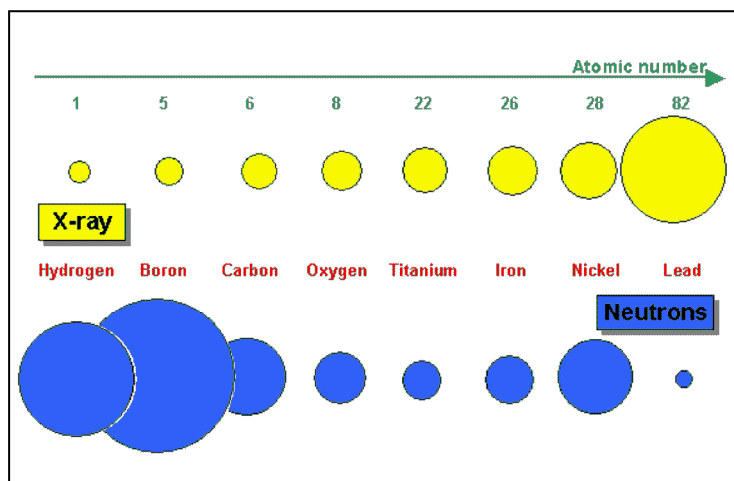


Figure 2: Comparison of the attenuation characteristics of selected materials for neutrons and X-ray (<http://www.psi.ch>)

X-ray computed tomography has been used for many years to obtain 3D images of biological, geological and industrial samples (Werth et al. 2010). X-rays are sensitive to density variations in the sample and the method is based on mapping the spatially-distributed different absorption of an X-ray beam as it passes through the sample (Kaestner et al. 2008).

Pierret et al. (2003) introduced the applicability of X-ray transmission through thin-slab systems to observe root water uptake and root growth. This method had the potential to images fine roots with sufficient spatial resolution at less cost compared to X-ray computer tomography (X-ray CT) (Pierret et al. 2003). At the size of soil aggregates with approx 3 – 4 mm diameter, Hallett et al. (2009) used X-ray CT to investigate the changes in soil pore structure induced by fluctuations in water content. Recently, Verboven et al. (2012) showed that X-ray micro-CT is able to visualize the microstructure of the gas space in plants. They used the images to calculate the O<sub>2</sub> fluxes and model O<sub>2</sub> profiles and compared them with microelectrode (Verboven et al. 2012). Nevertheless, X-ray tomography is favourable for investigating soil structure and pore morphology but less capable for measuring water distributions (Carminati et al. 2009). The

ability to discriminate between two materials (water and air) with closely similar attenuation values is difficult due to little contrast changes (Wildenschild et al. 2002).

Besides X-ray tomography, much research has focused on using magnetic resonance imaging (MRI) to investigate processes like the mechanisms of water infiltration (Amin et al. 1998), the spatial distribution of dissolved  $\text{Ni}^{2+}$  around the roots of *Berkheya coddii* (Moradi et al. 2010) or colloidal transport and deposition (Baumann & Werth 2005). Signal enhancing gadolinium tracer for example can be used to observe flow velocities in soils columns which are mostly too slow to be monitored directly (Haber-Pohlmeier et al. 2010). The basic of MRI is that atoms with uneven spin quantum numbers (e.g.  $^1\text{H}=1/2$ ) are magnetically susceptible. By applying an external magnetic field to the sample this causes the spins to align with the field resulting in a precession movement (Amin et al. 1998). The spins are forced to flip out of the magnetic field and relax back to their original state. The relaxation decays exponentially and is recorded as the MRI signal (Werth et al. 2010). However, limitations are the presence of other paramagnetic compounds in soil which distort the MRI images and cause signal loss (Amin et al. 1998). Therefore, this technique mainly is applied to carefully selected porous media such as pre-treated sand or soil, agar, and glass beads (Moradi et al. 2010).

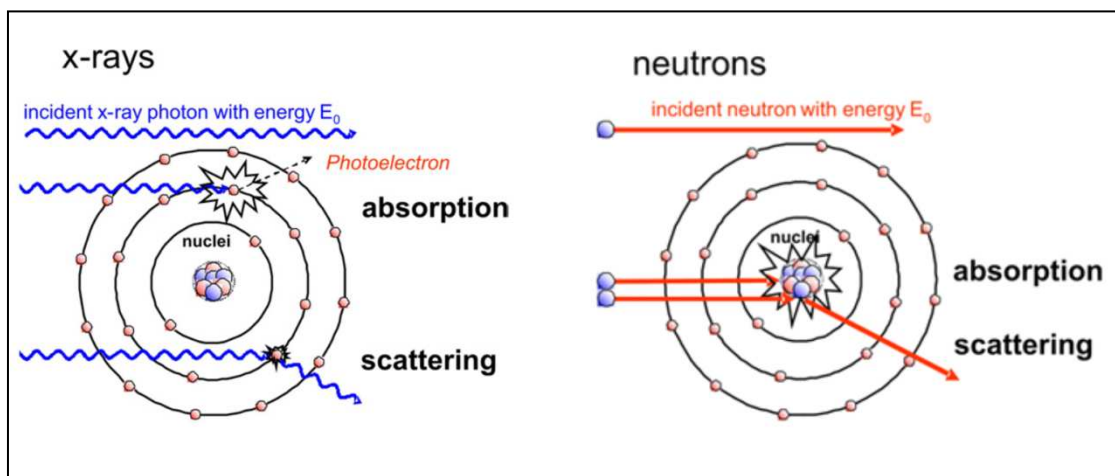


Figure 3: Comparison between X-ray and neutron interaction with matter (from Strobl et al., 2009)

The most recent and sensitive application to study water content distribution, root water uptake and root growth is neutron radiography (NR). Neutrons are a unique probe due to the fact that they have zero net charge. Consequently, unlike x-rays, neutrons do not interact with the electronic charge of the electrons but they interact with the atomic nucleus (Menon et al. 2007). Neutron radiography and X-ray tomography are complementary non-

invasive imaging techniques (see Fig. 2, 3). As neutrons directly probe the nuclei, they may give a strong contrast for elements that are close together in the periodic table (Strobl et al. 2009) or in between isotopes. X-rays on the other hand interact with the electronic charge and the contrast increases with the atomic number. The proton ( $^1\text{H}$  nucleus) shows a much larger interaction with neutrons than most other nuclide. In turn this high sensitivity to hydrous materials makes hydrogen-bearing materials such as water or many plastics highly visible (Oswald et al. 2008). For example, Deinert et al. (2004) used real-time neutron radiography to measure rapidly changing moisture profiles in porous media. Menon et al. (2007) made use of neutron radiography to study the in situ root development in contaminated soils. Because of its high sensitivity to water, neutron radiography can provide accurate images of water movement induced by plant uptake (Tumlinson et al. 2008).

Since the visualization of roots with a diameter  $<0.2$  mm is difficult (Moradi et al. 2009) a lot of work has been done with plants which have a thick root diameter. Two examples: (1) Esser and co-workers (2010) showed the applicability of neutron radiography and tomography to detect active parts for water uptake in lupin and maize roots. (2) Matsushima et al. (2009) combined neutron radiography with  $\text{D}_2\text{O}$  tracer to visualize water flow in small plants from root via stem to leaf or flower. Heavy water reduces the attenuation coefficient which improves the penetration depth of neutrons which in turn increases the signal (Matsushima et al. 2009).

### **1.2.2 Optical imaging using sensors**

The measurement of the distribution of physical and chemical parameters in heterogeneous systems is of wide general interest (Liebsch et al. 2000). Optical chemical sensors have experienced increasing success during the last decade (Stich et al. 2010). Optical sensors proved to be reliable analytical tools for monitoring various chemical and biological species (Borisov et al. 2011b). Such sensor materials consist of a dye incorporated in a polymeric matrix to produce a thin sensing foil. The choice of appropriate dye including polymeric matrix addressing the specific application is the major component. The oxygen permeability of the polymer mainly determines the sensitivity of the resulting sensor. Optical chemical sensors are free of electromagnetic interferences and are highly versatile in their formats (Borisov et al. 2011b). Analytes of wider interest include  $\text{O}_2$ ,  $\text{CO}_2$ , pH,  $\text{Cl}^-$ ,  $\text{Ca}^{2+}$ , and temperature.



In general, fluorescence is the emission of light from any substance, and occurs from electronically excited states (Lakowicz 2006). The processes that occur between the absorption and emission of light are illustrated by the Jablonski diagram. A typical simplified Jablonski diagram is shown in Figure 4. Upon excitation with light of suitable wavelength the fluorophore resides in one of the vibrational levels of an excited single state. Molecules then relax through internal conversion to the first excited state,  $S_1$  followed by a fall to the lowest vibrational level of  $S_1$ . From that point, the molecule can lose energy via different processes: (1) via radiationless internal conversion or (2) via the radiative depopulation of  $S_1$  by spontaneous emission of a photon. The spin of an excited electron can also be reversed by intersystem crossing leaving the molecule in the first excited triplet state,  $T_1$ . In most organic dyes intersystem crossing is inefficient but the probability increases if the vibrational levels of the single and triplet state overlap. However, the presence of heavy atoms can substantially increase the intersystem crossing. Again, molecule undergo intersystem crossing to  $S_0$  (Sauer et al. 2011).

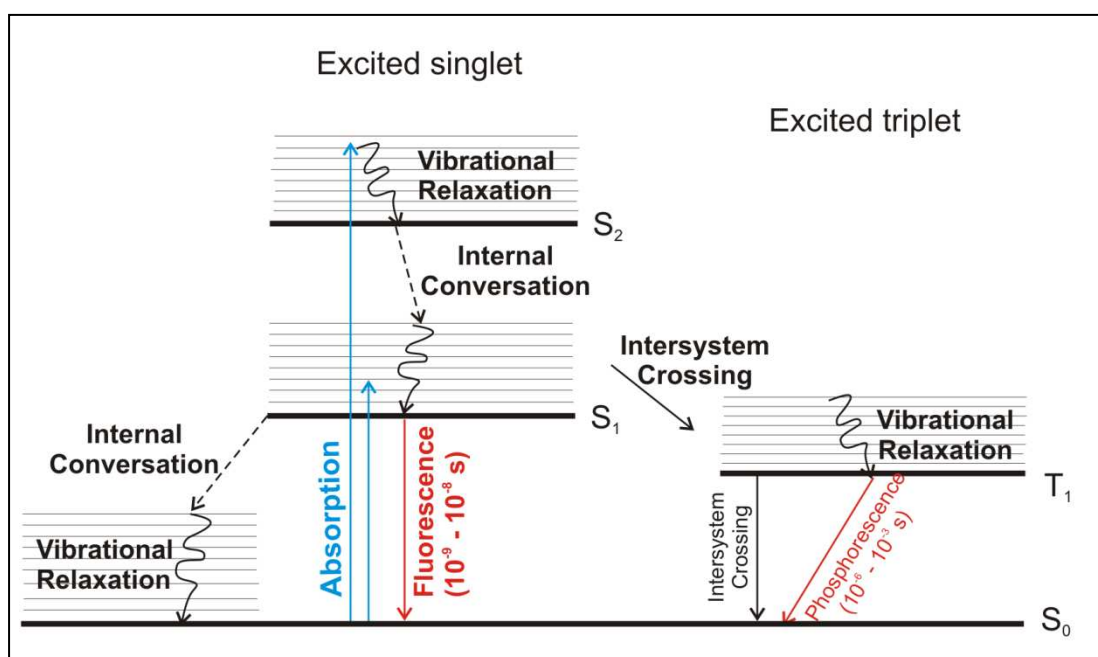


Figure 4: Typical Jablonski diagram with timescales of fluorescence and phosphorescence

Favorable sensor dye properties for fluorescence imaging did not depend on the biogeochemical parameter of interest. Important is that they provide large Stokes shifts, which means the absorption and emission signals can be separated spectrally (Borisov et al. 2006), and absorption/emission bands in the visible spectral range to ensure lower-cost equipment to

record (Fuller et al. 2003). The optical sensor response is mainly monitored by changes in fluorescence lifetime or intensity. The advantage of lifetime based measurements is that they are self-referenced but this includes a complex, expensive experimental setup and only a limited numbers of indicator dyes are suitable (Stich et al. 2010). Our novel approach, though being an intensity-based measurement only, has the advantages of mapping a larger area in shorter times and being based on lower cost equipment. This also allows a mobile, flexible and quick set-up for an experiment, with a number of possible replicates and without high costs.

There are several reports on the simultaneous determination of two or more parameters using optical sensors. Up to date, several kinds of dual sensors have been described, e.g., for CO<sub>2</sub>/O<sub>2</sub>, O<sub>2</sub>/T and pH/O<sub>2</sub> (Baleizao et al. 2008, Schröder et al. 2007a). Two examples: 1) Schröder et al. (2007a) developed a dual sensor for O<sub>2</sub>/CO<sub>2</sub> which has been optimized for use in aquatic systems. Since evolution consumption of oxygen and carbon dioxide are often strongly interrelated, the simultaneous detection of both parameters is of significant analytical interest. 2) Baleizão et al. (2008) introduced a sensor for trace oxygen and temperature. Due to the unmatched range and sensitivity application possibly range from biotechnological procedures to aerospace research to food packaging industry (Baleizao et al. 2008). The sensor architecture is expected to become increasingly sophisticated with increasing numbers of analytes that needs to be analyzed simultaneously. Recently, Borisov et al. (2011b) presented a novel sensing material suitable for simultaneous monitoring of four parameters including oxygen, carbon dioxide, pH, and temperature.

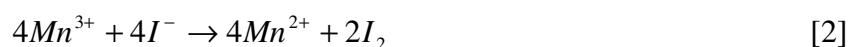
In comparison with the MRI, neutron, and X-ray imaging, there is one major drawback of optical imaging: Besides confocal laser scanning microscopy (CLSM) it is strictly limited to two-dimensional set ups. Nevertheless, optical chemical sensor films are ideally suitable for combination with other imaging techniques because the response of planar sensor foils can be easily read out with charge coupled device (CCD) cameras (Liebsch et al. 2000). Since this PhD thesis focus on oxygen and pH mapping via optical methods, the following section gives an overview starting from traditional methods to measure the parameters to sensor application.

## ***Oxygen***

Oxygen is one of the most important analytes on earth and is routinely monitored (Borisov et al. 2011a). Since most plants and microorganisms living in the top soils need

atmospheric oxygen ingress by diffusion gas movement through porous media is a fundamental aspect of many environmental, ecological, biological problems (Allaire et al. 2008). However, soils are characterized by structures (layers, aggregates, roots), which in turn can enhance the storage of water. In general, soil water greatly affects gas transport parameters by water blockage of gaseous flow paths (Hamamoto et al. 2009). The solubility of oxygen in water is quite low: at atmospheric pressure and a temperature of 25°C, air-saturated water contains about 8 mg L<sup>-1</sup> O<sub>2</sub> which decreases further with increasing temperature. Oxygen therefore is often rapidly depleted at locations where catabolic activity is high (Brune et al. 2000). For example at the root – soil interface, in biofilms and sediments, or in aggregates steep gradients of oxygen are common (Glud et al. 1998, Precht et al. 2004, Rudolph et al. 2012). Considerable heterogeneities can be observed at small scale within the soil matrix as shown when studying changes in redox potentials across small soil aggregates (Renault and Stengel 1994).

Traditional methods of determining oxygen concentrations in soil gas and water are labor intensive and not easily automated for semi-continuous monitoring (Patterson & Davis 2008). Oxygen sensing techniques are classified into the following categories: Winkler titration, amperometry (Clark electrode), and chemiluminescence (optical sensors) (Amao et al. 2000). Among these systems, the most popular method is the amperometric method, developed for use in physiology and based on coated platinum cathods (Klimant et al. 1995). This so called Clark electrode measures the rate of diffusion of oxygen to the cathode (Amao et al. 2000). The amperometry method can be miniaturized but still it is a localized measurement (Verboven et al. 2012). Winkler titration is the classical analytical method without any spatial resolution. The dissolved oxygen in the sample will be oxidized and fixed by adding Mn(II) and iodide solutions. Sulfuric acid is used to dissolve the resulting precipitation and an equivalent amount of iodine is formed. Thiosulfate is then used to titrate the solution until the color changes. The oxygen concentration can be calculated with knowledge of the amount of thiosulfate. The following equations describe the reaction:



### *Dynamic oxygen mapping using optical sensors*

Optical sensors for chemical species have undergone rapid development in the last decades (Klimant et al. 1995). The use of optical sensors is of increasing interest in different fields of research. The size of oxygen sensors varies and strongly depends on the experimental setup. Sediments and biofilms are characterized by steep gradients of various physical and chemical parameters over distances ranking from  $< 0.5$  mm to a few millimeters (Klimant et al. 1995). The dynamic behavior of the gradients can easily be captured with optical sensors due to their non-destructive character. In aquatic systems for example Glud et al. (1998) studies the  $O_2$  dynamics at the base of a biofilm. They showed that in mature biofilms heterogeneous  $O_2$  distributions were caused by clusters of high biomass which had low  $O_2$  saturation surrounded by oxygen rich voids and channels (Glud et al. 1998). At the interface of water and sediments in marine systems, Precht et al. (2004) looked at oxygen distribution in permeable sediments forced by advective pore water exchange. They obtained a spatial resolution of  $40 \mu\text{m}$  with  $37 \times 57$  mm field of view (Precht et al. 2004). Glud et al. (1996) measured vertical oxygen distributions in marine sediments and observed pronounced differences in penetration depth and also showed differences in thickness of the diffusive boundary layer due to small topographic structures. Their set up allowed the 2-dimensional distribution of oxygen to be resolved with a field of view of  $13 \times 17$  mm and a spatial resolution of  $26 \mu\text{m}$  (Glud et al. 1996). The redox dye cristal-violet will change from colorless to violet and was used by Van Noordwijk and Brouwer (1993) to visualize the oxygen transport in roots of wetland plants. As for rice they showed that the zone close to the root tip, root tips of emerging laterals and branch roots close to the stem were zones of high oxygenation (Vannoordwijk & Brouwer 1993). Jensen et al. (2005) investigated the spatial distribution of oxygen and radial oxygen loss in the roots of wetland plants. They showed that the rhizosphere of *Z. marina* is characterized by a constantly changing mosaic of oxic microniches with highest oxygen levels at the root tip.

### ***Soil pH***

Soil pH can substantially vary in space and time, as evidenced in both agricultural and forest ecosystems. Spatial variations are especially documented with changes over 0.5 - 3 units that are reported within a small plot scale down to millimeter scale (Hinsinger et al. 2009). For example, Göttlein and Matzner (1997) showed pH gradients of more than 0.5 pH units within 2 cm in forest soils. Soil pH can decrease in the vicinity of roots due to several

factors: root exudation of organic anions with a concomitant release of  $H^+$ ; cation-anion exchange balance by roots; redox-coupled processes; environmental and nutritional constraints (Martínez-Alcalá et al. 2010). Respiration and root exudation of organic carbon that will then be degraded by rhizosphere microorganisms lead to a built-up of  $CO_2$  in neutral and alkaline soils. This decreases the soil pH. Given that  $CO_2$  rapidly forms  $H_2CO_3$  which is a weak acid, increased  $pCO_2$  thus results in a decreased pH (Hinsinger et al. 2003). At acidic pH values,  $H_2CO_3$  remains undissociated therefore the contribution of root respiration and exudation, and consequent microbial respiration, to changes in rhizosphere can be neglected (Nye 1981). Heterogeneity of soil pH over space and time is also influenced by localized patches of organic matter or discrete distribution of  $CaCO_3$  grains (Hinsinger et al. 2009).

Measurements of pHs in soil solution or sedimentary deposits are typically made using  $H^+$  sensitive glass electrodes. The potentiometric technique is based on a galvanic cell which measures electromotive forces between a reference electrode and an electrode sensitive to the hydrogen ion activity. In general 0.01 M  $CaCl_2$  solution is used to extract soil solution of different soil materials which is then measured using glass electrodes. The construction of ion selective microelectrode gave the possibility to study  $H^+$  fluxes in intact maize roots as function of nitrogen source (Plassard et al. 1999). Zhang and Pang (1999) showed the general application of microelectrodes to microscale environments in the rhizosphere. This potentiometric technique is ideal for many applications but nevertheless is limited in resolving spatial patterns.

#### *Dynamic pH mapping using optical sensors*

Spectrophotometric pH measurements (optical sensors) are usually simpler and less expensive to construct than electrodes, show less electrical interferences, and can be used in remote detection schemes (Hulth et al. 2002). Introduced initially as simple pH indicator dye method limited to rather artificial conditions (Weisenseel et al. 1979), considerable effort has been directed toward the development of solute specific chemical sensors with optical detection (Lakowicz 2006). Owing to the general importance of pH measurements, a large number of pH sensors have been designed (Hulth et al. 2002, Schröder et al. 2007b, Stahl et al. 2006, Turel et al. 2008, Weidgans et al. 2004).

Among the studies, Weisenseel et al. (1979) introduced a method for mapping the pH changes mediated by barley roots which use pH indicator dyes in transparent agars. They used Bromocresol purple as dye which appears yellow under acidic conditions and appears purple

in its basic form and showed that the dye has no harmful effects on the growing plants (Weisenseel et al. 1979). Later, Römheld and Marschner (1983) mapped the spatial heterogeneities of pH changes in the rhizosphere of maize, wheat, chickpea and white clover. The plants were grown in natural soil and after a growing period between 4 to 10 days the soil and the roots were filtrated by agar (Marschner & Römheld 1983). In 2010, Martínez-Alcalá et al. used the same indicator dye to map the pH distribution by placing intact, in real soil grown roots into agarose gel. They visualized a strong acidification around cluster roots of white lupin ( $\text{pH} < 5$ ) while other parts showed slightly increased pH ( $> 7$ ) (Martínez-Alcalá et al. 2010). Jaillard et al. (1996) extended the method developed by Weisenseel et al. (1979). They introduced the color indicator videodensitometry which is based on the clear relationship between the optical density of Bromocresol and the pH in solution (Jaillard et al. 1996). Nevertheless, these examples illustrate the limitations: 1) An artificial system based on an agarose gel can hardly be as representative for real soils 2) Indicator reactions are non reversible so continuous monitoring is not possible 3) The spatial resolution was rather poor 4) The pH was mapped via a pH indicator yielding rather pH classification than pH resolution.

To overcome these limitations and to avoid any disturbance of the natural conditions, optical sensors offer a great possibility. The dyes incorporated into a polymeric matrix are reversible which makes it possible to study spatial and temporal changes over small distances. Blossfeld and Gansert (2007) used a pH sensitive foil to investigate the plant-mediated effects on microbial  $\text{CH}_4$  and  $\text{N}_2\text{O}$  production. They point wise triggered the pH changes by moving the readout device across the pH sensor. Recently, Blossfeld et al. (2010) visualized the heterogeneity of rhizosphere pH for alpine pennycress, maize and ryegrass. This study showed that rhizosphere pH has a local acidification dip 2 – 4 mm behind the root tip. Similar to oxygen, pH plays a key role in many important biogeochemical processes taking place in marine sediments. Stahl et al. (2006) observed pH hotspots with intensified microbial activity at the water – sediment interface but also pH minima along burrow walls of polychaetes (marine worms). Hulth et al. (2002) introduced a two-dimensional sensor system with a resolution of 55  $\mu\text{m}$  applied over an image of 34 x 26 mm. In this study small-scale heterogeneity and micro-niches associated with reactive organic material and locally enhanced mineralization of organic matter were clearly demonstrated (Hulth et al. 2002).

### 1.3 Objectives and thematic structure of the thesis

The general motivation of this thesis was to develop an in situ imaging method able to visualize the interrelated pattern of oxygen transport and water content distribution. We wanted to develop a methodology which is able to map the pattern with a high spatial and temporal resolution. The main aim is to visualize and quantify oxygen transition zones in soil resulting from the combined effect of soil structure, water flow, oxygen transport, and oxygen consuming reactions. We were interested in covering the knowledge gaps concerning the response of roots to oxygen deficits. We wanted to focus on the importance of bulk soil properties on rhizosphere pH dynamics.

In more detail, the aim of this study was to develop, adapt and apply a combined imaging approach to simultaneously capture the dynamics of oxygen, and pH, and the water content distribution. The first step was to develop a quantitative fluorescence imaging technique capable of studying the dynamics of oxygen and pH changes. The study focused on highly resolved visualization of oxygen and pH changes in the rhizosphere of different plant species. The second step was to develop a method to simultaneously quantify the distribution of oxygen concentration and water content. The major point was to monitor the formation of oxygen depletion zones forced by plant roots and limited oxygen recharge. The next step was to apply the combined approach to a structured soil system. Here we addressed the heterogeneity inherent to soils and their influence on oxygen transport and water content distribution. The last step was to setup a 2D reactive transport model to simulate acetate biodegradation. We aimed to prove that data obtained from imaging methods can give reasonable results. The study proceeded in four steps, each of which is described in one of the main chapters of this dissertation:

- (1) We developed a quantitative fluorescence imaging method to visualize the spatial and temporal pH changes around roots (chapter 2). Various bulk soil properties and plant species were analysed to identify their impact on the pH distribution.
- (2) We adapt the fluorescence imaging method (chapter 3) to study the spatiotemporal distribution of oxygen in variable saturated porous media. The method was then applied to monitor respiration activity in the plant-soil system. Roots act as an oxygen sink and the real time development of depletion zones of oxygen was mapped. For the first time, we successfully combined fluorescence imaging with highly sensitive

neutron radiography for studying simultaneously root growth, root respiration, root water uptake, and the soil water content.

- (3) The developed combined set-up (chapter 4) was subsequently applied to a structured soil system without plants. In order to mimic microbial oxygen demand and create a patchy structure of oxic and anoxic zones we use Pyrogallol which consumes oxygen by a chemical reaction.
- (4) In this study we combined microbiological, numerical modelling and imaging techniques to calibrate a nitrate-sensitive fluorescence tracer capable of monitoring the evolution of biodegradation under anaerobic, nitrate-reducing conditions. We set up a reactive transport model using Visual Modflow with the submodule RT3D2.5 to simulate anaerobic microbiological acetate degradation via consumption of nitrate (chapter 5). The reactive transport model was used to obtain the nitrate distribution as a function of microbiological growth and decay.



## References:

- Allaire SE, Lafond JA, Cabral AR, Lange SF (2008): Measurement of gas diffusion through soils: comparison of laboratory methods. *Journal of Environmental Monitoring* 10, 1326-1336
- Amao Y, Miyashita T, Okura I (2000): Optical oxygen sensing based on the luminescence change of metalloporphyrins immobilized in styrene-pentafluorostyrene copolymer film. *Analyst* 125, 871-875
- Amin MHG, Hall LD, Chorley RJ, Richards KS (1998): Infiltration into soils, with particular reference to its visualization and measurement by magnetic resonance imaging (MRI). *Prog Phys Geog* 22, 135-165
- Baleizao C, Nagl S, Schaferling M, Berberan-Santos MN, Wolfbeis OS (2008): Dual fluorescence sensor for trace oxygen and temperature with unmatched range and sensitivity. *Anal Chem* 80, 6449-6457
- Baumann T, Werth CJ (2005): Visualization of colloid transport through heterogeneous porous media using magnetic resonance imaging. *Colloid Surface A* 265, 2-10
- Bengough AG, McKenzie BM, Hallett PD, Valentine TA (2011): Root elongation, water stress, and mechanical impedance: a review of limiting stresses and beneficial root tip traits. *Journal of Experimental Botany* 62, 59-68
- Blossfeld S, Gansert D (2007): A novel non-invasive optical method for quantitative visualization of pH dynamics in the rhizosphere of plants. *Plant Cell Environ* 30, 176-186
- Blossfeld S, Perriguet J, Sterckeman T, Morel JL, Losch R (2010): Rhizosphere pH dynamics in trace-metal-contaminated soils, monitored with planar pH optodes. *Plant Soil* 330, 173-184
- Borisov SM, Vasylevska AS, Krause C, Wolfbeis OS (2006): Composite luminescent material for dual sensing of oxygen and temperature. *Advanced Functional Materials* 16, 1536-1542
- Borisov SM, Lehner P, Klimant I (2011a): Novel optical trace oxygen sensors based on platinum(II) and palladium(II) complexes with 5,10,15,20-meso-tetrakis-(2,3,4,5,6-pentafluorophenyl)-porphyrin covalently immobilized on silica-gel particles. *Anal Chim Acta* 690, 108-115
- Borisov SM, Seifner R, Klimant I (2011b): A novel planar optical sensor for simultaneous monitoring of oxygen, carbon dioxide, pH and temperature. *Anal Bioanal Chem* 400, 2463-2474
- Bridge JW, Banwart SA, Heathwaite AL (2006): Noninvasive quantitative measurement of colloid transport in mesoscale porous media using time lapse fluorescence imaging. *Environ Sci Technol* 40, 5930-6
- Bridge JW, Banwart SA, Heathwaite AL (2007): High-resolution measurement of pore saturation and colloid removal efficiency in quartz sand using fluorescence imaging. *Environ Sci Technol* 41, 8288-94
- Brune A, Frenzel P, Cypionka H (2000): Life at the oxic-anoxic interface: microbial activities and adaptations. *Fems Microbiol Rev* 24, 691-710
- Carminati A, Vetterlein D, Weller U, Vogel HJ, Oswald SE (2009): When Roots Lose Contact. *Vadose Zone J* 8, 805-809

- Deinert MR, Parlange JY, Steenhuis T, Throop J, Unlu K, Cady KB (2004): Measurement of fluid contents and wetting front profiles by real-time neutron radiography. *J Hydrol* 290, 192-201
- Esser HG, Carminati A, Vontobel P, Lehmann EH, Oswald SE (2010): Neutron radiography and tomography of water distribution in the root zone. *Soil Plant Nutrients* accepted
- Eynard A, Schumacher TE, Lindstrom MJ, Malo DD, Kohl RA (2006): Effects of aggregate structure and organic C on wettability of Ustolls. *Soil Till Res* 88, 205-216
- Fuller ZJ, Bare WD, Kneas KA, Xu WY, Demas JN, DeGraff BA (2003): Photostability of luminescent ruthenium(II) complexes in polymers and in solution. *Anal Chem* 75, 2670-2677
- Glud RN, Ramsing NB, Gundersen JK, Klimant I (1996): Planar optodes: A new tool for fine scale measurements of two-dimensional O<sub>2</sub> distribution in benthic communities. *Mar Ecol-Prog Ser* 140, 217-226
- Glud RN, Santegoeds CM, De Beer D, Kohls O, Ramsing NB (1998): Oxygen dynamics at the base of a biofilm studied with planar optodes. *Aquatic Microbial Ecology* 14, 223-233
- Goebel MO, Bachmann J, Woche SK, Fischer WR, Horton R (2004): Water potential and aggregate size effects on contact angle and surface energy. *Soil Sci Soc Am J* 68, 383-393
- Göttlein A, Matzner E (1997): Microscale heterogeneity of acidity related stress-parameters in the soil solution of a forested cambic podzol. *Plant Soil* 192, 95-105
- Gregory PJ, Hinsinger P (1999): New approaches to studying chemical and physical changes in the rhizosphere: an overview. *Plant Soil* 211, 1-9
- Haber-Pohlmeier S, Bechtold M, Stapf S, Pohlmeier A (2010): Water Flow Monitored by Tracer Transport in Natural Porous Media Using Magnetic Resonance Imaging. *Vadose Zone J* 9, 835-845
- Hallett PD, Feeney DS, Bengough AG, Rillig MC, Scrimgeour CM, Young IM (2009): Disentangling the impact of AM fungi versus roots on soil structure and water transport. *Plant Soil* 314, 183-196
- Hamamoto S, Moldrup P, Kawamoto K, Komatsu T (2009): Effect of Particle Size and Soil Compaction on Gas Transport Parameters in Variably Saturated, Sandy Soils. *Vadose Zone J* 8, 986-995
- Hanbury CD, Atwell BJ (2005): Growth dynamics of mechanically impeded lupin roots: Does altered morphology induce hypoxia? *Ann Bot-London* 96, 913-924
- Hanson PJ, Edwards NT, Garten CT, Andrews JA (2000): Separating root and soil microbial contributions to soil respiration: A review of methods and observations. *Biogeochemistry* 48, 115-146
- Hinsinger P, Plassard C, Tang CX, Jaillard B (2003): Origins of root-mediated pH changes in the rhizosphere and their responses to environmental constraints: A review. *Plant Soil* 248, 43-59
- Hinsinger P, Bengough AG, Vetterlein D, Young IM (2009): Rhizosphere: biophysics, biogeochemistry and ecological relevance. *Plant Soil* 321, 117-152
- Hodge A, Berta G, Doussan C, Merchan F, Crespi M (2009): Plant root growth, architecture and function. *Plant Soil* 321, 153-187

- Horn R, Smucker A (2005): Structure formation and its consequences for gas and water transport in unsaturated arable and forest soils. *Soil Till Res* 82, 5-14
- Horn R, Peth S (2009): Soil structure formation and management effects on gas emission. *Biologia* 64, 449-453
- Huang WE, Oswald SE, Lerner DN, Smith CC, Zheng C (2003): Dissolved oxygen imaging in a porous medium to investigate biodegradation in a plume with limited electron acceptor supply. *Environ Sci Technol* 37, 1905-11
- Hulth S, Aller RC, Engstrom P, Selander E (2002): A pH plate fluorosensor (optode) for early diagenetic studies of marine sediments. *Limnol Oceanogr* 47, 212-220
- Jaillard B, Ruiz L, Arvieu JC (1996): pH mapping in transparent gel using color indicator videodensitometry. *Plant Soil* 183, 85-95
- Jensen SI, Kuhl M, Glud RN, Jorgensen LB, Prieme A (2005): Oxic microzones and radial oxygen loss from roots of *Zostera marina*. *Mar Ecol-Prog Ser* 293, 49-58
- Kaestner A, Lehmann E, Stampanoni M (2008): Imaging and image processing in porous media research. *Advances in Water Resources* 31, 1174-1187
- Klimant I, Meyer V, Kuhl M (1995): Fiberoptic Oxygen Microsensors, a New Tool in Aquatic Biology. *Limnol Oceanogr* 40, 1159-1165
- Kristensen AH, Thorbjorn A, Jensen MP, Pedersen M, Moldrup P (2010): Gas-phase diffusivity and tortuosity of structured soils. *J Contam Hydrol* 115, 26-33
- Lakowicz JR (2006): Principles of Fluorescence Spectroscopy. Springer Science + Business Media New York
- Lazik D, Krauss G, Geistlinger H, Vogel H-J (2008): Multi-scale optical analyses of dynamic gas saturation during air sparging into glass beads. *Transport in Porous Media* in press
- Liebsch G, Klimant I, Frank B, Holst G, Wolfbeis OS (2000): Luminescence lifetime imaging of oxygen, pH, and carbon dioxide distribution using optical sensors. *Applied Spectroscopy* 54, 548-559
- Lipiec J, Walczak R, Witkowska-Walczak B, Nosalewicz A, Slowinska-Jurkiewicz A, Slawinski C (2007): The effect of aggregate size on water retention and pore structure of two silt loam soils of different genesis. *Soil Till Res* 97, 239-246
- Marschner H, Römheld V (1983): In vivo Measurement of Root-induced pH Changes at the Soil-Root Interface: Effect of Plant Species and Nitrogen Source. *Zeitschrift für Pflanzenphysiologie* 111, 241-251
- Martínez-Alcalá I, Walker DJ, Bernal MP (2010): Chemical and biological properties in the rhizosphere of *Lupinus albus* alter soil heavy metal fractionation. *Ecotox Environ Safe* 73, 595-602
- Matsushima U, Herppich WB, Kardjilov N, Graf W, Hilger A, Manke I (2009): Estimation of water flow velocity in small plants using cold neutron imaging with D(2)O tracer. *Nucl Instrum Meth A* 605, 146-149
- Menon M, Robinson B, Oswald SE, Kaestner A, Abbaspour KC, Lehmann E, Schulin R (2007): Visualization of root growth in heterogeneously contaminated soil using neutron radiography. *Eur J Soil Sci* 58, 802-810

- Moradi AB, Conesa HM, Robinson B, Lehmann E, Kuehne G, Kaestner A, Oswald S, Schulin R (2009): Neutron radiography as a tool for revealing root development in soil: capabilities and limitations. *Plant Soil* 318, 243-255
- Moradi AB, Oswald SE, Nordmeyer-Massner JA, Pruessmann KP, Robinson BH, Schulin R (2010): Analysis of nickel concentration profiles around the roots of the hyperaccumulator plant *Berkheya coddii* using MRI and numerical simulations. *Plant Soil* 328, 291-302
- Moradi AB, Carminati A, Lamparter A, Woche SK, Bachmann J, Vetterlein D, Vogel HJ, Oswald SE (2012): Is the Rhizosphere Temporarily Water Repellent? *Vadose Zone J*
- Muehl GJH, Ruehlmann J, Goebel MO, Bachmann J (2012): Application of confocal laser scanning microscopy (CLSM) to visualize the effect of porous media wettability on unsaturated pore water configuration. *J Soil Sediment* 12, 75-85
- Niemet MR, Selker JS (2001): A new method for quantification of liquid saturation in 2D translucent porous media systems using light transmission. *Advances in Water Resources* 24, 651-666
- Nye PH (1981): Changes of pH across the Rhizosphere Induced by Roots. *Plant Soil* 61, 7-26
- Oswald SE, Menon M, Carminati A, Vontobel P, Lehmann E, Schulin R (2008): Quantitative imaging of infiltration, root growth, and root water uptake via neutron radiography. *Vadose Zone J* 7, 1035-1047
- Patterson BM, Davis GB (2008): An in situ device to measure oxygen in the vadose zone and in ground water: Laboratory testing and field evaluation. *Ground Water Monit R* 28, 68-74
- Pierret A, Kirby M, Moran C (2003): Simultaneous X-ray imaging of plant root growth and water uptake in thin-slab systems. *Plant Soil* 255, 361-373
- Plassard C, Meslem M, Souche G, Jaillard B (1999): Localization and quantification of net fluxes of  $H^+$  along maize roots by combined use of pH-indicator dye videodensitometry and  $H^+$ -selective microelectrodes. *Plant Soil* 211, 29-39
- Precht E, Franke U, Polerecky L, Huettel M (2004): Oxygen dynamics in permeable sediments with wave-driven pore water exchange. *Limnol Oceanogr* 49, 693-705
- Rees HC, Oswald SE, Banwart SA, Pickup RW, Lerner DN (2007): Biodegradation processes in a laboratory-scale groundwater contaminant plume assessed by fluorescence imaging and microbial analysis. *Appl Environ Microbiol* 73, 3865-76
- Rennert T, Totsche KU, Heister K, Kersten M, Thieme J (2012): Advanced spectroscopic, microscopic, and tomographic characterization techniques to study biogeochemical interfaces in soil. *J Soil Sediment* 12, 3-23
- Rudolph N, Esser HG, Carminati A, Moradi AB, Hilger A, Kardjilov N, Nagl S, Oswald SE (2012): Dynamic oxygen mapping in the root zone by fluorescence dye imaging combined with neutron radiography. *J Soil Sediment* 12, 63-74
- Sauer M, Hofkens J, Enderlein J (2011): *Handbook of Fluorescence Spectroscopy and Imaging*. Wiley-VCH Weinheim
- Schmidt H, Eickhorst T, Tippkötter R (2011): Monitoring of root growth and redox conditions in paddy soil rhizotrons by redox electrodes and image analysis. *Plant Soil* 341, 221-232

- Schröder CR, Neurauter G, Klimant I (2007a): Luminescent dual sensor for time-resolved imaging of pCO<sub>2</sub> and pO<sub>2</sub> in aquatic systems. *Microchimia Acta* 158, 205-218
- Schröder CR, Polerecky L, Klimant I (2007b): Time-resolved pH/pO<sub>2</sub> mapping with luminescent hybrid sensors. *Anal Chem* 79, 60-70
- Stahl H, Glud A, Schröder CR, Klimant I, Tengberg A, Glud RN (2006): Time-resolved pH imaging in marine sediments with a luminescent planar optode. *Limnology and Oceanography-Methods* 4, 336-345
- Stich MIJ, Fischer LH, Wolfbeis OS (2010): Multiple fluorescent chemical sensing and imaging. *Chem Soc Rev* 39, 3102-3114
- Strobl M, Manke I, Kardjilov N, Hilger A, Dawson M, Banhart J (2009): Advances in neutron radiography and tomography. *J Phys D Appl Phys* 42, -
- Totsche KU, Rennert T, Gerzabek MH, Kogel-Knabner I, Smalla K, Spiteller M, Vogel HJ (2010): Biogeochemical interfaces in soil: The interdisciplinary challenge for soil science. *J Plant Nutr Soil Sc* 173, 88-99
- Totsche KU, Eusterhues K, Rennert T (2012): Spectro-microscopic characterization of biogeochemical interfaces in soil. *J Soil Sediment* 12, 1-2
- Tumlinson LG, Liu H, Silk WK, Hopmans JW (2008): Thermal Neutron Computed Tomography of Soil Water and Plant Roots. *Soil Sci Soc Am J* 72, 1234-1242
- Turel M, Cajlakovic M, Austin E, Dakin JP, Uray G, Lobnik A (2008): Direct UV-LED lifetime pH sensor based on a semi-permeable sol-gel membrane immobilized luminescent Eu<sup>3+</sup> chelate complex. *Sensor Actuat B-Chem* 131, 247-253
- Vannoordwijk M, Brouwer G (1993): Gas-Filled Root Porosity in Response to Temporary Low-Oxygen Supply in Different Growth-Stages. *Plant Soil* 152, 187-199
- Verboven P, Pedersen O, Herremans E, Ho QT, Nicolai BM, Colmer TD, Teakle N (2012): Root aeration via aerenchymatous phellem: three-dimensional micro-imaging and radial O<sub>2</sub> profiles in *Melilotus siculus*. *New Phytol* 193, 420-431
- Watt M, Silk WK, Passioura JB (2006): Rates of root and organism growth, soil conditions, and temporal and spatial development of the rhizosphere. *Ann Bot-London* 97, 839-855
- Weidgans BM, Krause C, Klimant I, Wolfbeis OS (2004): Fluorescent pH sensors with negligible sensitivity to ionic strength. *Analyst* 129, 645-650
- Weisenseel MH, Dorn A, Jaffe LF (1979): Natural H<sup>+</sup> Currents Traverse Growing Roots and Root Hairs of Barley (*Hordeum-Vulgare-L*). *Plant Physiol* 64, 512-518
- Wenzel WW, Wieshammer G, Fitz WJ, Puschenreiter M (2001): Novel rhizobox design to assess rhizosphere characteristics at high spatial resolution. *Plant Soil* 237, 37-45
- Werth CJ, Zhang CY, Brusseau ML, Oostrom M, Baumann T (2010): A review of non-invasive imaging methods and applications in contaminant hydrogeology research. *J Contam Hydrol* 113, 1-24
- Whalley WR, Riseley B, Leeds-Harrison PB, Bird NRA, Leech PK, Adderley WP (2005): Structural differences between bulk and rhizosphere soil. *Eur J Soil Sci* 56, 353-360
- Wildenschild D, Hopmans JW, Vaz CMP, Rivers ML, Rikard D, Christensen BSB (2002): Using X-ray computed tomography in hydrology: systems, resolutions, and limitations. *J Hydrol* 267, 285-297

- Yarwood RR, Rockhold ML, Niemet MR, Selker JS, Bottomley PJ (2002): Noninvasive quantitative measurement of bacterial growth in porous media under unsaturated-flow conditions. *Appl Environ Microbiol* 68, 3597-605
- Young IM, Crawford JW, Rappoldt C (2001): New methods and models for characterising structural heterogeneity of soil. *Soil Till Res* 61, 33-45
- Young IM, Crawford JW (2004): Interactions and self-organization in the soil-microbe complex. *Science* 304, 1634-1637
- Zevi Y, Dathe A, Mccarthy JF, Richards BK, Steenhuis TS (2005): Distribution of colloid particles onto interfaces in partially saturated sand. *Environ Sci Technol* 39, 7055-7064
- Zhang TC, Pang H (1999): Applications of microelectrode techniques to measure pH and oxidation-reduction potential in rhizosphere soil. *Environ Sci Technol* 33, 1293-1299

## Chapter 2

# Spatio-temporal mapping of local soil pH changes induced by roots of lupin and soft-rush<sup>1</sup>

*The rhizosphere is a dynamic system strongly influenced by root activity. Roots modify the pH of their surrounding soil causing the soil pH to vary as a function of distance from root surface, location along root axes, and root maturity. Non-invasive imaging techniques provide the possibility to capture pH patterns around the roots as they develop. We developed a novel fluorescence imaging set up and applied to the root system of two lupin (*Lupinus albus* L., *Lupinus angustifolius* L.) and one soft-rush (*Juncus effusus* L.) species. We grew plants in glass containers filled with soil and equipped with fluorescence sensor foils on the container side walls. We gained highly-resolved data on the spatial distribution of  $H^+$  around the roots by taking time-lapse images of the samples over the course of several days. We showed how the soil pH in the vicinity of roots developed over time to different values from that of the original bulk soil. The soil pH in the immediate vicinity of the root surface varied greatly along the root length, with the most acidic point being at 0.56 – 3.36 mm behind the root tip. Indications were also found for temporal soil pH changes due to root maturity. In conclusion, this study shows that this novel optical fluorescence imaging set up is a powerful tool for studying pH developments around roots in situ.*

**Keywords:** acidification, alkalization, exudates, fluorescence imaging, optical sensors, pH mapping, rhizosphere

---

<sup>1</sup> An article with equivalent content has been published as:

N. Rudolph, S. Voss, A.B. Moradi, S. Nagl, S.E. Oswald (2013): Spatio-temporal mapping of local soil pH changes induced by roots of lupin and soft-rush. *Plant Soil*, 369: 669-680

## 2.1 Introduction

Plant roots continuously modify the soil properties of their immediate vicinity, the so-called rhizosphere (Hauter and Mengel 1988; Nye 1981; Weisenseel et al. 1979). This causes the rhizosphere to have a dynamic character and to develop different physicochemical properties than those of the bulk soil. Key biological functions of plant roots such as water and nutrient uptake, respiration, and exudation alter the concentrations of nutrients, toxic elements and pollutants, pH, redox potential, and partial pressure of O<sub>2</sub> and CO<sub>2</sub> in their rhizosphere (Hinsinger et al. 2005). Root induced changes of soil pH can have various origins: root exudation of organic anions with an associated release of H<sup>+</sup>; root respiration and release of CO<sub>2</sub> which results in the formation of carbonic acid in the rhizosphere; cation-anion exchange balance in the root; and environmental and nutritional constraints resulting in enhanced root release of H<sup>+</sup> as a response to P or Fe deficiency or heavy metal toxicity (Hinsinger et al. 2003; Marschner and Römheld 1994; Nichol and Silk 2001). Change of pH in the rhizosphere, relative to bulk soil, is well documented in the studies of the soil-root interface (Hinsinger et al. 2003). However, most of those studies are point measurements and have poor spatial or temporal resolutions. Martínez-Alcalá et al. (2010) for example recently made use of bromocresol purple to map the pH distribution by placing agarose gel on the intact roots. They detected a decrease of pH around cluster roots of white lupin (pH <5) while other parts showed an increase to a pH of greater than 7. This study demonstrated the applicability of optical methods towards temporal pH changes in soil but still had a few limitations. 1) an artificial system based on an agarose gel does not fully resemble real soil; 2) the spatial resolution was rather limited and 3) the employed setup with a pH indicator observing its color change yielded only a coarse pH resolution. Local pH gradients were observed as a function of time in Hinsinger et al. (2009), and its distance from the root surface, location along the root axes, or root age (Nichol and Silk 2001).

Owing to the general importance of pH measurements in various disciplines and broad applications, a large number of optical pH sensors have been designed (Blossfeld and Gansert 2007; Hulth et al. 2002; Schröder et al. 2007; Stahl et al. 2006; Weidgans et al. 2004). All these sensors rely on the luminescence properties of an acid/base conjugate pair of the pH indicator and the permeation selectivity provided by a polymer matrix. Optical pH sensors have been successfully used for gaining insights into dynamics and distributions of protons at the interface between water and sediments in marine systems (Hulth et al. 2002; Stahl et al.



2006). Studies of the spatial heterogeneities of pH changes in the rhizosphere have been published based on the original work of Römheld and Marschner (1981).

Optical sensors enable sensing of biochemical parameters by making use of dyes whose signals can be differentiated by spectral and/ or temporal resolution (Stich et al. 2010). Most sensors are based on the measurement of one of the luminescence properties, e.g. intensity, lifetime, or spectral distributions (Fuller et al. 2003). The general detection principle for optical sensors is based on changes in the luminescence properties from immobilized solute specific indicators within thin-layered plastic films when exposed to the analyte. Our novel approach, though being an intensity-based measurement, has the advantages of mapping a larger area in shorter times while comprising of low cost equipment (Rudolph et al. 2012). It also allows a mobile, flexible and quick setup for experiments with relatively large number of replicates. The studies of Blossfeld and co-workers (2007; 2010) are based on the measurement of the fluorescence decay time of pH-sensitive indicator dyes using the dual lifetime referencing method (DLR). A sensor sensitivity to a pH range of 6 - 8.5 made it possible to map the dynamics in the rhizosphere of wetland plants (Blossfeld and Gansert 2007) and in the rhizosphere of trace-metal-contaminated soils (Blossfeld et al. 2010). The advantage of lifetime measurements is that they are self-referenced but this includes a complex, expensive experimental setup and only a limited numbers of indicator dyes are suitable (Stich et al. 2010).

The signal in most optical pH sensors is based on the change in the spectral properties of a pH-sensitive indicator, immobilized in a thin layer of a proton-permeable polymer (Weidgans et al. 2004). A large number of fluorescent pH indicators exist including various fluorescein derivatives (Schröder et al. 2007; Stahl et al. 2006; Weidgans et al. 2004), HPTS (8-hydroxypyrene-1,3,6,-trisulfonic acid) (Hulth et al. 2002) and europium(III) chelates (Turel et al. 2008). A visible response spectrum is preferred because it allows the use of inexpensive optics and light sources. The advantages of using fluorescein derivatives among other fluorescent indicators are their photophysical properties, which include high absorption coefficients and fluorescence quantum yields of typically higher than 0.9 (Weidgans et al. 2004). Stahl et al. (2006) incorporated a fluorescein derivative in a polyurethane hydrogel matrix resulting in a dynamic range of pH  $\approx$  7.3 to 9.3 to investigate the spatio-temporal variability in the pH distribution across the sediment-water interface. Weidgans et al. (2004) synthesize different fluorescein indicators with varying substituents. The resulting dynamic range of pH depend on the position of the halide substituent, e.g. 2',7'-Dichlorofluorescein

shows a dynamic range from pH 4.5 to 7.0 whereas 2'-Chlorofluorescein gave a pH range from 5.5 to 8.5 which is almost ideal for physiological sensing (Weidgans et al. 2004).

While most studies on localized pH changes in the direct vicinity of roots have been using techniques where plants are grown in rather artificial conditions such as hydroponic solution or agar gels (Hinsinger et al. 2009), in this study, we have developed a non-invasive fluorescence imaging approach to quantify pH distributions under more realistic conditions using sand and sandy soils. Moreover, we present data on temporal changes of pH in the rhizosphere *in situ* over the course of several days. The objective of the present study was to introduce and test a novel fluorescence dye imaging method for *in situ* visualization and quantification of pH in the rhizosphere of plants with high spatial and temporal resolutions. To illustrate the performance of the method, detailed information on the dynamics of root-induced pH changes around the roots of white lupin (*Lupinus albus L.*), narrow-leaved lupin (*Lupinus angustifolius L.*), and soft-rush (*Juncus effusus L.*) are presented.

## 2.2 Material and methods

### 2.2.1 Fluorescence sensor imaging

*Sensor preparation.* The sensor is in fact a thin foil composed of two layers, produced via different steps. The optical sensor materials consisted of a dye incorporated in a polymeric matrix. The matrix provides a solid support and serves as a solvent for the dye as well as a permeation selectivity. The sensor layer was prepared in two steps: First, 1 g hydrogel (HydroMed D4, AdvanSource Biomaterials, Wilmington, MA) was dissolved in 9 g 9:1 ethanol/ water mixture to give a 10% (w/w) stock solution of the matrix polymer. In the second step, 10 mg pH indicator 5-hexadecanoylamino fluorescein (Fisher Scientific, Schwerte, Germany) was dissolved in 1 g hydrogel solution. The sensor cocktail was then stirred for at least 12 h before being spread into a dust-free polyester support (Melinex 505, Puetz, Taunusstein, Germany) using a thin film coating device from Elcometer (Aalen, Germany). After solvent evaporation at ambient air for 24 h, the resulting sensor foils were in the desired range of 10  $\mu\text{m}$  thickness. Thickness was measured with a disc micrometer (Ultra Präzision Messzeuge GmbH, Glattbach, Germany). The foils were kept in the dark throughout storage.

The sensitivity of the sensor signal on ionic strength is a well-known issue in many sensing schemes, including optical pH sensing (Schröder et al. 2007; Weidgans et al. 2004). To minimize this interference, we chose a lipophilic fluorescein derivative (5-

hexadecanoylamino fluorescein) with long alkyl chains. This modification results in several advantages: (i) the number of charges is reduced to one which results in a negligible cross-sensitivity towards ionic strength, (ii) the indicator shows different colors for the basic and acidic forms, and (iii) the lipophilic character of the dye reduces leaching from the polymer matrix (Weidgans et al. 2004).

Based on Schröder et al. (2007), the fluorescence intensity in the images is related to the pH. The normalized fluorescence intensity is plotted against pH, and fitted by the Boltzmann (sigmoidal) function.

$$\frac{F}{F^0} = \frac{A1 - A2}{1 + \exp\left(\frac{pH - pK_a'}{p}\right)} + A2 \quad [1]$$

where  $F$  is the measured the fluorescence signal and  $F_0$  is an arbitrary reference value used for normalization of the calibration curve. Herein the reference was set at the highest pH of 8.2 used during calibration, therefore the fluorescence at this pH corresponds to 1 in the calibration curve. The calibration function is characterized by empirical parameters describing the minimum fluorescence value ( $A1$ ), the maximum fluorescence value ( $A2$ ), the point of inflection ( $pK_a'$ ), and the width ( $p$ ) of the sigmoidal curve. The point of inflection corresponds to the apparent  $pK_a$  value ( $pK_a'$ ) (Schröder et al. 2007). The 'apparent  $pK_a$ ' is the  $pK_a$  which is measured via fluorescence emission which is not necessarily the  $pK_a$  value of the molecule. Fluorescein for example has several equilibria which can be overlapping but only 2 of them show fluorescence signals (mono- and diionic form). Their fluorescence properties are not exactly the same which means that the measured  $pK_a$  is not the actual  $pK_a$  representing the transition from the neutral to the monoionic form and is therefore called 'apparent  $pK_a'$ '.

In fact, all optical sensors are cross-sensitive to temperature (Borisov et al. 2011). However, during the experiment presented the temperature changed between 19 °C – 25 °C where we did not found a significant effect on fluorescence intensity.

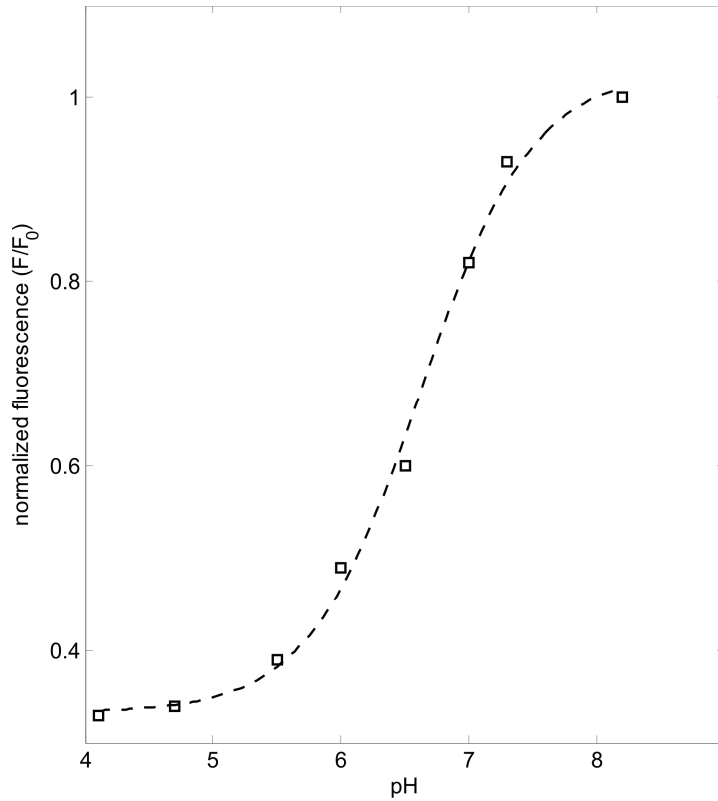


**Fig. 2.1:** Calibration curve of the polyurethane pH sensor layer on polyester foil used in this study

*Calibration.* Phosphate buffer solutions of pre-defined pHs were prepared from various mixtures of sodium salts of hydrogen phosphate and dihydrogen phosphate of analytical grade from Roth (Karlsruhe, Germany). Acidic and basic stock solutions were prepared by dissolving  $1.3799 \text{ g L}^{-1}$  of  $\text{NaH}_2\text{PO}_4 \cdot \text{H}_2\text{O}$  and  $1.799 \text{ g L}^{-1}$  of  $\text{Na}_2\text{HPO}_4 \cdot 2 \text{H}_2\text{O}$  respectively. Buffers with a range of pHs were prepared by mixing the two stock solutions. The pH values were checked using a digital pH meter (WTW, Weilheim, Germany) calibrated with standard buffers of pH 7.00 and 4.00. Calibration of the sensor was performed with determination of the fluorescence intensity at several pH values and at constant room temperature ( $21^\circ\text{C}$ ). Calibration was done on samples similar to one of the plant-growth experiment. The same container as in plant-growth experiments was filled with the same porous medium type and flushed with buffer solutions of different pH values. The normalized fluorescence signals are plotted against pH in Fig. 2.1. The calibration curve was fitted using equation [1]. The following fitting parameters were found:  $A1 = 0.333 \pm 0.016$ ,  $A2 = 1.029 \pm 0.027$ ,  $pKa' = 6.62 \pm 0.06$  and  $p = 0.436 \pm 0.051$ . The pH value maps were then calculated from the recorded grey value images according to equation [1] using Matlab (The MathWorks Inc., Natick, MA, USA).

### 2.2.2 Plant growth experiments

The containers used in this study had a height of 15 cm, a width of 15 cm and an internal thickness of 1.5 cm. All containers were equipped with pH foils attached to one of the inner sides. The sensor foils covered an area of 9.5 cm x 13 cm. The containers were made of glass to ensure transparency for optical imaging and were filled with a close to neutral quartz sand (pH = 6.6). To create a layered soil, we packed a layer of fine-grained (< 2  $\mu\text{m}$ ) quartz sand into the homogeneous quartz sand mixture (grain size distribution of 200 - 2000  $\mu\text{m}$ ). We built the layer to create two compartments. The upper compartment has a connection to the atmosphere and evaporation could potentially influence the results. Nevertheless, the soil surface was covered with a 1 cm layer of coarse gravel (3 mm diameter) to reduce evaporation. The lower compartment is separated from evaporation as long as the layer is water saturated, therefore we have stronger indication that changes are related to root activity. The containers were covered with dark cardboards to prevent light interference with root growth and functions. Seeds of white lupin (*Lupinus albus L.*) and narrow-leaved lupin (*Lupinus angustifolius L.*) were sown on the sand surface and watered to start germination (single seed per box). For each species, two containers were planted. The plants were grown for 11 days under controlled conditions in a climate chamber with a light/dark cycle of 14/10 h and a constant relative humidity of 60 %,. The day cycle starts at 6 am with a slope from 0 – 100 % illumination and 19 °C – 25 °C until 10 am. 100 % illumination corresponds to a light intensity of 300  $\mu\text{mol m}^2 \text{s}^{-1}$  and 25 °C starts from 10 am to 4 pm, followed by a slope until 0 % and 19 °C from 4 pm to 8 pm. In case of soft-rush (*Juncus effusus L.*), young seedlings were transplanted into the containers filled with acidic quartz sand (pH = 4.8) and a grain size distribution of 400 – 630  $\mu\text{m}$ . One plant per container (three in total) was grown for 3 weeks. The containers with soft-rush were kept submerged in water throughout the experiment. The temperature, humidity and light conditions were the same as described above.

For fluorescence imaging, the samples were illuminated by a UV lamp (type 215L, Peqlab, Erlangen, Germany) at 410 nm (Fig. 2.2). The fluorescence intensity was recorded using a CCD camera (type DX 4C-285, Kappa Optoelectronics, Gleichen, Germany) with an array of 1392 x 1040 pixels, 12-bit digitalization, and a field of view of 300 x 400 mm which resulted in pixel size of 0.28 mm. The CCD chip was cooled to a temperature of -15 °C to reduce thermal noise. The CCD camera was equipped with a 500 nm long-pass filter (Stemmer Imaging, Puchheim, Germany) to separate the excitation and emission light of the fluorescent dye. The distance between camera and sample was 0.5 m. The UV lamp was placed next to the CCD camera to ensure homogeneous illumination. We took fluorescence

images with acquisition times of 503 ms every 2 – 4 hours covering the diurnal changes of soil pH. The samples were weighed before each imaging. The transpiration rate was then calculated from the gravimetric weight differences. The soil surface was covered with a 1 cm thick gravel layer minimizing evaporation to a minimal value.

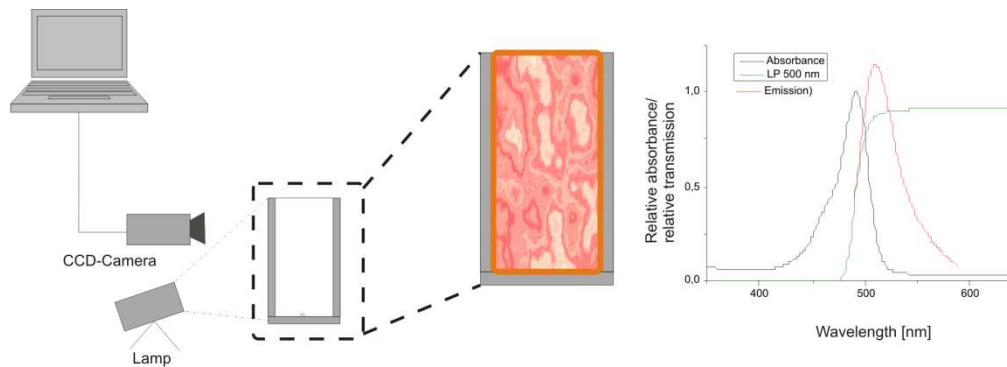


**Fig. 2.2:** Schematic view of the fluorescence imaging setup

## 2.3 Results

### 2.3.1 Sensor calibration

The fluorescein derivate in polyurethane we used gave a  $pK_a'$  value of 6.6 and a pH dynamic range of 5.0 to 8.0 (Fig. 2.1). This is well within the pH range of most of the soils and, therefore, proved suitable for root-soil studies. A pH range of 3 units means a large signal change per pH unit and, therefore, a high pH resolution (Schröder et al. 2007). Evaluation of sensor accuracy was done by comparison with a commercial pH meter (WTW, Weilheim, Germany). A 0.01 M  $\text{CaCl}_2$  solution was used to extract soil solution of different sand materials which were then measured using both pH sensors and a pH meter (Table 2.1). The two measurements deviated from each other by a pH unit of 0.0 - 0.3. This confirmed that the measurements via the optical sensor can give reasonable quantitative pH values as well as relative changes over space and time.

**Table 2.1:** Comparison of electrochemical pH measurements with sensor foil

Material	pH (CaCl <sub>2</sub> )	pH (optical sensor)
Quartz sand (400 – 630 $\mu\text{m}$ )	$4.78 \pm 0.06$	$4.92 \pm 0.03$
Quartz sand (200 – 2000 $\mu\text{m}$ )	$6.57 \pm 0.01$	$6.88 \pm 0.02$
Quartz clay (< 2 $\mu\text{m}$ )	$7.40 \pm 0.06$	$7.30 \pm 0.10$

### 2.3.2 Root growth

Roots are visible by their pH changes, if they grow not too far away from the sensor foil. Larger roots may appear with visible line in their centre due to their different brightness than soil, similar to the fact that roots can be visible in optical images if they are close to the surface of the soil. Though this way of locating roots is challenging for automated identification of root structure, independent measurements showed that it gives consistent results, e.g. confirmed by neutron radiography in case of oxygen sensing (Rudolph et al. 2012) or by invasive sampling after the measurements (data not shown). Within a series of time-lapsed images during periods of hours and days the elongation of roots can be visible and at these locations the newly formed part of the roots are known to be young.

Soft-rush forms a dense root network (fibrous root system), while lupin grows a taproot system. The lupin roots grew with an average rate of  $0.58 \text{ mm h}^{-1}$  ( $n=6$ ). Root elongation was calculated by counting the number of pixels along the root length in time-lapsed images. The results were in agreement with the findings of Hanbury and Atwell (2005) on root growth under various air pressure and soil oxygen concentrations. Hanbury and Atwell (2005) showed that root elongation was  $1.1 \text{ mm h}^{-1}$ , but decreased to  $0.5 \text{ mm h}^{-1}$  with soil O<sub>2</sub> concentrations below 10%. The fine-grained layer in the root-growth containers had a higher water content and smaller pore size than the rest of the soil and limited the gas exchange between the lower soil layer and the upper soil layer, and thus from the atmosphere. This caused the oxygen concentration in the lower part of the container to reduce due to ongoing root and soil respiration activity (data not shown). In the previous study (Rudolph et al. 2012), we used the same setup and showed that the fine-grained layer lead to formation of oxygen depletion zones around the roots.

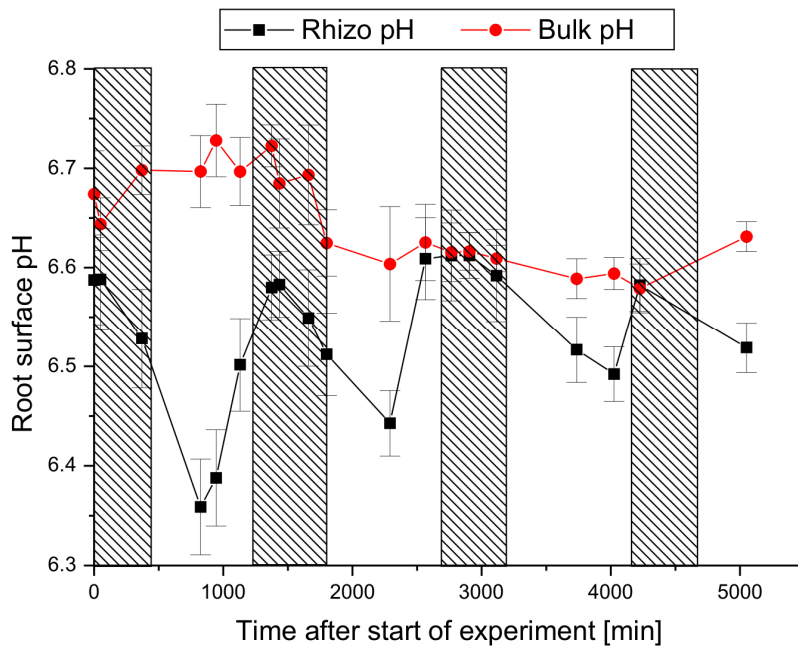


**Fig. 2.3:** Time series of pH distribution at a single spot (mean values out of an array of 3x3 pixel) in the rhizosphere of white lupin indicating a diurnal rhythm of pH and at a single pot in the bulk soil. On the x-axis time after start of the experiment with  $t_0=12$  midnight. The night cycles are indicated by the dashed rectangles.

### 2.3.3 Dynamics of soil pH around the roots

The time-lapse pH maps showed considerable changes of soil pH around the roots of all three investigated plant species. The soil pH development around the tap root of white lupin, grown in neutral soil, and of soft-rush, grown in acidic soil, over a course of a few days are shown in Fig. 2.3 and Fig. 2.4. The images in Figure 2.4 represent a region of interest (ROI), the complete images are shown in the supporting material (Figure S1). An average acidification of 1 pH unit (from pH 6.6 to 5.6) was measured in the soil adjacent to white lupin roots (Fig. S2). The root-induced acidification was stronger in the first 1.0 mm distance from the root surface. We identify this zone as the rhizosphere. From here, the soil pH increased slowly to that of the bulk soil, defined as soil far away from roots where soil pH did not change significantly. This acidification was observed to be stronger during daytime, with a minima during noon compared to the rest of the day (Fig. 2.3, Fig. S2). Time-series images of soil pH starting from day 12 to day 15 showed that the pH of the bulk soil in white lupin containers decreased from an average pH of  $6.66 \pm 0.13$  to an average pH of  $6.51 \pm 0.14$ . Three areas of 40 x 40 pixels, covering an area of  $376.32 \text{ mm}^2$  were averaged to calculate this change in bulk soil pH. This was done at fixed positions for starting conditions and at the end



of the experiment. This slight decrease could be due to root-induced acidification of the bulk soil or due to a decrease in soil water content, as has been observed by Kim et al. (1999). The soil water content in container planted with white lupin decreased by 8% and by 10%, respectively. In contrast to white lupin samples, an alkalization of the rhizosphere could be clearly identified for the roots of soft-rush (Fig. 2.4). We detected a pH increase of up to 1.44 units (pH 4.78 to 6.22) in the soil directly at the root surface of soft-rush plants. Similar to white lupin, the bulk soil remained unchanged for the first 2 days of investigation. However, it increased from a pH of 4.78 to a pH of 5.24 over the course of the next nine days.

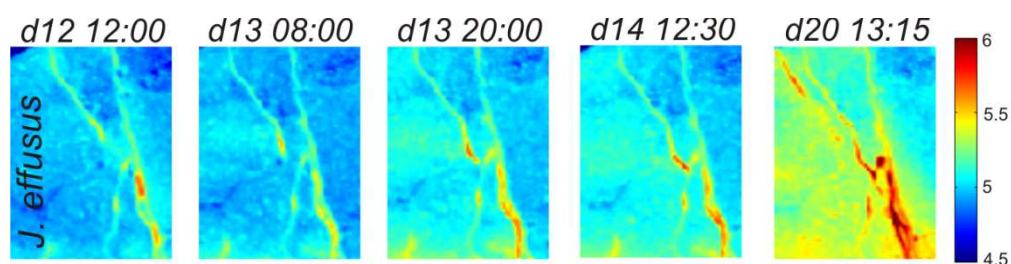


**Fig. 2.4:** Time series of pH distribution during root growth in containers planted with soft-rush (The part shown is a ROI from the full image and has a size of: 23 mm x 32 mm)

### 2.3.4 Variation in pH along the root length

The fluorescence images provided great details on the spatial and temporal variation of root-induced changes of pH both along the roots length and away from the root surface in the immediate surrounding soil, i.e. rhizosphere. Figure 2.5 illustrates the pH profiles in white lupin as a function of distance from the branching point along the root axis, in the direction of the root tip, over a course of 46 h, from day 12 early morning to day 13 late evening. We observed two acidification minima along the profile for all time-series. The root surface pH was found to be most acidic in the zone of maximum root elongation; distances of 0.56 to 3.36 mm behind the root tip (point 1-4, Fig. 2.5). The pH increased within the next mm from the root tip reached an intermediate level and then declined again (point 5, Fig. 2.5). Point 5 is where the lateral roots branched off from the main root. This pattern of a pH decline around the root branching points was observed consistently in all time-series.

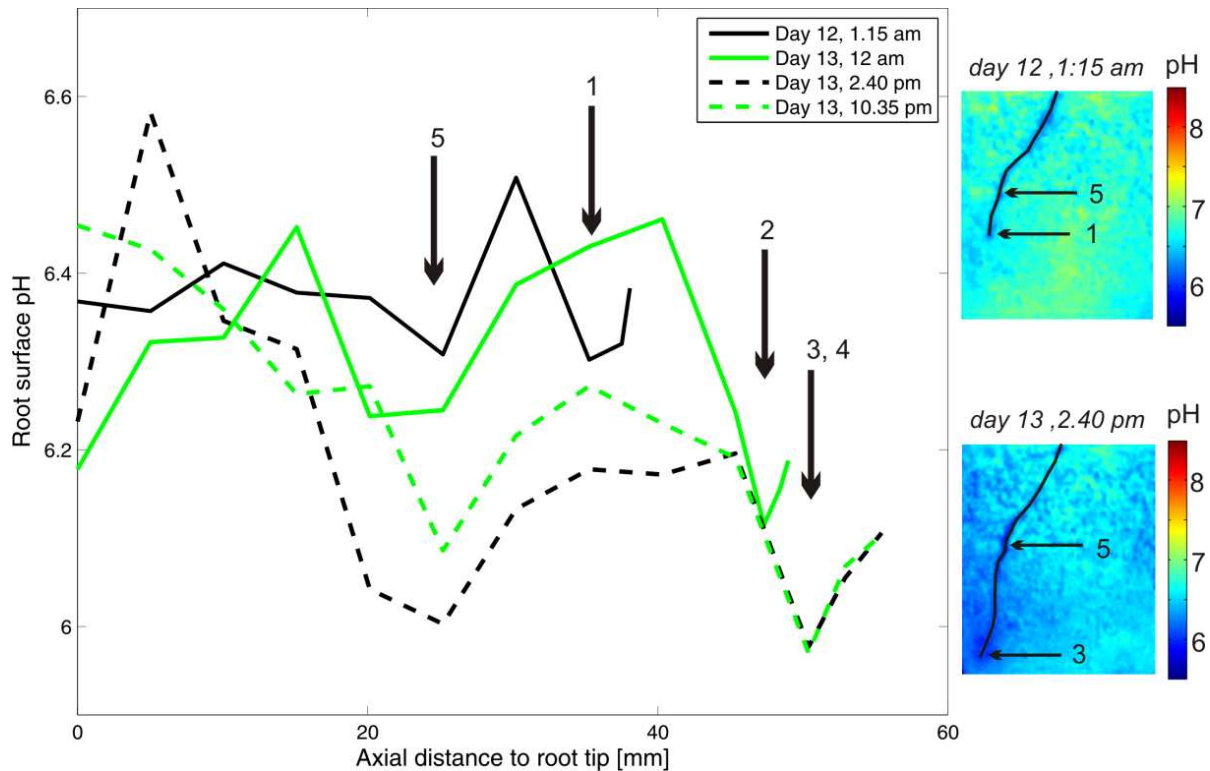


**Fig. 2.5:** Time series of pH profile along the growing tap root for white lupin over a course of 46 h. The profiles show pH as a function of axial distance from branching point in the direction of the growing root tip. The root tip is proceeding downward from distances of around 38 mm distance to 56 mm. The images on the right side show the corresponding pH dynamics where the black line indicates the position of the roots. The vertical arrows 1 – 4 indicate the area just behind the root tips whereas arrow 5 indicates a newly branching root (the arrow in the profile plot corresponds with those in the images).

### 2.3.5 Temporal variability in near-root pH

In addition to the spatial variability, we observed strong day and night cycles in soil pH changes at the root surface. This can be seen in the pH profiles of a single root of white lupin presented in Fig. 2.5. The main acidification was observed during day time at 2:40 pm (down to pH 5.92). We detected the main alkalization (up to pH 6.53) during night time. Monitoring the soil pH every two hours revealed that the acidification took place between 2:00 and 8:00 pm, whereas the main alkalization occurred between midnight and 6:00 am. The diurnal pH changes in the rhizosphere corresponded to the patterns of root water uptake. The average water loss in the samples during the measurements was  $0.42 \text{ g h}^{-1}$  (white lupin) and  $0.39 \text{ g h}^{-1}$  (narrow leafed lupin) during the photoperiod, and  $0.20 \text{ g h}^{-1}$  and  $0.22 \text{ g h}^{-1}$  during the night, respectively. We observed a maximum water loss between 2:00 pm and 3:00 pm and a minimum water loss between 8:00 pm and 10:00 pm. Therefore we can assume that the lateral transport of root exudates away from the root surface is slowest during

transpiration peaks, caused by the opposing water flow from soil towards the root and also a reduced effective diffusivity due to decreased water content around the roots.

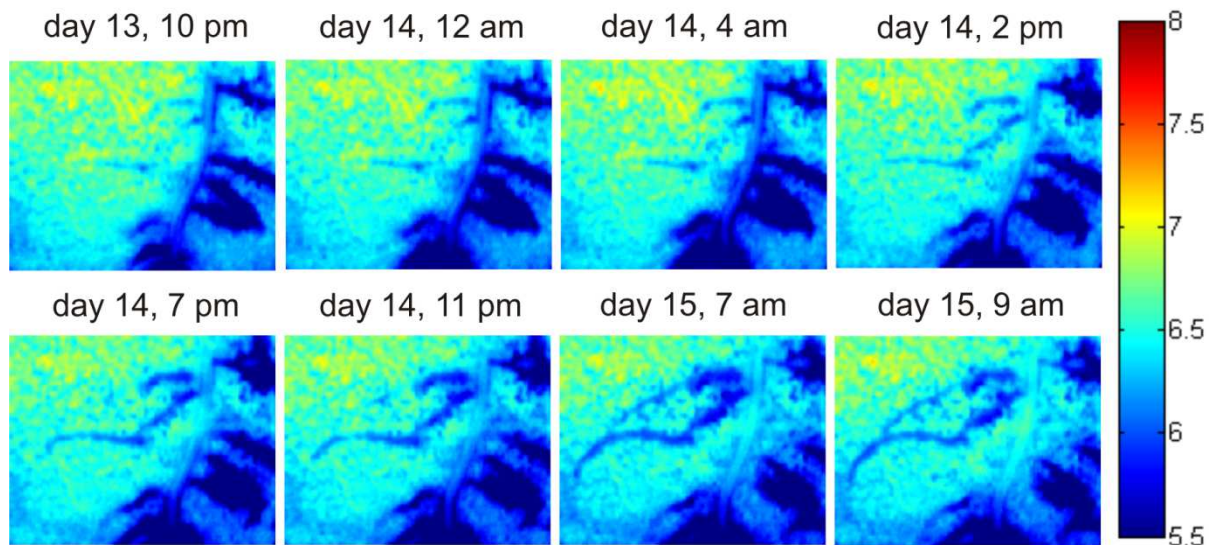


**Fig. 2.6:** Time series of pH distribution in the rhizosphere of narrow-leafed lupin (The part shown is a ROI from the full image and has a size of: 62 mm x 43 mm)

### 2.3.6 Rhizosphere pH dynamics in narrow-leafed lupin

The dynamics of the soil pH in the rhizosphere of a narrow-leafed lupin is shown in Fig. 2.6. The images represent a region of interest (ROI). For the complete images, see Figure S4 in the supporting material. Similar to white lupin, we observed root-induced acidification of the bulk soil by about 0.6 pH units (pH 6.6 to 6.0). The root surface pH of the tap root changed from acidic (pH=5.5) to neutral (up to pH 6.5) during the next 35 hours. The relatively large field of view in the pH images and the continuous monitoring of the  $H^+$  concentration enabled us to highlight the difference in pH evolution around the roots of different orders and ages. Acidification of the root surface and the soil in the immediate surroundings of the seminal roots appeared to be stronger than those of the lateral roots (Fig. 2.7, right). The pH at the centre of the root seems to be increased a little, but this is an artifact resulting from the bright colored tap root in the images. We did not try to correct for that in the pH images, but accounted for it in the interpretation.

Interestingly, the soil acidification around the lateral roots showed a more diffused pattern, compared to that of the seminal roots, and extended farther into the bulk soil (Fig. 2.7, right). Additionally, there was a clear difference in the pH distributions around the old roots

from those of the young growing roots (Fig. 2.7, left). With increasing plant age, the rhizosphere acidification reversed and its pH increased slowly to that of the bulk soil.

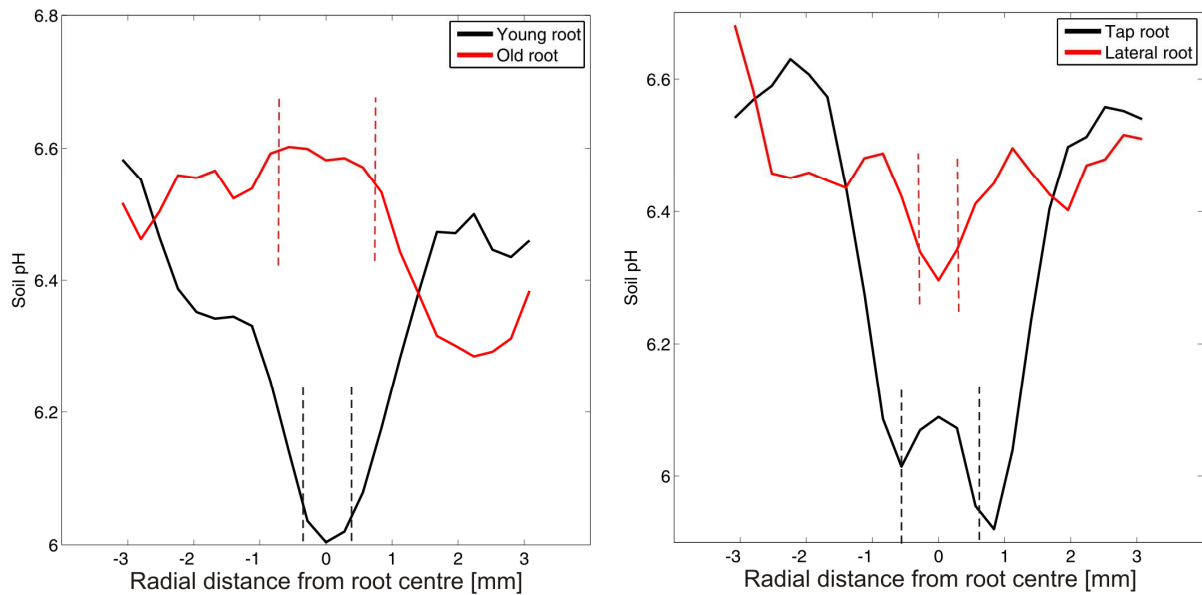


**Fig. 2.7:** Soil pH profiles around the roots of different ages as a function of distance from the root centre (young root vs. old left, tap root vs. lateral root right). The dashed vertical lines indicate the diameter of the corresponding roots

## 2.4 Discussion

This study reports on the capabilities of a novel pH sensitive sensor foil for monitoring *in situ* pH development in soil and rhizosphere of plants with high spatial and temporal resolutions. The fluorescein derivative 5-hexadecanoylamino fluorescein used in this study showed a  $pK_a'$  of 6.6 with a dynamic range of  $pK_a'$  of  $6.6 \pm 1.5$  pH units. This perfectly covers the neutral pH region which is relevant to the root environment of most of the plants.

The pH dynamics around the roots of white lupin and soft-rush presented in this study showed opposite behavior which we attribute to different initial bulk soil properties, e.g. bulk soil pH. While white lupin roots grown in neutral sands tend to acidify their rhizosphere, soft-rush roots grown in acidic sand alkalized them. The soil alkalization observed around the roots of soft-rush is in contrast to results presented by Blossfeld and Gansert (2007) for an alkaline soil. They illustrated that under similar conditions growing roots induced acidification of a wetland soil by about one pH unit (pH 8.5 to 7.5). The capability of plants to acidify and/ or to alkalize their rhizosphere, depending on their environment, was also reported by Chaignon et al. (2002). In their study, tomato and oilseed rape decreased the

rhizosphere pH when growing in calcareous soil, but increased the pH in acidic soil. Additionally, soil buffering capacity may play a major role. The observed pH changes (1.44 pH units for soft-rush, 1 pH unit for white lupin) can be related to the soil type we used here and its low buffering capacity. Hauter and Mengel (1988) showed that the pH decrease at the root surface of clover was heavily dependent on the buffering capacity of the soil. In the sandy soil, the pH at the root surface was about one unit lower than in the bulk soil whereas in the calcareous soil, the pH did not differ from bulk soil (Hauter and Mengel 1988).

Besides soil conditions, the source of nitrogen has been reported to influence the pH changes in the rhizosphere (Hinsinger et al. 2003). To maintain electrical neutrality across the root - soil interface, the pH changes in the rhizosphere are a consequence of either nitrate ( $\text{HCO}_3^-$  exported, pH rises) or ammonium ( $\text{H}^+$  exported, pH falls) uptake. If nitrogen is taken up as uncharged molecule ( $\text{N}_2$  fixation)  $\text{H}^+$  is exported and rhizosphere pH usually decreases (Gregory and Hinsinger 1999). Generally lupins are legumes and the observed pH decrease could be related to  $\text{N}_2$  fixation. The method presented in this study is able to map heterogeneities in the rhizosphere with a high spatial and temporal resolution. Therefore it could be used to study pH dynamics under various forms of nitrogen fertigation. However, during the study presented no nutrients were added to the plants. Therefore it is not possible to judge if the observed patterns are related to heterogeneous nitrogen uptake or nutrient deficiency. Nevertheless the method presented is able to capture pH changes and future experiments have to prove the influence of fertigation on rhizosphere pH changes.

The extent and the magnitude of the pH change were greatest in the vicinity of the root tip compared to the rest of the root length for both plant species (Fig. 2.3). This is consistent with literature, in which localized acidification was reported to occur behind the root tip (for instance, Marschner and Römheld (1994)). The root surface pH was found to be most acidic 0.56 to 3.36 mm behind the root tip (point 1-4, Fig. 2.5). This is due to fast root elongation rate compared to slow proton diffusivity. Observed elongation rates for lupine roots have been reported to range between  $0.58 \text{ mm h}^{-1}$  (in this study) to  $1.3 \text{ mm h}^{-1}$  (Hanbury and Atwell 2005). compared to proton diffusivity in most soils which range between  $0.0723 \text{ mm}^2 \text{ h}^{-1}$  in dry sandy soil (Kim et al. 1999) to  $0.44 \text{ mm}^2 \text{ h}^{-1}$  for a sandy soil with 60% of field capacity (Nichol and Silk 2001). The acidification behind the root tip is followed by an increase in pH and a second dip in acidification. We hypothesize that the second dip in acidification (point 5, Fig. 2.5) is induced by the newly-emerging lateral roots which is in agreement with the results obtained by Jaillard et al. (1996). The second decrease in root surface pH is consistently followed by an increase in pH, which represents the older, top part of the root. It has been

reported earlier that the various parts of the roots behave differently and that both alkalization and acidification could occur along a single root, suggesting that they can be attributed to various root functions (Chaignon et al. 2002).

Our results provided great details on pH changes as a function of distance from the root centre (Fig. 2.7). We could clearly show that pH values varied strongly with root age and root order. Large changes in physiological properties occur along the roots as a result of tissue aging and differentiation (Hodge et al. 2009). Our observations are in agreement with literature. For example, Plassard et al. (1999) mapped pH changes of young maize seedlings using indicator dye videodensitometry and microelectrodes. They reported similar patterns of pH distribution around the roots as function of distance from root surface. After exposure to agar gel the roots decreased the pH from 6.7 to 6.3. The acidification decreased further with increasing exposure time. 120 minutes after exposure the pH decreased to almost 5.9. Assuming that the diffusion coefficient of protons is  $D = 0.0723 \text{ mm}^2 \text{ h}^{-1}$  in a sandy soil and  $D = 33,84 \text{ mm}^2 \text{ h}^{-1}$  in aqueous solution (Kim et al. 1999) the extension of rhizosphere acidification is expected to be stronger in agar compared to our soil experiment.

With the presented quantitative optical pH imaging approach, it is possible to gain highly-resolved spatial and temporal  $\text{H}^+$  distribution around the roots of different plant species growing in a sandy medium. In comparison to expensive luminescence lifetime resolving cameras and fiber optics that provide only for point measurements, this method can be established with low cost optical equipment (camera, filters and lamps). We showed that the methodology presented here proved to be effective in sandy matrix. This should also apply to non sandy soil material, but with some limitations on dynamic range and accuracy. Sensor accuracy could suffer from dye leaching out of the polymeric hydrogel matrix. This effect can be prevented by a lipophilic character of the chosen dye which is embedded in the hydrophobic blocks of the employed hydrogel (Weidgans et al. 2004), by covalent bonding of the pH probe to the sensor matrix or by encapsulation of the pH indicator in nanoparticulate form. Herein, the pH sensitive dye is immobilized by adsorption. Limitations on dynamic range may arise from soils with high buffering capacity. This needs to be explored further. Nonetheless, a spatial resolution of 250  $\mu\text{m}$  can easily be achieved while maintaining a field of view of 10 x 13 cm. The time resolution can be as good as a few seconds. The selected fluorescent sensor matrix working in the neutral pH range was suitable for conducting soil - plant studies. Applying this method to the root system of soft-rush we showed that over the course of several days the pH in the vicinity of roots increased by as much as 1.4 pH units, contrasting earlier studies with other methods reporting a pH decrease. Additionally, our observation

implies that the young roots tend to acidify their rhizosphere whereas the older root parts of the root system tend to alkalize the rhizosphere, at least in our experimental system. Overall, the presented fluorescence imaging technique can be combined with other non-invasive techniques such as neutron imaging and other optical sensors (Rudolph et al. 2012) for quasi-simultaneous imaging of water, oxygen, and pH distribution at the root – soil interface. Furthermore, the ongoing development of optical sensors offers the opportunity to map other parameters in the future, e.g. temperature or CO<sub>2</sub> (Stich et al. 2010).

**Acknowledgements** We acknowledge funding from the German DFG priority program 1315 “Biogeochemical interfaces in soil”, under contract OS 351/1-2. We thank the Helmholtz Centre for Environmental Research – UFZ in Leipzig, Germany, for providing optical imaging equipment. Also, we thank Jonathan Bridge, formerly University of Sheffield, now at The University of Liverpool, for his comments on the manuscript.

## References

- Blossfeld S and Gansert D 2007 A novel non-invasive optical method for quantitative visualization of pH dynamics in the rhizosphere of plants. *Plant Cell Environ* 30, 176-186.
- Blossfeld S, Perriguet J, Sterckeman T, Morel J L and Losch R 2010 Rhizosphere pH dynamics in trace-metal-contaminated soils, monitored with planar pH optodes. *Plant Soil* 330, 173-184.
- Borisov S M, Seifner R and Klimant I 2011 A novel planar optical sensor for simultaneous monitoring of oxygen, carbon dioxide, pH and temperature. *Anal Bioanal Chem* 400, 2463-2474.
- Chaignon V, Bedin F and Hinsinger P 2002 Copper bioavailability and rhizosphere pH changes as affected by nitrogen supply for tomato and oilseed rape cropped on an acidic and a calcareous soil. *Plant Soil* 243, 219-228.
- Fuller Z J, Bare W D, Kneas K A, Xu W Y, Demas J N and DeGraff B A 2003 Photostability of luminescent ruthenium(II) complexes in polymers and in solution. *Anal Chem* 75, 2670-2677.
- Gregory P J and Hinsinger P 1999 New approaches to studying chemical and physical changes in the rhizosphere: an overview. *Plant Soil* 211, 1-9.
- Hanbury C D and Atwell B J 2005 Growth dynamics of mechanically impeded lupin roots: Does altered morphology induce hypoxia? *Ann Bot-London* 96, 913-924.
- Hauter R and Mengel K 1988 Measurement of pH at the Root Surface of Red-Clover (*Trifolium, pratense*) Grown in Soils Differing in Proton Buffer Capacity. *Biol Fert Soils* 5, 295-298.
- Hinsinger P, Bengough A G, Vetterlein D and Young I M 2009 Rhizosphere: biophysics, biogeochemistry and ecological relevance. *Plant Soil* 321, 117-152.
- Hinsinger P, Gobran G R, Gregory P J and Wenzel W W 2005 Rhizosphere geometry and heterogeneity arising from root-mediated physical and chemical processes. *New Phytol* 168, 293-303.
- Hinsinger P, Plassard C, Tang C X and Jaillard B 2003 Origins of root-mediated pH changes in the rhizosphere and their responses to environmental constraints: A review. *Plant Soil* 248, 43-59.
- Hodge A, Berta G, Doussan C, Merchan F and Crespi M 2009 Plant root growth, architecture and function. *Plant Soil* 321, 153-187.
- Hulth S, Aller R C, Engstrom P and Selander E 2002 A pH plate fluorosensor (optode) for early diagenetic studies of marine sediments. *Limnol Oceanogr* 47, 212-220.
- Jaillard B, Ruiz L and Arvieu J C 1996 pH mapping in transparent gel using color indicator videodensitometry. *Plant Soil* 183, 85-95.
- Kim T K, Silk W K and Cheer A Y 1999 A mathematical model for pH patterns in the rhizospheres of growth zones. *Plant Cell Environ* 22, 1527-1538.
- Marschner H and Roemheld V 1994 Strategies of Plants for Acquisition of Iron. *Plant and Soil* 165, 261-274.
- Marschner H and Römheld V 1994 Strategies of Plants for Acquisition of Iron. *Plant Soil* 165, 261-274.
- Martínez-Alcalá I, Walker D J and Bernal M P 2010 Chemical and biological properties in the rhizosphere of *Lupinus albus* alter soil heavy metal fractionation. *Ecotox Environ Safe* 73, 595-602.
- Nichol S A and Silk W K 2001 Empirical evidence of a convection-diffusion model for pH patterns in the rhizospheres of root tips. *Plant Cell Environ* 24, 967-974.
- Nye P H 1981 Changes of pH across the Rhizosphere Induced by Roots. *Plant Soil* 61, 7-26.



- Plassard C, Meslem M, Souche G and Jaillard B 1999 Localization and quantification of net fluxes of  $H^+$  along maize roots by combined use of pH-indicator dye videodensitometry and  $H^+$ -selective microelectrodes. *Plant Soil* 211, 29-39.
- Römheld V and Marschner H 1981 Iron-Deficiency Stress-Induced Morphological and Physiological-Changes in Root-Tips of Sunflower. *Physiol Plantarum* 53, 354-360.
- Rudolph N, Esser H G, Carminati A, Moradi A B, Hilger A, Kardjilov N, Nagl S and Oswald S E 2012 Dynamic oxygen mapping in the root zone by fluorescence dye imaging combined with neutron radiography. *J Soil Sediment* 12, 63-74.
- Schröder C R, Polerecky L and Klimant I 2007 Time-resolved pH/pO<sub>2</sub> mapping with luminescent hybrid sensors. *Anal Chem* 79, 60-70.
- Stahl H, Glud A, Schröder C R, Klimant I, Tengberg A and Glud R N 2006 Time-resolved pH imaging in marine sediments with a luminescent planar optode. *Limnology and Oceanography-Methods* 4, 336-345.
- Stich M I J, Fischer L H and Wolfbeis O S 2010 Multiple fluorescent chemical sensing and imaging. *Chem Soc Rev* 39, 3102-3114.
- Turel M, Cajlakovic M, Austin E, Dakin J P, Uray G and Lobnik A 2008 Direct UV-LED lifetime pH sensor based on a semi-permeable sol-gel membrane immobilized luminescent Eu<sup>3+</sup> chelate complex. *Sensor Actuat B-Chem* 131, 247-253.
- Weidgans B M, Krause C, Klimant I and Wolfbeis O S 2004 Fluorescent pH sensors with negligible sensitivity to ionic strength. *Analyst* 129, 645-650.
- Weisenseel M H, Dorn A and Jaffe L F 1979 Natural H<sup>+</sup> Currents Traverse Growing Roots and Root Hairs of Barley (*Hordeum-Vulgare-L*). *Plant Physiol* 64, 512-518.

## Chapter 3

# Dynamic oxygen mapping in the root zone by fluorescence dye imaging combined with neutron radiography<sup>2</sup>

*The rooted zone of a soil, more precisely the rhizosphere, is a very dynamic system. Some of the key processes are water uptake and root respiration. We have developed a novel method for measuring the real-time distribution of water and oxygen concentration in the rhizosphere as a biogeochemical interface in soil. This enables understanding where and when roots are active in respect to root respiration and water uptake and how the soil responds to it.*

*We used glass containers (15×15× 1 cm), which were filled with a quartz sand mixture. Sensor foils for fluorescence dye imaging of O<sub>2</sub> were installed on the inner side of the containers. A lupine plant was grown in each container for 2 weeks under controlled conditions. Then we took time series of fluorescence images for timelapsed visualization of oxygen depletion caused by root respiration. Changing water content was mapped in parallel by non-invasive neutron radiography, which yields water content distributions in high spatial resolution. Also it can detect the root system of the lupine plants. By this combined imaging of the samples, a range of water contents and different oxygen concentration levels, both induced by root activities, could be assessed.*

*We monitored the dynamics of these vital parameters induced by roots during a period of several hours. We observed that for high water saturation, the oxygen concentration decreased in parts of the container. The accompanying neutron radiographies gave us the information that these locations are spatially correlated to roots. Therefore, it can be concluded that the observed oxygen deficits close to the roots result from root respiration and show up while re-aeration from atmosphere by gas phase transport is restricted by the high water saturation.*

*Our coupled imaging setup was able to monitor the spatial distribution and temporal dynamics of oxygen and water content in a night and day cycle. This reflects complex plant activities such as photosynthesis, transpiration, and metabolic activities impacting the root–soil interface. Our experimental setup provides the possibility to non-invasively visualize these parameters with high resolution. The particular oxygen imaging method as well as the combination with simultaneously mapping the water content by neutron radiography is a novelty.*

**Keywords:** *fluorescence imaging, neutron radiography, oxygen mapping, rhizosphere, root respiration, water distribution*

---

<sup>2</sup> An article with equivalent content has been published as:

N. Rudolph, H.G. Esser, A. Carminati, A.B. Moradi, A. Hilger, N. Kardjilov, S. Nagl, S.E. Oswald (2012): Dynamic oxygen mapping in the root zone by fluorescence dye imaging combined with neutron radiography. *Soils and Sediments*, 12:63-74

### 3.1 Introduction

In soils and sediments there is a strong coupling between biogeochemical processes and local, often heterogeneous, distribution of water, electron acceptors, acids, nutrients and pollutants. Both sides are closely related and affect each other from the microscopic to the field scale. Oxygen is one of the most important factors in biological systems. Oxygen distribution is highly variable in soils, with concentrations ranging from aerobic conditions down to strictly anaerobic conditions (Hinsinger, Bengough et al. 2009). Knowledge of oxygen concentration gradients is of prior importance in understanding the function and regulation of microbial communities (Klimant, Meyer et al. 1995) and plants.

Oxygen undergoes a net transfer from atmosphere to soil by advective and diffusive processes. For not too wet soil conditions an oxygen flux mainly occurs via gas phase transport. In contrast, in the saturated capillary fringe and groundwater the transport occurs in the aqueous phase, and thus is substantially slower than for drier conditions. Soil is a complex three-phase system with varying degrees of spatial and temporal heterogeneity of physical and chemical properties (Luster, Gottlein et al. 2009). Typical soil structures such as aggregates, clay, layers, macropores and wettability differences occurring in natural soils imply that heterogeneity and patchiness is a general feature (Brune, Frenzel et al. 2000). Plant roots are an additional source of heterogeneity in soils. Roots are locations of high biogeochemical activity and strongly influence the surrounding soil. This includes exudation of organic acids, respiration activity and uptake of water (Hinsinger, Bengough et al. 2009). Root mediated processes often show a strong dependency from each other. For example, root water uptake may decrease when roots are exposed to anaerobic conditions (Tournaire-Roux, Sutka et al. 2003).

Blossfeld & Gansert (2007) pointed out the need to avoid any disturbance of the natural conditions of the biogeochemical micro-patterns. Due to the destructive character of conventional methods it is difficult to assess the spatial distribution and temporal dynamics of the variables of interest. By applying non-destructive measurements it is possible for particular parameters to overcome these limitations. Common example is X-ray CT, mostly suited to map the distribution of material density. Other imaging methods have recently been introduced for soil investigations, and two of them are fluorescence imaging and neutron radiography.

In the last two decades optical sensors for chemical species found increasing use for plant (Blossfeld and Gansert 2007), marine (Glud, Ramsing et al. 1996; Precht, Franke et al.

2004) and microbiological research (Glud, Santegoeds et al. 1998). The receptor part of optical chemical sensors is based on chemical species that show a change in their optical properties (e.g. absorption or emission intensity at particular wavelengths) depending on local environment conditions. The sensitivity and selectivity towards a specific analyte is also influenced by the polymeric matrix in which the sensor molecule is embedded. For oxygen, this mechanism is the basis for a point measurement of oxygen by laser excitation and lifetime measurement at optode spots, which is increasingly applied in practice (Blossfeld & Gansert 2007). Optical sensors have been developed for variety of important environmental analytes such as pH, CO<sub>2</sub>, temperature, O<sub>2</sub> and various ionic species (Fuller, Bare et al. 2003).

Fluorescence-based chemical sensors have many advantages compared to other methods. They show a fast response, they are highly sensitive, reversible and are capable of spatially resolved data acquisition (“imaging”) (Baleizao, Nagl et al. 2008). Their drawbacks include limited photostability of the indicator dyes (Schroeder, Polerecky et al. 2007). Inaccuracies may also arise from camera drift (Borisov, Vasylevska et al. 2006) or non-homogeneous lighting (Liebsch, Klimant et al. 2000). Applications of fluorescence sensors are numerous. In aquatic systems, for example Glud et al. (1998) studied the O<sub>2</sub> dynamics at the base of a biofilm. At the water sediment interface in marine systems Precht et al. (2004) looked at oxygen distribution in permeable sediments forced by advective pore water exchange, and Schroeder et al. (2007) developed a dual sensor for imaging dynamics of pO<sub>2</sub> and pH. The latter was also mapped for smaller parts of a root system (Blossfeld & Gansert 2007, Schreiber et al. 2010). Moreover, optical sensors have been used to study the development of oxic zones for aquatic plants (Jensen, Kuhl et al. 2005) and very recently Blossfeld et al. (2011). In contrast to wetland plants, which are extensively studied, little has been documented for changes in partly saturated systems.

Neutron imaging has a long history with more than seven decades of research. Neutrons are very efficiently attenuated by materials rich in hydrogen. This makes neutron radiography an optimal tool to investigate water and root distribution in soils. The considerable progress in recent times is mainly due to the developments in digital image recording (Strobl, Manke et al. 2009). CCD camera based detector systems have several advantages, like low acquisition times, good reproducibility and a high dynamic range (Lehmann, Pleinert et al. 1999). Applications range from non-destructive testing of industrial components to scientific investigations in biology, geology, material science and physics (Kardjilov, Hilger et al. 2005). Recently, several investigators showed the applicability of neutron radiography in soil science with special focus on water and plant related research.

Deinert et al. (2004) used neutron radiography to study variations of moisture content across a wetting front moving through porous media. Matsushima et al. (2009) showed the applicability of neutron radiography to monitor the velocity of water transport inside rose plants. Oswald et al. (2008) reported that neutron radiography (NR) is a promising imaging technique for studying water relations between soils and plants. Because of its high sensitivity to water, tomography by neutrons can provide accurate images of water movement induced by root water uptake (Tumlinson, Liu et al. 2008; Moradi, Carminati et al. 2011).

In this study we have developed a non-invasive fluorescence imaging technique to quantify oxygen content distribution and its temporal changes *in situ* with high spatial resolution. Moreover, we imaged simultaneously the water content distributions by neutron radiography to visualize and quantify the inter-related pattern of oxygen consumption and water distribution in complex aerobic root-soil systems. This combination allowed also for a direct interpretation, if gas phase re-supply of oxygen was restricted or not. Our aim was to capture the in-situ oxygen and water distributions with a spatial and temporal resolution appropriate for the rhizosphere. We successfully mapped the effects of root water uptake and respiration under restricted aeration in sand packings. This oxygen mapping by fluorescence dye imaging is designed to visualize also oxygen distributions at other biogeochemical interfaces and is suited to work in natural soils also.

## **3.2 Materials and methods**

### **3.2.1 Fluorescence oxygen imaging**

Oxygen sensitive dyes are based on the ability of oxygen to act as fluorescence quencher, thereby decreasing the fluorescence quantum yield (Carraway, Demas et al. 1991). The optical properties depend on the choice of fluorescent dyes and its carrier polymer. For example, metalloporphyrins dyes with fluoro-substituents typically show increased photostability and slow photodecomposition due to their electron-withdrawing properties that prevent oxidation in the excited state (Schroeder, Polerecky et al. 2007). Suitable fluorescence dyes possess high chemical stability (Carraway, Demas et al. 1991), high quantum yields (Amao and Okura 2000), fast response and recovery times (Mills and Lepre 1997). Among the most viable sensors that have been used in literature are Ruthenium(II) diimine (Liebsch, Klimant et al. 1999), fullerene (Nagl, Baleizao et al. 2007), platinum(II) as well as palladium(II) porphyrin complexes (Amao and Okura 2000; Borisov, Vasylevska et al. 2006). The optical sensor response is monitored by changes in fluorescence intensity, lifetime, or

spectral distributions (Fuller, Bare et al. 2003). These dye complexes have favorable properties. They provide large Stokes shifts, which means the absorption and emission signals can be separated spectrally (Borisov, Vasylevska et al. 2006), and absorption/emission bands in the visible spectral range to ensure lower-cost equipment to record (Fuller, Bare et al. 2003). Upon excitation, the emissive triplet state is quenched (deactivated) by the triplet molecular oxygen ground state (Bacon and Demas 1987). Therefore sensor layers in oxygen-free water show the strongest fluorescence intensity  $I_0$ . The quenching effect is a function of temperature and oxygen concentration (Baleizao, Nagl et al. 2008). At constant temperature, the Stern-Volmer plots show a nonlinear behavior for most oxygen indicator dyes (Carraway, Demas et al. 1991). This behavior can be described by a modified Stern-Volmer equation based on a two-site quenching model (Carraway, Demas et al. 1991; Demas, Degraff et al. 1995):

$$\frac{I_0}{I} = \left[ \frac{f}{1 + K_{SV}[O_2]} + (1 - f) \right]^{-1} \quad (1)$$

Eq. (1) is a simplified form of the general two-site model assuming a constant non-quenchable second fraction, where  $I$  is the fluorescence intensity,  $K_{SV}$  is the Stern-Volmer constant,  $[O_2]$  is the oxygen concentration, and  $f$  and  $(1-f)$  reflects the quenchable and non-quenchable fraction of the fluorescent dye, respectively (Carraway, Demas et al. 1991).

*Preparation of the oxygen sensing matrix.* Most of such optical sensor materials consist of a dye incorporated in a polymeric matrix that serves as a solvent for the dye, as a solid support and as a selectively permeable membrane. The sensor foil for oxygen was prepared in two steps. 20 mg of Platinum (II) 5,10,15,20-tetrakis(2,3,4,5,6-pentafluorophenyl)porphyrin (Pt-PFPP) purchased from Porphyrin Systems ([www.porphyrin-systems.de](http://www.porphyrin-systems.de)) and 1,98 g of polystyrene obtained from Sigma-Aldrich ([www.sigmaaldrich.de](http://www.sigmaaldrich.de)) were dissolved in 18 g of toluene purchased from Sigma Aldrich. The “cocktail” was stirred over night and knife-coated onto a 100  $\mu\text{m}$  polyester support (Melinex 505, [www.puetz-folien.com](http://www.puetz-folien.com)). After solvent evaporation at ambient air the resulting sensor foils are in the range of 10  $\mu\text{m}$  thickness. Thickness is an important parameter especially for oxygen sensing because lateral diffusion of the analyte in the sensitive film may cause limitations (Liebsch, Klimant et al. 2000). Schroeder et al. (2007) showed that this complex has an increased photostability due to the electron-withdrawing pentafluorophenyl substituents of the porphyrin ligands. Moreover, in marine experiments under water saturated conditions no significant change in the calibration function was monitored within a period of 18 months (Precht, Franke et al. 2004); which

implies that the dye neither was bleached nor diffused out of the foil in substantial amounts. For the latter reason possible phytotoxicity of the dye was not a prime issue, because the foil itself was stable, and this was not assessed here.

*Calibration of the oxygen sensing matrix.* The calibration of the sensor was performed at room temperature (21°C) with determination of the fluorescence intensity of the dye at several oxygen concentrations. We conducted the calibration under conditions similar to the experiments. The container was filled with the same porous medium and flushed with water of different oxygen concentrations. The fluorescence intensity of the oxygen indicator versus oxygen concentration is displayed in Fig. 3.1. The “two-site model” described in Equation [1] was used to fit the data. The model fits the experimental data very well. Moreover,  $f$  and  $K_{SV}$  are determined from the calibration points by rearranging Eq. (1) (Glud, Ramsing et al. 1996). The calculated values for  $f$  and  $K_{SV}$  were 0.37 and 0.19 mg/l<sup>-1</sup>, respectively.

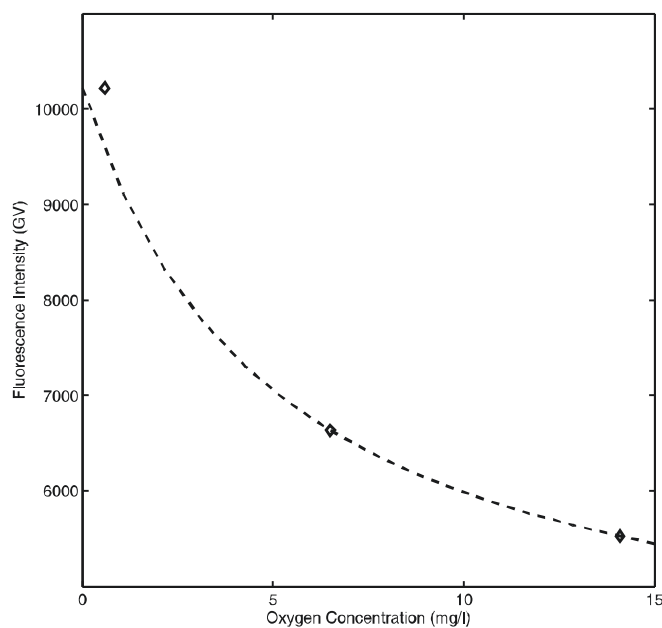


**Fig. 3.1** Fluorescence intensity as a function of dissolved O<sub>2</sub> concentration in water. The dotted line represents the fit with the modified Stern-Volmer-equation [Eq. 1].

### 3.2.2 Neutron radiography

Neutrons and protons are constituents of the atomic nuclei. Whereas protons have a positive net charge, neutrons are electrically neutral. Because of their zero net charge neutrons do not interact with electrons, but with atomic nuclei, and have highly different attenuation



coefficients even for elements of similar atomic number or isotopes of one element. This is in contrast to X-rays, which interact with electronic charge and therefore the interaction increases with atomic number. Whereas X-ray imaging strongly responds to heavy elements, neutron radiography (NR) in comparison is sensitive mainly to hydrogen and hydrogen bearing materials. This dominant sensitivity to  $^1\text{H}$  in soil systems results in a good visualization of water and roots, which mainly consist of water (Moradi, Conesa et al. 2009). The high spatial and temporal resolution of neutron radiography permits the visualization of changes at the soil–root interface without disturbance of the gradients. Information about mass and thickness of neutron-attenuation components can be derived by comparing the transmitted and unperturbed neutron beam. Neutron radiography techniques are based on the exponential law (similar to the Lambert–Beer law) of attenuation of radiation passing through matter, in our case composed of grains, water and air (Oswald, Menon et al. 2008):

$$I(x, z) = I_0(x, z) * e^{-\Sigma L(x, z)} \quad (2)$$

where  $(x, z)$  is the plane perpendicular to the neutron beam direction  $y$ ,  $I(x, z)$  is the detected neutron flux after an incident neutron flux  $I_0(x, z)$  passes through material of thickness  $L(x, z)$  with a neutron attenuation coefficient of  $\Sigma$ .

*Image analysis.* Neutron radiographs show the neutron penetration through the sample in the direction of the beam. Neutrons can be absorbed or scattered, but they can also pass the sample undisturbed. With increasing water content, in soil there is a much higher probability for neutron scattering than for neutron absorption (Hassanein 2006). Scattered neutrons may reach the detector and then increase the image intensity recorded, which leads to an underestimation of the neutron attenuation or ultimately water mass density (Moradi, Conesa et al. 2009). In our study, the transmission images were first processed by the Quantitative Neutron Imaging (QNI) algorithm (Hassanein 2006). It corrects the images for scattering, beam fluctuations, detector non-uniformities, and camera noise using the open beam image without the sample and the image without beam (dark current). After correction, the intensity of the transmitted neutron beam through the sample is described by the exponential law taking into account the individual attenuation coefficients of the sample:

$$-\log \left[ \frac{I(x, z)}{I_0(x, z)} \right] = \Sigma_{cont} L_{cont}(x, z) + \Sigma_{H_2O} L_{H_2O}(x, z) + \Sigma_{soil} L_{soil}(x, z) \quad (3)$$

The subscript *cont* refers to the container, *H<sub>2</sub>O* to water, and *soil* to the dry soil (quartz). The attenuation coefficient of water is calculated by QNI software. Then, rearranging Eq. (3), we calculate  $L_{H_2O}(x,z)$ . The water content  $\theta$  is defined as:

$$\theta(x, z) = \frac{L_{H_2O}(x, z)}{L_{tot}(x, z)} \quad (4)$$

where  $L_{tot}(x,z)$  is the sample thickness. Eq. (4) yields the water content averaged along the beam direction (Carminati and Fluhler 2009). For this study, we expect that the two-dimensional average of the water content is sufficient to compare the data with the fluorescence images.

### 3.2.3 Experimental set-up

The first part of the experiment involved imaging water content and oxygen concentrations in a homogeneously-packed glass bead medium, without plant roots, as a relatively simple system. By that, we could test the two imaging methods and highlight the influence of the water content distribution on oxygen diffusion at room temperature (21°C). The containers had internal dimensions of 0.1 m x 0.2 m x 0.05 m and were filled with glass beads (from Carl Roth, Germany; [www.carl-roth.de](http://www.carl-roth.de)). The glass beads had a grain size distribution of 0.75–1.0 mm. The containers were open to atmosphere at the top and had a port at the bottom for drainage and imbibition. The container chosen for containing a fully saturated porous medium was filled up with water, afterwards dry glass beads were slowly moved in from a hopper. The porosity was about 33%. The container to represent unsaturated conditions was filled up with dry glass beads, and then was wetted by raising the water table via the port at the bottom. The porosity was about 30%, which was determined by the known glass density, the inner volume of the container and the dry mass of glass beads. The water content was estimated gravimetrically and was lower than for the saturated set-up. The same porous medium was used to conduct a simple drainage experiment. The water content distribution in a container filled with the same glass beads was calculated. The average water content in the drained upper part of the container was 0.02 and 0.28 in the saturated lower part. In general, the grain size distribution affects the water content distribution, but also the shape and size of the capillary fringe.

The next step targeted plant experiments in thin containers. The size was a compromise between achieving a good contrast in the image (the thinner the better) and providing adequate space for germination and root development. The sensor foils for O<sub>2</sub> were

installed inside on the container walls. These types of sensors show short response times to changes in the environment in order of minutes or less, and seem completely reversible. The containers were made of glass because the optical transparency in the visible range was required for fluorescence imaging. Additionally, the glass chosen has a low attenuation for neutrons resulting in containers that were also transparent for the incoming neutrons. Firstly, we performed a series of experiments with plants in four containers that had dimensions of 0.1 m by 0.1 m by 0.01 m and were open to atmosphere at the top. The containers were filled homogeneously with quartz composed of 85% sand, 10% silt and 5% clay. White lupine (*Lupinus albus* L.) or blue lupine (*Lupinus angustifolius* L.) seeds were planted in the container.

The last set of experiments then looked at the most complex situation, with a plant grown in a structured soil in a similar way. Into a homogeneous quartz sand mixture (grain size distribution of 200–2000  $\mu\text{m}$ ) we built a layer of finer grained quartz sand (grain size distribution of 1 - 250  $\mu\text{m}$ ). The layer of finer sand was designed to block the lower compartment during drying from quick links to the gas phase in the upper part and thus the atmosphere. The two containers with internal dimensions of 0.15 m by 0.15 m by 0.01 m were planted with white lupine (*Lupinus albus* L.). The experiments were performed at the neutron radiography facility CONRAD at the Helmholtz Centre Berlin (HZB), Germany. The facility is located at the reactor based neutron source BER 2 and consists of a special beam collimator, a two-dimensional neutron detector and a cooled CCD camera (Fig. 3.2, left, A).

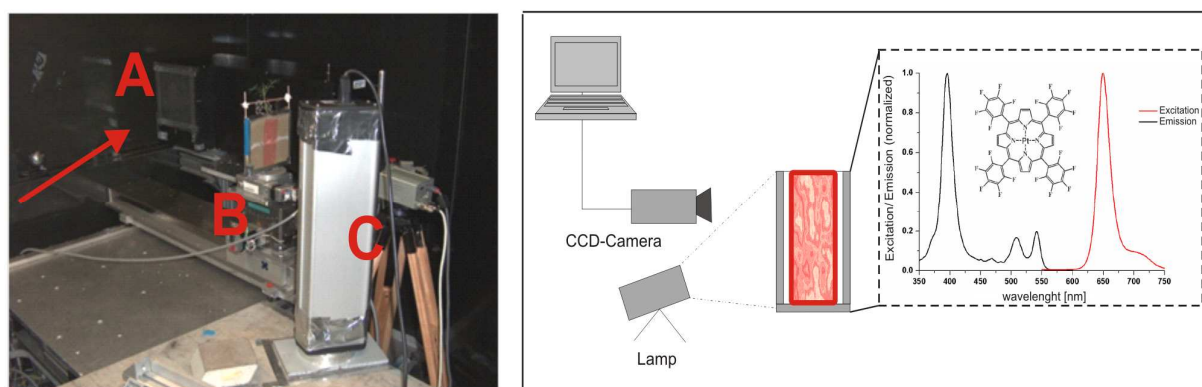


**Fig. 3.2** Coupled set-up for neutron radiography and fluorescence foil imaging (left). A: Position of sample in front of neutron detector with neutron beam direction as indicated by the arrow; B: sample on positioning table, rotated for optical imaging from the right; C: UV lamp and CCD camera. The sketch on the right outlines in detail the fluorescence foil imaging set-up.

A mobile plant growth cabinet (Vötsch, Balingen, Germany) was placed at the facility for the experiments. All plants were grown in containers starting from a single seed placed into the sand surface and watered to start germination. The plants were grown for two weeks with a daily photoperiod of 14 h (starting at 6 am to 8 pm), day temperature of 25°C, night temperature of 19°C, and relative humidity of about 60%. After a growing period of two weeks the samples were wetted from bottom. During five day and night cycles we took radiographies and imaged the root growth, water content, and oxygen distribution. For each sample an image, or image set, was taken every three hours during the day-night cycle to monitor intraday variations. To have an adequate illumination of the sample, the container usually is chosen smaller than the diameter of the beam. We could enable imaging the 0.15 m by 0.15 m containers, though larger than the maximum field of view of just 0.1 m x 0.1 m at CONRAD, by scanning 9 single images of an overlapping 3 by 3 array. In image processing the images were stitched together by applying the ImageJ plugin “TrakEM2” resulting in an image covering the full size of the container.

At the neutron imaging station CONRAD a special set-up was built inside the shielded area to enable automatic positioning of the equipment during operation (see Fig. 3.2, left). The samples were placed onto a positioning system to be able to move quickly and precisely between the position of the neutron radiography set up and the position for optical fluorescence imaging. At position A (see Fig. 3.2) the beam was transmitted through the sample, transferred into light impulses at the neutron detector and a built in CCD camera recorded the resulting image. In essence, grey-value images are taken with values proportional to the neutron flux behind the sample. The intensity of the neutron flux was recorded as a two-dimensional transmission map (image) for the sample positioned orthogonal to the beam (Strobl, Manke et al. 2009), and therefore the resulting image stores a water content value that is integrated in the beam direction over the thickness  $d$  of the container (Moradi, Conesa et al. 2009). Though also a three-dimensional tomography of these containers is possible (Esser, Carminati et al. 2010), this two-dimensional imaging set-up gave a higher temporal resolution that was essential for capturing the dynamics of the oxygen distribution changes. The sketch (see Fig. 3.2 right) describes in more detail the components of the fluorescence imaging part. The containers were illuminated by a UV lamp (typ 215L, Fa. Peqlab). The fluorescence was recorded by a CCD camera (type DX 4C-285, Kappa Optoelectronics) that provided a resolution of 1392 x 1040 pixels with 12 bit digitization. The CCD chip was cooled to -15°C to avoid thermal noise. The distance between the cameras and the container was 0.3 m. The UV lamp was placed next to the CCD camera at the height of

the sample to ensure homogeneous illumination and to prevent shadows. The dye was excited with high efficiency at the Soret band (~400 nm) and the emission maximum was located at ~650 nm. The excitation light and emission of the luminescent compound were separated by a 500 nm long-pass filter ([www.stemmer-imaging.de](http://www.stemmer-imaging.de)). For neutron radiography we used a field of view of 100 x 110 mm, obtaining an image of 2,048 x 2,048 pixels with pixel size of 0.054 mm. Fluorescence foil imaging achieved a camera resolution of 0.21 mm with a field of view of 258 x 221 mm.

### **3.3 Results**

The experiments investigated water content and oxygen concentrations in artificial porous media. We report in the following the results (i) in a homogeneously-packed glass bead medium without plant roots, (ii) in a homogeneously packed quartz sand with a plant, and (ii) for the most complex situation, with a plant grown in a structured soil, with an intermediate layer of finer grained quartz sand.

#### **3.3.1 Homogeneous porous media**

We mapped the oxygen concentration in a container homogeneously packed with glass beads of uniform size. Images were taken for saturated conditions and for unsaturated conditions, but close to saturation (Fig. 3.3; after 2 and 4 hours of diffusion). We monitored the oxygen content and observed reduced oxygen transport for unsaturated conditions. By comparing fully saturated conditions with the situation close-to-saturation, but containing trapped gas bubbles, we observed that small amounts of trapped gas can retard the movement of dissolved oxygen. A simple relationship to estimate the transport distance of diffusion is given by:

$$x^2 = 2Dt$$

where  $D = 1.2 \cdot 10^{-9} \text{ m}^2\text{s}^{-1}$  is the diffusion coefficient of oxygen in water accounting for the tortuosity of a porous medium (Huang, Oswald et al. 2003). The resulting distance 0.588 cm fitted perfectly the measured one given by the image (0.576 cm).

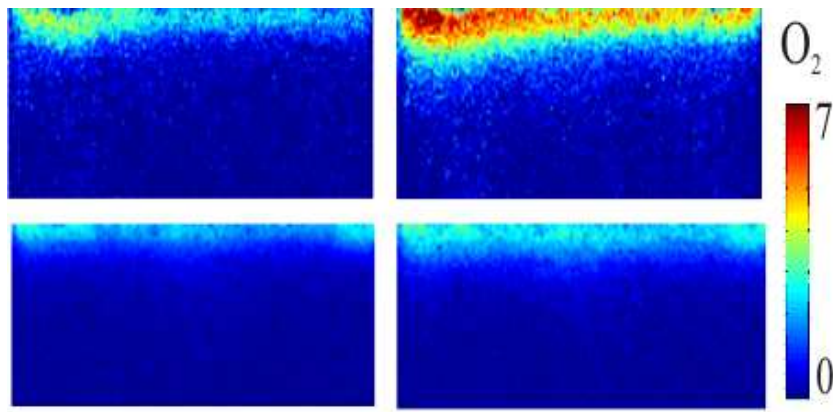


**Fig. 3.3** Oxygen concentration (mg/l) after 2 hours (left) and 4 hours (right) of oxygen diffusion from top in contact with atmosphere into the anaerobic water: in partly unsaturated glass beads, initially filled with nitrogen gas (bottom images), and in fully saturated glass beads (top images).

### 3.3.2 Homogeneous porous media with plant roots

The distribution of oxygen around the roots of a 14-day old lupine plant was measured, quasi simultaneously with the soil water content distribution obtained by neutron radiography (Fig. 3.4). The oxygen sensitive foil covered the central part of the container only. The left image in Fig. 4 shows the corrected neutron radiogram of the container, which captured the root structure, i.e. after 14 days of root development. The oxygen sensitive foil covers main parts of the root-system including tap root and lateral roots (as is illustrated in Fig. 3.4). These roots are clearly visible in the neutron radiogram. The observed oxygen patterns seem patchy and inhomogeneous. The combination with neutron radiography allows to judge if this was caused by plant roots growing inside the porous medium.

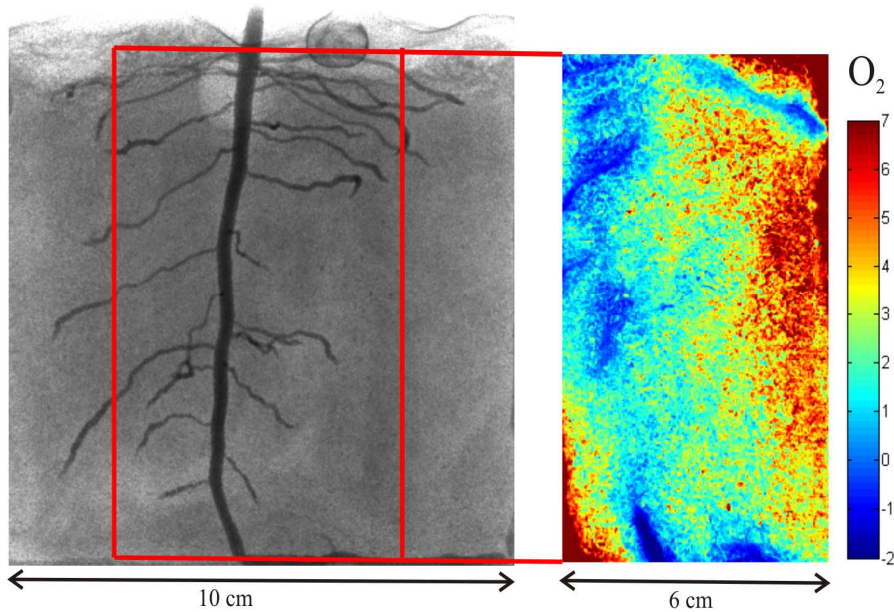


**Fig. 3.4** Container with lupine in a quartz sand captured by NR (corrected raw image, left) and position of the oxygen sensitive foil. Oxygen concentration in the rectangular area 2.5 hours after wetting (right).

By superimposing the segmented roots from neutron radiography on top of the fluorescence image, we could spatially match roots and oxygen concentration and highlight that the oxygen deficits occur around the roots. The oxygen maps indicated that the depletion of oxygen extended to distances of 2.94 mm from the root surface (see Fig. 3.4, right). This could be clearly identified by the spatial resolution of 0.21 mm.

The combined set-up enables us to capture day and night cycles concerning water content and oxygen distribution (Fig. 3.5). Uptake of water varied significantly between day and night. During a night cycle we monitored almost no change in the average water content, whereas during the following day the average water content dropped from 0.35 to 0.25. The related patterns of oxygen depletion were also monitored during a day and during a night (see Fig. 3.5, upper and lower row). Both represent conditions close to water saturation, because the samples were wetted directly before starting to monitor the oxygen depletion. The depletion zones started at the location of the tap root and largest lateral roots, and extended to the whole root-zone after a few hours. Oxygen depletion was similar at day and night, though it seemed a bit smaller and more diffuse during night time.

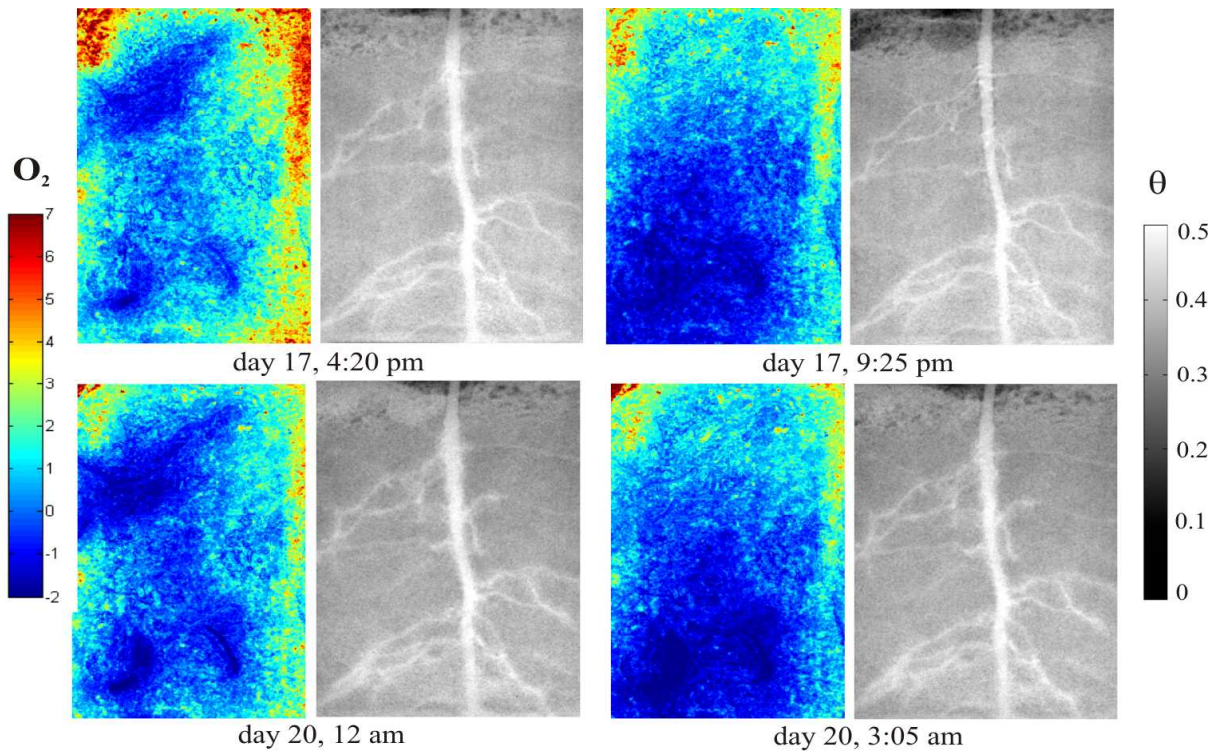


**Fig. 3.5** Time series of water content distribution in homogeneous porous media with lupine plant (left) and two according time series of oxygen patterns for the same sample (right) in mg/l; upper row shows a day cycle and lower row a night cycle.

The sensor foil consisting of polymeric substances influenced the neutron radiography images. The additional neutron attenuation of the foil created a higher background, which resulted in seemingly higher water content. Thus, at the area of the sensor foil we observed initially a slightly higher water content than the calculated average water content (about  $\theta = 0.05$ ). We have corrected for that effect by using a comparison of a reference zone inside and outside the area of the foil.

Fig. 3.6 shows a time series of oxygen deficit dynamics over 16 hours after watering the sample. We observed that the extension of oxygen depletion by respiration was not limited to the rhizosphere. The depletion zones developed and increased from local, patchy depletion patterns, close to the roots, to a diffuse pattern over a larger area after several hours. From day 14 at 3 pm to 10 pm the upper part of the container shows a slight re-aeration, limited to the top centimeters of sand. This could be related to decreasing water saturation by water losses due to evapotranspiration. Oxygen depletion was still increasing due to on-going respiration activities in the lower part of the container for some time. Then at day 15 at 7:20 am (see Fig. 3.6), comparing with the former image at day 14 at 9:50 pm, we observed that the oxygen concentration increased in all parts of the container, and the oxygen depletion zone was much smaller and weaker. Both images are separated by a night cycle, meaning little transpiration,



but ongoing respiration activity. By additionally taking into account the neutron radiography images, there is no change in the overall water content distribution, which is still high with an average water content of 0.37 for both images.

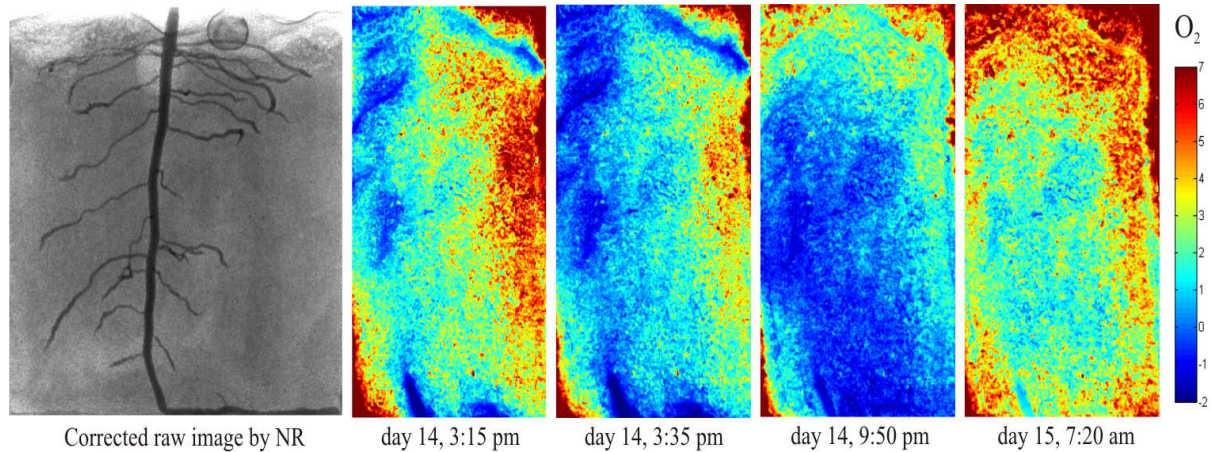


**Fig. 3.6** Time series of oxygen patterns (concentration in mg/l) induced by plant roots in a container with homogeneous porous medium.

### 3.3.3 Layered porous media with plant roots

The heterogeneous structure of soil is clearly visible in the water content images (Fig. 3.7). We observed a clear separation of water contents during drying of the soil that strongly reduced the water content in the upper part. This is essentially caused by the built in clay layer in the middle of the container. The finer grained clay held more water than the surrounding soil, which resulted in higher water contents. Moreover, this high water content in the clay layer limits the downward oxygen diffusion, which results in a generally low oxygen concentration compared to the coarser grained sand above, exposed to oxygen in the atmosphere. Since any oxygen exchange between the lower part and the atmosphere was limited by the clay layer, it is reasonable to assume that any change in oxygen concentration in the lower part of the container was linked to the activity of roots and soil microorganisms, plus potentially lateral diffusion of oxygen from the roots. The position of the oxygen sensitive foil is comparable with Fig. 3.4. The foil here also covered most of the main part of the root-system including the tap root and the laterals.

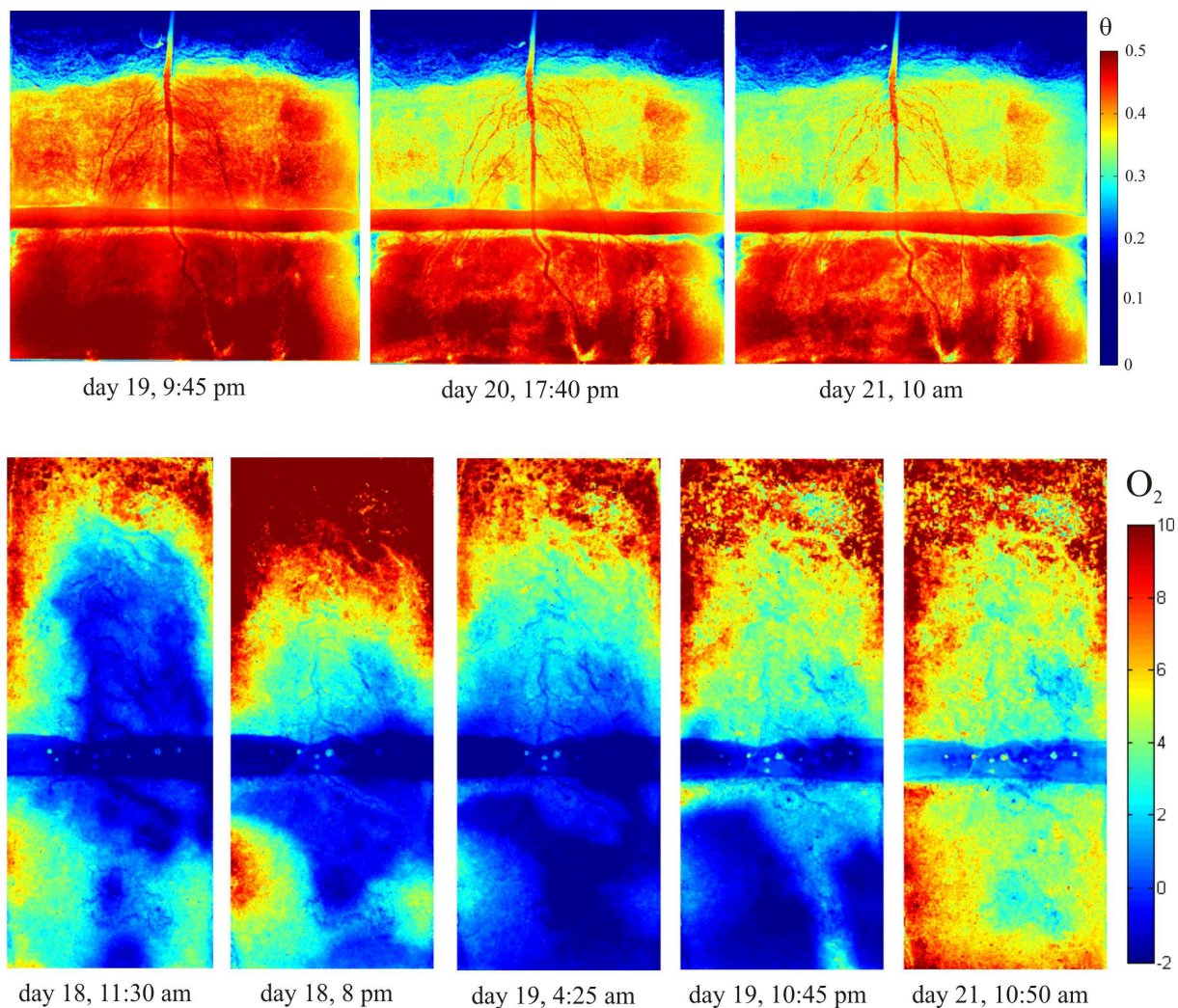


**Fig. 3.7** Time series of water content distribution in a container with a layer of fine quartz sand (upper row); corresponding distribution of oxygen (in mg/l) in the central area of the container where the oxygen sensing foil is installed (lower row).

We observed a decrease in water content in both compartments from day 19 to day 21 (see Fig. 3.7, upper row). The evapotranspiration was stronger in the upper compartment compared to the lower one, also because the root mass was much higher in the upper part. It can be concluded that water loss in the lower part was directly linked to root water uptake. The water content distributions on day 20 and day 21, respectively, showed reduced water contents around the roots compared to bulk soil. Comparing water content distributions from day 19 to day 20, again we could observe strong day and night variations. Due to physiological reasons (compare chapter 3.2) we expected and monitored reduced root water uptake rate during night. The average water loss in the samples with white lupine was 0.46 g per h during the photoperiod and 0.21 g per h during night. Containers planted with blue lupines had an average water loss of 0.42 g per h and 0.23 g per h during night. The averaged

water content in the lower compartment dropped from 0.50 to 0.46 between day 19 and day 21, respectively.

After rewetting (early morning of day 18) oxygen deficit zones formed, induced by respiration activity of the plant roots (see Fig. 3.7, lower row). The time series showed a decreased oxygen concentration at the positions of the roots. Moreover, the lower compartment showed increasing oxygen deficits. The oxygen concentrations decreased until morning of day 19, though in the upper part oxygen was re-entering already at day 18. Then, in the morning of day 19 at 10:45 pm, oxygen re-entered also in the lower part, along the position of the tap root. However, as it looks like this occurred starting from the bottom of the container, as visible between 4:25 am and 10:45 am. This correlated with a hole in the bottom at the right hand-side for wetting the sample. Thus, the seal seemed to have failed, probably because the tap root was growing into this opening. Without this connection at the bottom the oxygen deficit in the lower part may have lasted longer. The clay layer itself was depleted in oxygen until the last image at day 21.

The upper compartment was open to atmosphere and oxygen diffusion was only limited in case of high water saturation. Neutron radiography provided the information that the root density in the upper compartment was higher than in the lower one. Due to higher root density the water uptake was stronger than in the lower part. The oxygen deficit in the upper compartment increased until day 18 at 11:30 am due to high water content. In the following day cycle (starting with day 18 at 8 pm) we observed an oxygenation in the upper compartment, which could be explained by the decrease of the soil water content and resulting recovery of connected air phase and exchange of oxygen between the soil pores and the atmosphere. The slight decrease in oxygen in the upper compartment on day 19, 4:25 am could be due to the redistribution of soil water following the pausing of root water uptake. The next day cycle restarts the transpiration and results again in re-aeration of the upper part of the container.

### **3.4 Discussion**

Within the first set of experiments we showed that knowledge of water content distribution is important concerning the transport of oxygen. The simple set-up with partly saturated porous media visualized the strong coupling of both parameters. The mass transfer of oxygen for fully saturated reaching farther into the porous medium than in the presence of trapped gas bubbles (see Fig. 3.3). Oxygen will transfer from mobile aqueous phase and gas

phase by diffusion. Oxygen concentration gradients between both phases are the driving force until equilibrium is reached (Balcke, Meenken et al. 2007). At the gas-liquid interface, the mass transfer is controlled by the rate of diffusion of the oxygen across a thin layer assumed to exist at the phase interface (Donaldson, Istok et al. 1997). Though oxygen diffusion in the gas phase is much higher than in water, the trapped gas bubbles seem to act rather as a storage retarding the oxygen front than as a preferential pathway. This is different for connecting gas phase as can be seen in the other experiments.

The second set of experiments proved that the formation of oxygen deficits can be directly related to root activity, more specific to root respiration. The combination of neutron radiography and fluorescence dye imaging is able to simultaneously capture the concentrations of oxygen and water content. Moreover, the characteristics of the oxygen sensor give us the possibility to monitor dynamics of these parameters in-situ. This enables us to capture day and night variations in the root zone. Our experiments indicate that oxygen distribution in soils is highly variable in time and space and is related to water content and roots (see Fig. 3.5 and 3.6). Whereas only green tissues photosynthesize, all tissues respire, and they do so 24 hours a day. Thus, this oxygen depletion is to be expected and could now be monitored in more detail by the presented imaging approach.

The average water content from evening of day 14 to the morning of day 15 decreased slightly. It could be possible that the air phase just can form a connected gas filled pore network, probably by the larger pores present in the soil. This may not show up in the water content images, especially since the averaging of the two-dimensional neutron radiography over the thickness of the container will make this difficult to detect. If so, there is a connected network for the quick gas phase diffusion of oxygen, and oxygen from the atmosphere will replenish the oxygen in the soil. Thus, this could explain the increased oxygen values in spite of ongoing oxygen consumption due to respiration activity. Possibly even this threshold was already reached in the evening, but some more time was needed for the oxygen transfer from the atmosphere to greater depth to result in the observed changes. To sum up, oxygen depletion zones will result, provided that gas phase re-supply of oxygen is limited due to high water content. Further investigations are needed to differentiate the effect of plant roots and soil structure of oxygen movement in soil.

The third, most complex set-up presented in this study confirms the applicability for the combined approach. The experimental set up was able to visualize patches of different grain size distributions and roots. Natural soils are highly heterogeneous and the third set of experiments showed the application also to a structured soil (see Fig. 3.7). Again, these

experiments showed the strong interrelation between root water uptake forced by transpiration activity, oxygen depletion induced by root respiration, and soil structure. Besides mass transfer of oxygen between liquid and gas phase had an influence on the observed patterns. Closer experiments on the interaction of oxygen change and water content distributions are necessary to better understand how and where plants react on oxygen limitations.

Combining fluorescence dye imaging with neutron radiography, which is highly sensitive for water, shows a minor drawback. The supporting foils for fluorescence imaging are visible in neutron radiography, because the foils consist of an organic polymer that absorbs neutrons efficiently, similar to water. A background correction for the additional attenuation by the foil was applied, and may be necessary for some set-ups and some facilities to give accurate water content values, and may not be necessary for others. Also, the fluorescence dye layer could be manufactured on different substrates, e.g. directly on glass, which should result in a much lower background.

Combining neutron radiography and fluorescence imaging could be most effective by targeting a spatial resolution around 200  $\mu\text{m}$ , i.e. less than the possible 54  $\mu\text{m}$  resolution achieved as described in this study. This could allow for imaging larger areas and the obtained water content distributions in combination with fluorescence dye imaging should still be sufficient to allow a similar interpretation as the one presented here.

The experiments have demonstrated that by this novel methodology it is possible to monitor, with high spatial and temporal resolution, the dynamics of oxygen and water in the rhizosphere as an interface between soil and roots. The rhizosphere is accepted to be an area around the roots where most of biological activities occur in soil (Hinsinger, Bengough et al. 2009). Moreover, the rhizosphere is home to most of the soil microorganisms that feed on decomposing root residue and root exudates on organic materials. Besides root respiration, microbial induced oxygen consumption may have had a major effect on the observed oxygen distributions.

Both imaging methods work in quantitative way and gave meaningful results. In spite of the averaging character of two-dimensional radiography and the sensor foil being in contact with the lateral soil surface, the results demonstrate that the processes and dynamics inside soil can be visualized. Thus, zones of oxygen depletion could be mapped and linked to root respiration, plant transpiration and water content distribution.

### 3.5 Conclusions

Within this study we presented a methodology with fluorescence dye imaging to map the changes in oxygen concentration in soil-root systems, which is also applicable to natural soils with plants. As a second step we already coupled the optical imaging with highly sensitive neutron radiography to monitor the water content distribution of the same sample at nearly the same time. The formation of the observed oxygen depletion zones is highly sensitive to the water content distribution, because zones with high water saturation are able to block the supply of oxygen via the soil gas phase. Therefore, the major advantage of this combined approach is that the oxygen dynamics and changing patterns of oxygen depletion and oxygen availability can be interpreted in a more profound and meaningful way.

Generally, the presented fluorescence foil imaging method is applicable to porous media with focus on soil structure, sediments or microbes. Moreover, one great advantage of fluorescence dye imaging is the broad range of adaptability. Besides oxygen, temperature, pH, or CO<sub>2</sub> gradients are other important biogeochemical parameters. Concerning vital parameters of plants, e.g. pH is also of interest, because of the strong correlation between pH, water, oxygen and root activity in the rhizosphere (i) water uptake by plant roots is negatively influenced by increasing pH; (ii) anaerobic conditions cause a decrease in respiration activity and this in turn increases the pH (Tournaire-Roux, Sutka et al. 2003); (iii) root exudates directly modify pH and thus trace metal availability. The fluorescence dye imaging method has the potential for visualization of pH and oxygen, and possibly other parameters, in the root zone, soils or sediments; even at the same time, which could be achieved by fluorescent multisensing (Nagl and Wolfbeis 2007). As presented here, also water content can be simultaneously mapped, if optical imaging is combined with neutron radiography.

**Acknowledgements** We acknowledge funding from the DFG priority program 1315 “Biogeochemical interfaces in soil”, under contract OS 351/1-2, and the support from the Helmholtz-Centre for Environmental Research – UFZ, departments Hydrogeology and Soil Physics.

## References

- Amao, Y. and I. Okura (2000). "An oxygen sensing system based on the phosphorescence quenching of metalloporphyrin thin film on alumina plates." Analyst **125**(9): 1601-1604.
- Bacon, J. R. and J. N. Demas (1987). "Determination of Oxygen Concentrations by Luminescence Quenching of a Polymer-Immobilized Transition-Metal Complex." Analytical Chemistry **59**(23): 2780-2785.
- Balcke, G. U., S. Meenken, et al. (2007). "Kinetic gas-water transfer and gas accumulation in porous media during pulsed oxygen sparging." Environmental Science & Technology **41**(12): 4428-4434.
- Baleizao, C., S. Nagl, et al. (2008). "Dual fluorescence sensor for trace oxygen and temperature with unmatched range and sensitivity." Analytical Chemistry **80**(16): 6449-6457.
- Blossfeld, S. and D. Gansert (2007). "A novel non-invasive optical method for quantitative visualization of pH dynamics in the rhizosphere of plants." Plant Cell and Environment **30**(2): 176-186.
- Borisov, S. M., A. S. Vasylevska, et al. (2006). "Composite luminescent material for dual sensing of oxygen and temperature." Advanced Functional Materials **16**(12): 1536-1542.
- Brune, A., P. Frenzel, et al. (2000). "Life at the oxic-anoxic interface: microbial activities and adaptations." Fems Microbiology Reviews **24**(5): 691-710.
- Carminati, A. and H. Fluhler (2009). "Water Infiltration and Redistribution in Soil Aggregate Packings." Vadose Zone Journal **8**(1): 150-157.
- Carraway, E. R., J. N. Demas, et al. (1991). "Luminescence Quenching Mechanism for Microheterogeneous Systems." Analytical Chemistry **63**(4): 332-336.
- Carraway, E. R., J. N. Demas, et al. (1991). "Photophysics and Photochemistry of Oxygen Sensors Based on Luminescent Transition-Metal-Complexes." Anal Chem **63**: 337-342.
- Deinert, M. R., J. Y. Parlange, et al. (2004). "Measurement of fluid contents and wetting front profiles by real-time neutron radiography." Journal of Hydrology **290**(3-4): 192-201.
- Demas, J. N., B. A. Degraff, et al. (1995). "Modeling of Luminescence Quenching-Based Sensors - Comparison of Multisite and Nonlinear Gas Solubility Models." Analytical Chemistry **67**(8): 1377-1380.
- Donaldson, J. H., J. D. Istok, et al. (1997). "Development and testing of a kinetic model for oxygen transport in porous media in the presence of trapped gas." Ground Water **35**(2): 270-279.
- Esser, H. G., A. Carminati, et al. (2010). "Neutron radiography and tomography of water distribution in the root zone." Soil Plant Nutrients **accepted**.
- Fuller, Z. J., W. D. Bare, et al. (2003). "Photostability of luminescent ruthenium(II) complexes in polymers and in solution." Analytical Chemistry **75**(11): 2670-2677.
- Glud, R. N., N. B. Ramsing, et al. (1996). "Planar optodes: A new tool for fine scale measurements of two-dimensional O<sub>2</sub> distribution in benthic communities." Marine Ecology-Progress Series **140**(1-3): 217-226.

- Glud, R. N., C. M. Santegoeds, et al. (1998). "Oxygen dynamics at the base of a biofilm studied with planar optodes." Aquatic Microbial Ecology **14**(3): 223-233.
- Hassanein, R. K. (2006). "Correction methods for the quantitative evaluation of thermal neutron tomography." Dissertation ETH Zurich(Switzerland).
- Hinsinger, P., A. G. Bengough, et al. (2009). "Rhizosphere: biophysics, biogeochemistry and ecological relevance." Plant and Soil **321**(1-2): 117-152.
- Huang, W. E., S. E. Oswald, et al. (2003). "Dissolved oxygen imaging in a porous medium to investigate biodegradation in a plume with limited electron acceptor supply." Environ Sci Technol **37**(9): 1905-1911.
- Jensen, S. I., M. Kuhl, et al. (2005). "Oxic microzones and radial oxygen loss from roots of *Zostera marina*." Marine Ecology-Progress Series **293**: 49-58.
- Kardjilov, N., A. Hilger, et al. (2005). "Industrial applications at the new cold neutron radiography and tomography facility of the HMI." Nuclear Instruments & Methods in Physics Research Section a-Accelerators Spectrometers Detectors and Associated Equipment **542**(1-3): 16-21.
- Klimant, I., V. Meyer, et al. (1995). "Fiberoptic Oxygen Microsensors, a New Tool in Aquatic Biology." Limnology and Oceanography **40**(6): 1159-1165.
- Lehmann, E., H. Pleinert, et al. (1999). "Application of new radiation detection techniques at the Paul Scherrer Institut, especially at the spallation neutron source." Nuclear Instruments & Methods in Physics Research Section a-Accelerators Spectrometers Detectors and Associated Equipment **424**(1): 158-164.
- Liebsch, G., I. Klimant, et al. (2000). "Luminescence lifetime imaging of oxygen, pH, and carbon dioxide distribution using optical sensors." Applied Spectroscopy **54**(4): 548-559.
- Liebsch, G., I. Klimant, et al. (1999). "Luminescence lifetime temperature sensing based on sol-gels and poly(acrylonitrile)s dyed with ruthenium metal-ligand complexes." Advanced Materials **11**(15): 1296-+.
- Luster, J., A. Gottlein, et al. (2009). "Sampling, defining, characterising and modeling the rhizosphere-the soil science tool box." Plant and Soil **321**(1-2): 457-482.
- Matsushima, U., W. B. Herppich, et al. (2009). "Estimation of water flow velocity in small plants using cold neutron imaging with D2O tracer." Nuclear Instruments & Methods in Physics Research Section a-Accelerators Spectrometers Detectors and Associated Equipment **605**(1-2): 146-149.
- Mills, A. and A. Lepre (1997). "Controlling the response characteristics of luminescent porphyrin plastic film sensors for oxygen." Analytical Chemistry **69**(22): 4653-4659.
- Moradi, A. B., A. Carminati, et al. (2011). "Three-dimensional visualization and quantification of water content in the rhizosphere." New Phytologist in revision.
- Moradi, A. B., H. M. Conesa, et al. (2009). "Neutron radiography as a tool for revealing root development in soil: capabilities and limitations." Plant and Soil **318**(1-2): 243-255.
- Nagl, S., C. Baleizao, et al. (2007). "Optical sensing and imaging of trace oxygen with record response." Angewandte Chemie-International Edition **46**(13): 2317-2319.
- Nagl, S. and O. S. Wolfbeis (2007). "Optical multiple chemical sensing: status and current challenges." Analyst **132**: 507-511.



- Oswald, S. E., M. Menon, et al. (2008). "Quantitative imaging of infiltration, root growth, and root water uptake via neutron radiography." Vadose Zone Journal **7**(3): 1035-1047.
- Precht, E., U. Franke, et al. (2004). "Oxygen dynamics in permeable sediments with wave-driven pore water exchange." Limnology and Oceanography **49**(3): 693-705.
- Schröder, C. R., L. Polerecky, et al. (2007). "Time-resolved pH/pO<sub>2</sub> mapping with luminescent hybrid sensors." Analytical Chemistry **79**(1): 60-70.
- Schroeder, C. R., L. Polerecky, et al. (2007). "Time-resolved pH/pO<sub>2</sub> mapping with luminescent hybrid sensors." Analytical Chemistry **79**(1): 60-70.
- Strobl, M., I. Manke, et al. (2009). "Advances in neutron radiography and tomography." Journal of Physics D-Applied Physics **42**(24): -.
- Tournaire-Roux, C., M. Sutka, et al. (2003). "Cytosolic pH regulates root water transport during anoxic stress through gating of aquaporins." Nature **425**(6956): 393-397.
- Tumlinson, L. G., H. Liu, et al. (2008). "Thermal Neutron Computed Tomography of Soil Water and Plant Roots." Soil Sci Soc Am J **72**: 1234-1242.

## Chapter 4

# Simultaneous visualization of oxygen depletion zones and water content distribution in artificial soil structures<sup>3</sup>

*Heterogeneity in soil is a general feature and enhances the patchiness of biogeochemical parameters besides many others including oxygen and water. Dissolved oxygen is needed for respiration of plants and animals and a primary electron acceptor for microbes which may be depleted during biodegradation. Limited availability of oxygen restricts their respiration activity and in turn this limits biodegradation. The development of anoxic subzones is additionally stimulated by the low solubility of oxygen in water and low water diffusivities. Therefore the oxygen distribution, and especially the oxygen gradients, resulting from microbiological and plant activities and their visualization are a good tool for understanding the diffusive recharge. Autooxidation of alkaline pyrogallol with a reaction rate set by the aqueous pH, was used to mimic microbial oxygen demand.*

---

<sup>3</sup> An article with equivalent content is in preparation for Geoderma as:

N. Rudolph, S. Nagl, P.Vontobel, S.E. Oswald (2013): Simultaneous visualisation of oxygen depletion zones and water content distribution in artificial soil structures.

## 4.1 Introduction

Soil is a complex medium with high spatial and temporal environmental variability at a wide range of scales. Soils develop as a critical zone between the biosphere, hydrosphere, atmosphere, and lithosphere (Rennert et al. 2012). The different contacting organic, inorganic, and biological components define a complex and large biogeochemical interface (BGI) to the soil's liquid and gaseous phases (Young and Crawford 2004). This BGI is three-dimensional of varying thickness and continuously transformed by the interplay of soil biota (Totsche et al. 2012). Biogeochemical interfaces in soil can exhibit biological, chemical and physical gradients concerning from a scale of nanometers to decimetres. These gradients affect processes in soil, e.g. water retention (Whalley et al. 2005), or root growth (Hinsinger et al. 2009).

Soil structure or spatial heterogeneity dominates almost all properties of soils and hence, its functioning (Dexter 1997). Especially aggregates and layers are important structural features. Soils, even sandy soils with some salts tend to form aggregates (Horn and Peth 2009). Aggregation is crucial for the movement of water, gas and solutes because it enhances soil aeration, infiltration and storage of water (Carminati et al. 2008). Under normal conditions, water is stored by capillarity within aggregates and layers. This waterlogging may impair oxygen supply in the inner part of the aggregates and layers and affect the biological activity and mineralization of plant nutrients (Lipiec et al. 2007). Moreover, oxygen diffusion to sinks (soil microbial respiration or plant root respiration) takes place in the interaggregate pores and is controlled by the concentration gradients resulting from respiration (Horn and Peth 2009). The limited oxygen transport in the inner parts of the aggregates is due to the higher water content and therefore limited diffusion. Soils with strong layering show similar behavior, the change from finer pores to larger pores produce layered water distribution patterns (Oswald et al. 2008b). Furthermore, the occurrence of layers with lower diffusivity only few centimetres thick have been reported to reduce gas diffusion fluxes by several orders of magnitude (Kristensen et al. 2010). These examples indicated the necessity to measure water content and oxygen distribution simultaneously.

The impact of soil structure, how it controls or modulates the distribution, flow and retention of water, solutes, gases and biota, in agricultural and natural ecosystems, is relatively unquestioned (Young et al. 2001). Since most of these processes are dynamic non-destructive, non-invasive methods to observe them are desirable. Moreover, due to the destructive character of conventional methods, it is difficult to assess the spatial and temporal

dynamics of the variables of interest. Recently, we introduced a novel imaging setup which combined neutron radiography, sensitive to water dynamics, and fluorescence imaging, sensitive to oxygen concentrations to simultaneously map the distribution of both biogeochemical parameters (Rudolph et al. 2012).

Dissolved oxygen in soil solution can be detected by water sampling (and subsequent analysis), electrical methods or directly with external optodes by commercially available devices, but these are all localized measurement methods. Optodes are thin sensor foils where a dye is incorporated in a polymeric matrix. Its production procedure is described elsewhere (Baleizao et al. 2008; Borisov et al. 2006; Schröder et al. 2007). Application ranged from studies of the O<sub>2</sub> dynamics at the base of a biofilm in aquatic systems (Glud et al. 1998) to studies of the microdistribution of O<sub>2</sub> and the radial oxygen loss (ROL) from roots of *Zostera marina* (Jensen et al. 2005). At the interface water and sediments in marine systems Precht et al. (2004) looked at oxygen distribution in permeable sediments forced by advective pore water exchange. Practically all optical sensors for oxygen rely upon quenching of luminescence by oxygen; higher oxygen levels result in lower intensity (Carraway et al. 1991a). For oxygen sensing, the choice of oxygen probes (iridium(III), platinum(II) and palladium(II) phorpyrin complexes, fullerene) and oxygen-permeable materials are importance since they adjust the sensitivities of the resulting sensor (Baleizao et al. 2008; Borisov et al. 2011b; Mayr et al. 2009). For example, Platinum(II) phorpyrin cover a dynamic range between 0.3 – 1000 Pa when embedded into silica-gel (Borisov et al. 2011a) which increased to 13 kPa when embedded into cellulose acetate (Mills and Lepre 1997).

There are several imaging techniques to study the water content distribution in porous media. This can be done by light transmission e.g. (Niemet and Selker 2001), light reflection e.g. (Lazik et al. 2008), X-ray transmission or CT-tomography e.g. (Pierret et al. 2003) or by nuclear magnetic resonance e.g. (Votrubova et al. 2003). But the most recent and sensitive one is neutron radiography, that can be used to study infiltration pattern in porous media (Deinert et al. 2004; Oswald et al. 2008b). For example, Carminati et al. (2009) showed the possibility of using neutron radiography to image infiltration and redistribution of water through aggregate packing. Since it is difficult to access the spatial distribution of oxygen and water content simultaneously we developed a non-invasive imaging approach. Recently, we coupled neutron radiography with fluorescence foil imaging to simultaneously capture the dynamics of oxygen and water content distribution at the root soil interface (Rudolph et al.

2012). Whereas the usual sizes of commercially available optodes are in the range of 1 cm in diameter, our method offers the possibility to cover areas of 10 x 15 cm.

We are interested in the formation of interfaces due to the interrelated pattern of water and oxygen distribution in soils. We address the complex interplay and interdependencies of chemical, biological and physical processes of interfaces. Understanding and visualisation the architecture of biogeochemical interfaces in soil have been identified as emerging challenge in soil science (Totsche et al. 2010). Aggregates and layers are of major interest because they partly control the spatial distribution and bioavailability of solutes and gases in soil. It has been shown that neutron radiography is a powerful tool the study water content dynamics. Moreover, we proved that the fluorescence imaging method is an easy and low cost method to gain highly-resolved oxygen distribution data. Our approach (Rudolph et al. 2012) is the application of the combined techniques to visualize the dynamic relationship between water content and oxygen transport in an artificial structured soil.

## 4.2 Materials and methods

### 4.2.1 Fluorescence imaging

The relationship between oxygen partial pressure, in a gas or liquid, and the concentration of oxygen can be calculated from the partial pressures by means of Henry's Law:

$$c(X) = K_H(X) * p_X \quad [1]$$

Where  $c_X$  represents the concentration in mol L<sup>-1</sup>,  $p_X$  the partial pressure of oxygen, respectively and  $K_H(X)=1.24*10^{-6}$  mol L<sup>-1</sup> hPa<sup>-1</sup> (T=25°C) the Henry constant. The response is usually evaluated through changes in fluorescence intensity, lifetime, or spectral distributions (Fuller et al. 2003). Lifetime-based sensing has the advantage of being independent of the intensity of excitation light and is self-referenced. However, the setup and the data acquisition is complex and expensive (Stich et al. 2010). Intensity based sensing is simple and requires inexpensive instruments but homogeneous illumination is essential (Stich et al. 2010). As can be observed (Figure 1, small Figure), the Stern-Vollmer plot is not linear indicating localization of the indicator in two regions having substantially different microenvironments (Carraway et al. 1991b). The so called "two-site model" is commonly used to describe such behavior:

$$\frac{I_0}{I} = \left( \frac{f_1}{1 + K_{SV1}[O_2]} + \frac{f_2}{1 + K_{SV2}[O_2]} \right)^{-1} \quad [2]$$

where  $f_i$  is the fraction of the total emission from each component (with  $f_1 + f_2 = 1$ ) and the  $K_{SVi}$  is the associated Stern-Vollmer quenching constant for each component (Carraway et al. 1991b). However, it has been shown that oxygen probes dissolved in polystyrene can be described by a slightly adapted Stern-Vollmer equation (Klimant et al. 1995):

$$\frac{I_0}{I} = \left( \frac{f}{1 + K_{SV}[O_2]} + 1 - f \right)^{-1} \quad [3]$$

The basic assumption for using Eq. 3 is that the fluorescence of a fraction of the indicator is not quenched significantly by oxygen (Klimant et al. 1995).

*Preparation.* The sensor for oxygen mapping was prepared by dissolving 20 mg platinum (II) 5,10,15,20-tetrakis(2,3,4,5,6-pentafluorophenyl)porphyrin (PtTFPP) purchased from Porphyrin Systems ([www.porphyrin-systems.de](http://www.porphyrin-systems.de)) and 1.98 g of polystyrene (Sigma-Aldrich, Germany) in 18 g of toluene (Sigma-Aldrich, Germany). The sensor matrix was stirred over night, and knife-coated into a 75  $\mu\text{m}$  polyester support (Melinex 505, [www.puetz-folien.de](http://www.puetz-folien.de)). After solvent evaporation at ambient air, the resulting sensor foils are in the range of 10  $\mu\text{m}$  thickness. Platinum (II) complex (PtTFPP) is known for its excellent photostability because of the fluoro-substituents of the phorphyrin ligand (Schröder et al. 2007).

*Calibration.* Temperature is particularly important in fluorescent sensing since quenching by oxygen is always temperature dependent (Baleizao et al. 2008). At constant temperature, oxygen-free water shows the strongest fluorescence intensity. Sodium dithionite ([www.de.vwr.com](http://www.de.vwr.com)) was used to create oxygen-free water. The calibration of the sensor matrix was performed at room temperature (21°C) with determination of the fluorescence intensity of the dye at several oxygen concentration levels. It was conducted under conditions comparable to the following experiments. The container was filled with the same porous medium and flushed with water of different oxygen concentration. The fluorescence intensity of the oxygen indicator versus oxygen concentration is displayed in Fig. 4.1. The adapted Stern-Volmer equation described in Eq. 3 was used to fit the data. The model fitted the experimental data exceptionally well for the range of oxygen pressures relevant for the experiment.

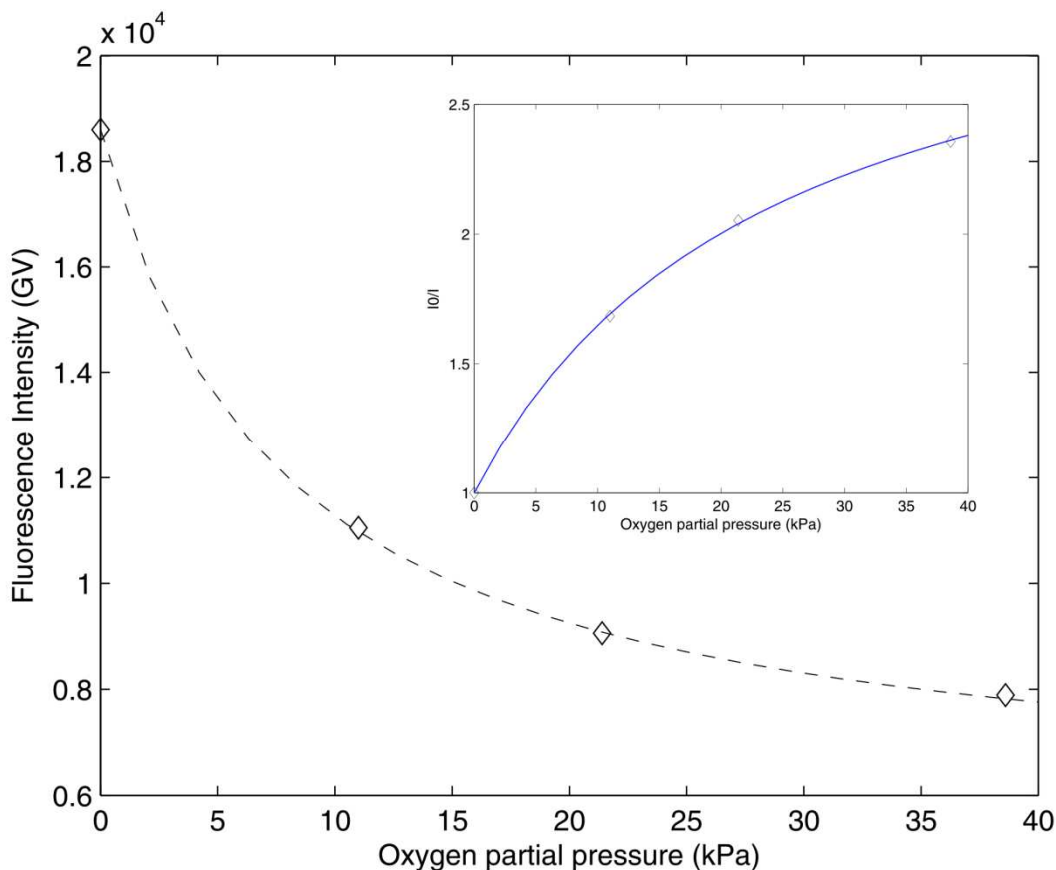


**Fig. 4.1:** The calibration curve of Pt-PFPP foil for various oxygen partial pressures and intensity based Stern-Volmer plot for the oxygen sensor (in-set)

#### 4.2.2 Kinetics of pyrogallol autooxidation

Anoxic pyrogallol (1,2,3-trihydroxybenzene, Sigma Aldrich) solution was used as reactant for chemical induced oxygen consumption. Pyrogallol reacts quickly with oxygen in alkaline solutions by changing the color of the solution from transparent to brown. Pyrogallol [A] reacts with dioxygen in alkaline solutions to form purpurogallin [B] which then forms the blue transient dianion of purpurogalloquinone [C] and then species [D] (Abrash et al. 1989).

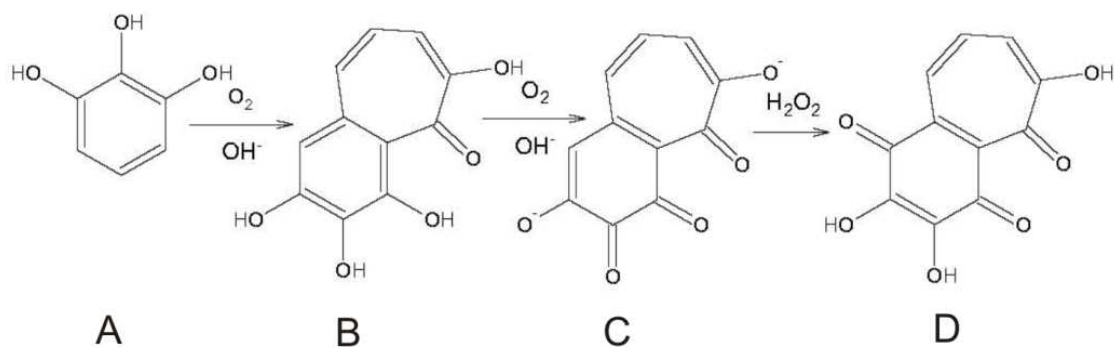


**Fig. 4.2:** Reaction mechanism for pyrogallol oxidation suggested by Abrash et al. (1989)

Previously, the autoxidation rate was shown to be pH dependent and the rate of dissolved oxygen consumption can be described according to the following stoichiometric equation (Doona and Kustin 1993):



The use of pyrogallol as an oxygen sensitive tracer was found to offer an advantage in that the reduced form can be handled under atmospheric conditions at neutral pH without precaution against oxidation (Oswald et al. 2008a). Moreover, pyrogallol and its oxidation products showed nearly conservative transport behavior in aqueous solution. Oswald and co-workers (2008a) showed that the oxygen demand rate  $k=3.6 \text{ h}^{-1}$  at pH 7.5 increases to  $k=69.9 \text{ h}^{-1}$  at pH 9. For preparation, aqueous 0.15 M air-saturated TRIS (trishydroxyaminomethane, Sigma Aldrich) buffer with a pH value of 7.6 were used. A typical kinetic experiment involved adding 1 ml of 0.02 M pyrogallol solution to 30 ml TRIS buffer. Variations in this procedure are: (1) adding either air saturated or nitrogen purged buffers; (2) using different volumes of solution to create various water contents; and (3) using coarser or finer grained material as background soil. All variations are listed in Table 4.1. Beside the chemical reaction, pyrogallol solution was used also to volumetrically adjust water content.

**Table 4.1:** Summary of the conducted experiments including the physical properties volumetric water content, air-filled porosity and porosity

	<b>Background material</b>	<b>structure</b>	$\theta_{vol}$	$\Phi$	$\theta_a$	<b>TRIS buffer</b>
<b>V1</b>	1 – 2 mm	layer	0.18	0.41	0.23	Air-sat
<b>V2</b>	1 – 2 mm	layer	0.26	0.43	0.17	Air-sat
<b>V3</b>	1 – 2 mm	layer	0.27	0.45	0.18	N <sub>2</sub> -sat
<b>V4</b>	0.2 – 1 mm	layer	0.27	0.43	0.16	Air-sat
<b>V5</b>	1 – 2 mm	aggregate	0.26	0.43	0.17	Air-sat

### 4.2.3. Experimental description

The containers used in this study were made of boron-free glass with inner size of 10 x 10 x 1.5 cm (height x width x thickness). All containers were open to the atmosphere at the top and had a port for drainage and imbibition at the bottom. The containers were equipped with oxygen sensitive foil attached to one inner-side and filled with quartz sand, using



different grain size distribution in varying experiments (see Table 4.1). Into a homogeneous quartz sand matrix we built structures (layers and aggregates) of finer-grained quartz sand (grain size distribution 1 – 250  $\mu\text{m}$ ). Aggregates had a round shape and dimensions of approximately 1 cm in diameter. Constructed layers had a length of 6 cm and a height of 1 cm (see Figure 4.3). Pyrogallol solution was infiltrated via the port at the bottom, by which also different water contents in the container were adjusted (see Figure 4.3). Porosity, average volumetric water content and air-filled pore space were calculated by the known quartz sand density, the inner volume of the container, the dry mass of the quartz sand, and the mass of water added via pyrogallol solution. Table 4.1 summarizes the parameters of all conducted experiments.

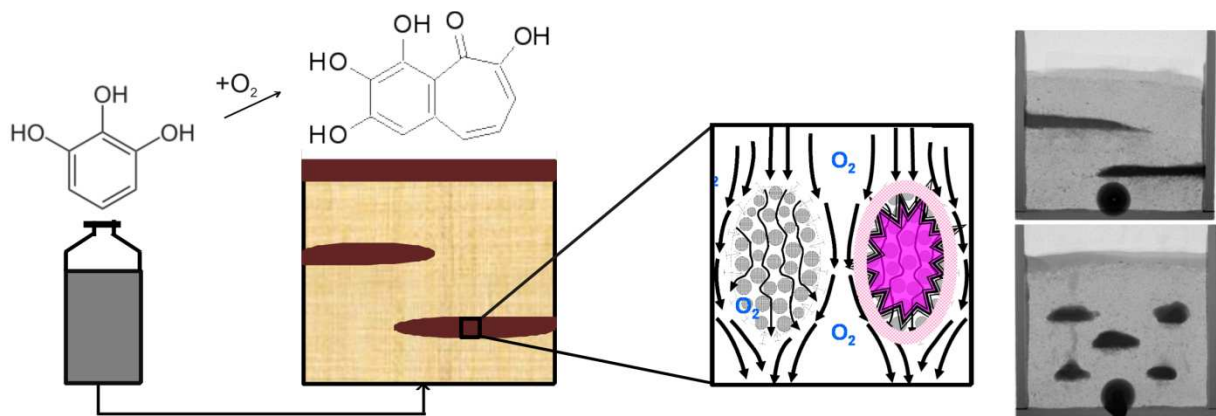


**Fig. 4.3:** Sketch of setup for oxygen depletion experiments (left) and two raw images captured with neutron radiography showing the location of the constructed aggregates and layers (right)

Neutron radiography was performed at the thermal neutron imaging facility NEUTRA, at Paul Scherrer Institute (PSI), Villigen, Switzerland. Neutron radiography is very sensitive to hydrous materials, making water easily visible (Menon et al. 2007). The setup consists of a collimated neutron beam guided through the sample. The neutron beam intensity behind the sample is detected by a scintillator plate and contains the information about mass and thickness of the sample components. The transmission images were corrected for scattering, beam fluctuations, detector non-uniformities, and camera noise using the quantitative neutron imaging (QNI) algorithm (Hassanein 2006). After correction, the intensity of the transmitted neutron beam through the sample is described by the exponential law taking into account the individual attenuation coefficients of the sample:

$$-\log \left[ \frac{I(x, z)}{I_0(x, z)} \right] = \Sigma_{cont} L_{cont}(x, z) + \Sigma_{H_2O} L_{H_2O}(x, z) + \Sigma_{soil} L_{soil}(x, z) \quad [5]$$

The subscript *cont* refers to the container, *H<sub>2</sub>O* to water, and *soil* to the dry soil (quartz). The attenuation coefficient of water is calculated by QNI software. Then, rearranging Eq. [5], we calculate  $L_{H_2O}(x, z)$ . The water content  $\theta$  is defined as:

$$\theta(x, z) = \frac{L_{H_2O}(x, z)}{L_{tot}(x, z)} \quad [6]$$

where  $L_{tot}(x, z)$  is the sample thickness. Eq. [6] yields the water content averaged along the beam direction (Carminati and Fluhler 2009). For this study, we expect that the two-dimensional average of the water content is sufficient to compare the data with the fluorescence images. For more details of the radiography setup, imaging parameters, image correction, and calculation of water content see Carminati et al. (2010) and Rudolph et al. (2012). By the procedure, the structure in soil can be identified clearly and the water content of the soil can be calculated precisely for all pixels. The soil water content was calculated using Matlab (Matlab R2010a). At the neutron imaging station NEUTRA, a special setup was built inside the shielded area to enable automatic positioning of the equipment during operation identical to Rudolph et al. (2012). For neutron radiography, we used a CCD camera detector with an array of 2,048×2,048 pixels with pixel size of 0.149 mm. For the fluorescence foil imaging a camera resolution of 0.188 mm could be achieved.

### 4.3 Results and Discussion

The development of oxygen depleted zones inside two single constructed aggregates is visualized in Figure 4.4. The respective radiograph was taken 24h after experimental duration. After 24 hours the water is equilibrated and we can see the closing layer at the top is water saturated that prevents re-aeration from atmosphere. Moreover, the radiograph shows that all aggregates are water saturated. The calculated volumetric water content ( $\theta_v=0.26 \text{ cm}^3/\text{cm}^3$ ) corresponds well with the radiograph that shows in more detail the distribution of water. The heterogeneous distribution of water inside the sandy matrix creates in different conditions for the aggregates at different locations.

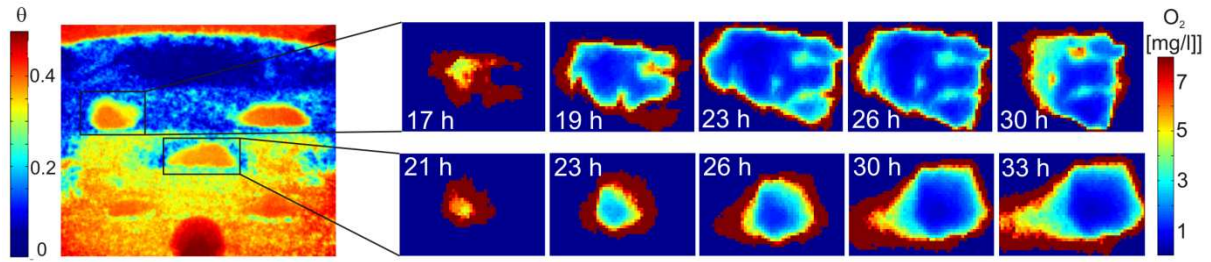


**Fig. 4.4:** Water content distribution in a constructed aggregated soil (left) and time series of oxygen concentration changes resulting from chemical oxygen consumption in two aggregates

Aggregate 1 (upper row) has a direct contact to air-filled pore space as the upper boundary with  $\theta_v < 0.10 \text{ cm}^3/\text{cm}^3$  and direct contact to the water-filled pore space as lower boundary with  $\theta_v > 0.20 \text{ cm}^3/\text{cm}^3$ . Oxygen depletion becomes evident 17 h after start of the experiment. Chemical induced oxygen consumption induced depletion zones with minimum oxygen concentration of 0.58 mg/l after 23 h of experimental duration. The maximum extent of the depletion zone was reached within the first 26 h followed by decrease within the next 4 h until the depletion zone disappears (no oxygen limiting conditions for the next measurements after 33h). Moreover, the last image shows a re-aeration of the aggregate from the left side. If we additionally look at the radiographs we see that the aggregate has a connection to the air-filled pore space which is assumed to provide the oxygen recharge. Aggregate 2 (Fig. 3, lower row) has a good connection to the water-filled pore space as lower boundary with  $\theta_v > 0.25 \text{ cm}^3/\text{cm}^3$  and a weak contact to the air-filled pore space as upper boundary with  $\theta_v$  from 0.15 – 0.20  $\text{cm}^3/\text{cm}^3$ . Oxygen depletion appears 21h after start of the experiment. Chemical induced oxygen consumption induced depletion zones with minimum oxygen concentration of 0.48 mg/l after 33 h. The depletion zone increases within the first 33h of observation, then decreases and completely disappears by the last measurement after 44h.

Pyrogallol is known to quickly react with  $\text{O}_2$  in alkaline solution. The use of pyrogallol as an oxygen-sensitive tracer dye was found to offer an advantage in that the reduced form can be handled under atmospheric conditions at neutral pH without precaution against oxidation. Moreover, as shown by Oswald et al. (2008) pyrogallol and its oxidations products showed nearly conservative transport behavior in aqueous solution. The presence and distribution of water in the pore space is a critical factor for flow and transport of gases through unsaturated porous media. Moreover, several studies have shown that particle size distribution, air-filled pore size distribution, and microbial activity are key parameters in controlling gaseous transport (Sharma et al. 2009). We showed (Fig. 4.4) that chemical

induced oxygen depletion in structured soils decreased the oxygen concentration down to 0.48 mg/l. The images also showed that gas phase re-supply of oxygen is not limited and the anoxic zones became re-aerated after several hours. Studies suggest that dissolved oxygen levels down to 0.2 mg/l can support biodegradation if oxygen recharge is not limited (Neale et al. 2000).

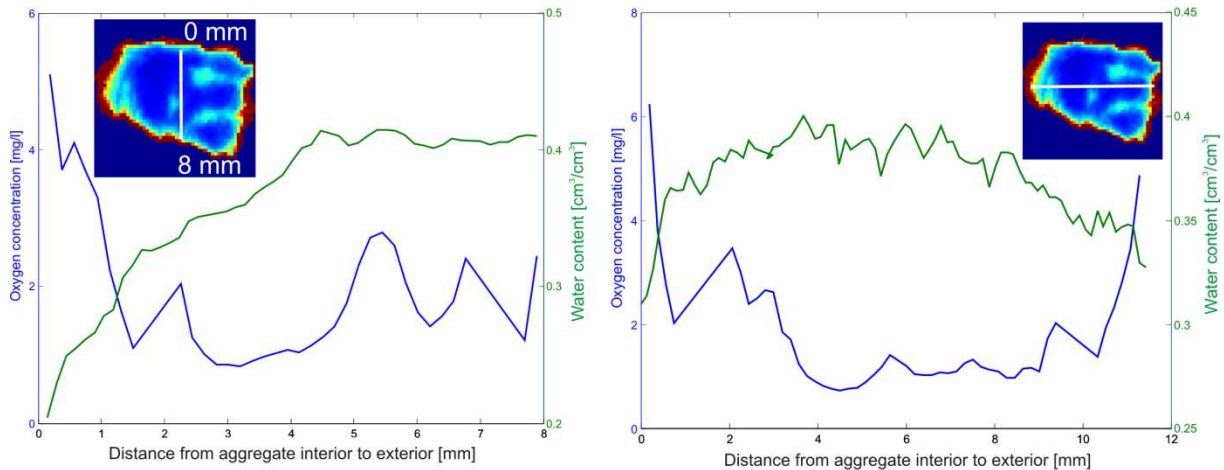


**Fig. 4.5:** Oxygen and water content gradient from aggregate A1 interior to exterior plotted along a vertical (left) and a horizontal (right) profile (position shown in the small image).

A closer look inside the aggregates regarding the gradients of water content and oxygen is provided by Figure 4.5. Within the aggregate, oxygen and water content changed spatially with increasing distance from aggregate exterior and with dependencies from each other. The water content increases with increasing distance to aggregate exterior. The upper boundary of the aggregate is connected to the matrix with water content of  $0.1 \text{ cm}^3/\text{cm}^3$  whereas the lower boundary shows water content around  $0.35 \text{ cm}^3/\text{cm}^3$ . The strong dependency of oxygen transport from water content is visualized here. Oxygen diffusion coefficients are reduced by factor 1000 when going from gas-phase to water-phase. With increasing water content we detect at the same time a decrease in oxygen concentration with increasing distance from upper boundary. Neutron radiography has been proved to be very sensitive to small changes in water content (comparison infiltration experiments from (Oswald et al. 2008b)). The direct measurement of oxygen concentration (Fig. 4.5) within constructed aggregates was shown. The results are in comparison with Sexstone et al. (1985) who measured and modeled oxygen concentrations in water-saturated aggregates. They showed that large aggregate (radius  $\geq 10$  mm) often had anaerobic centre whereas small ( $\leq 6$  mm) aggregates were generally oxic. The oxygen depletion measured inside the aggregate was mainly caused by the water content.

However, Parkin (1987) showed that with sufficient oxygen consumption rates, anaerobiosis can develop even if only a very thin water film (160  $\mu\text{m}$ ) is impeding oxygen diffusion.

Figure 4.6 visualized the effect of pore size distribution on gas transport. It is shown that the formation of oxygen deficits inside clay layers and the re-aeration is different with varying background pore size distribution. As shown in Table 1, air-filled porosity, volumetric water content and porosity are quite similar (V2 vs. V4). The clay layer on the left time series was built within a porous media made of quartz sand with a grain size distribution of 1 – 2 mm whereas the right time series was built within a quartz sand of 0.2 – 1 mm. For the coarser sand re-aeration shows up earlier compared to the finer sand. At the same water content coarser pores are easily drained and built a connection to the air-filled pore space which enhances oxygen transport into the layer structure. The results are consistent with literature. For example, Hammamoto et al. (2009) observed higher gas diffusivity for the coarser sands than for the fine sands, indicating that enhanced gas diffusion and advection occurred through the continuous large-pore networks for sands with high  $D_{50}$ .

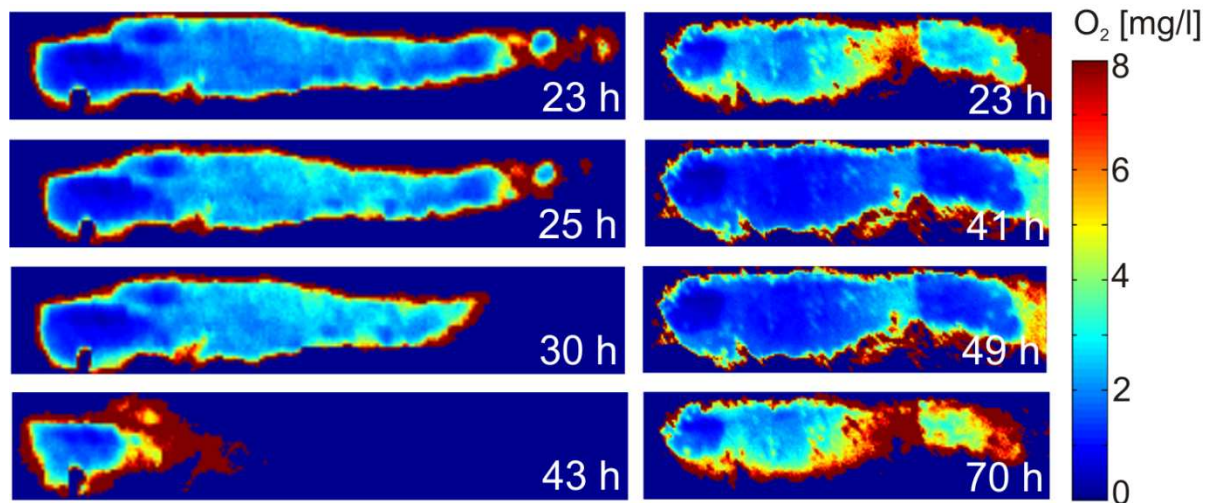


**Fig. 4.6:** Time series of oxygen concentration changes induced by pyrogallol solution in clay layer surrounded by quartz sand of 1 – 2 mm (V2, left block) and 0.2 – 1 mm (V4, right block)

To evaluate the effects of initial oxygen concentration (V3), varying background pore size distribution (V1) and varying water content (V4) we calculated oxygen consumption rates. The oxygen consumption rates (OCRs) were calculated by fitting the changes in  $\text{O}_2$  concentration over time (Fig. 4.7) according to Precht et al. (2004). We chose a pixel (which represents an array of 3 x 3 pixels) located inside the clay layer. The corresponding OCR, equivalent to the negative value of the slope of the oxygen decrease, was  $-9.48 \cdot 10^{-4} \text{ mg L}^{-1}$

$\text{min}^{-1}$  ( $R^2 = 0.99469$ ) for fine background pore size distribution,  $-1.49 \cdot 10^{-3} \text{ mg L}^{-1} \text{ min}^{-1}$  ( $R^2 = 0.95776$ ) for reduced initial oxygen concentration and  $-5.44 \cdot 10^{-4} \text{ mg L}^{-1} \text{ min}^{-1}$  ( $R^2 = 0.97977$ ) for reduced water content, respectively. The situations are quite similar for varying water content (V4) and varying background matrix (V1). The oxygen consumption rate increases slightly with nitrogen flushed buffer solution (V3) indicating a dependency of pyrogallol reaction from initial oxygen value. Within the first 24 h of experimental duration oxygen concentrations changed linearly with time, indicating that the effect of diffusion was negligible and convection the main contributor (Fig. 4.7, left). This pattern changes with increasing experimental duration. The decrease of oxygen slows down during the interval between 43h – 65h which is assumed to be forced by oxygen diffusion.

Oxygen movement in soil occur by convective transport in the water and soil air, diffusion in water and soil air, diffusion into water-saturated soil aggregates, and consumption in free and fixed water (Refsgaard et al. 1991). Figure 6 shows in more detail that in the present study convection and diffusion play a major role depending on the observation time. Within the first 24 h diffusion seems to be neglected. Water infiltrated at the bottom equilibrates and the movement is based on convective forces.

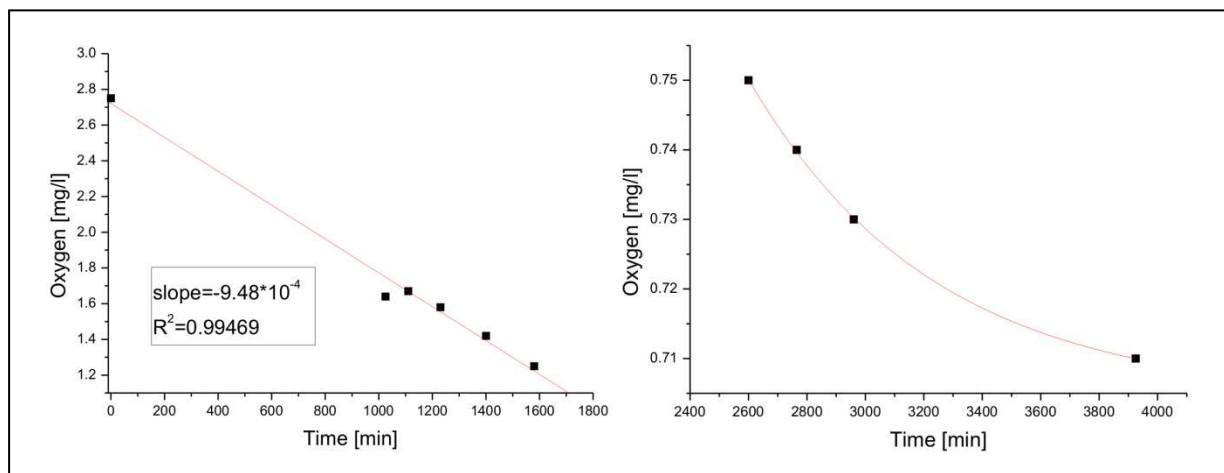


**Fig. 4.7:** Assessment of the OCR in the layer of V4

#### 4.4. Conclusion

There at least two types of situations where oxygen in soil can become depleted by consumption reactions. One is the case of areas or structures of higher suction, e.g. finer grained aggregates. Then water content in these areas will be higher than in the background.

Thus, from metabolic activity (essentially transferring  $O_2$  into  $CO_2$ ) oxygen concentrations will decline and oxygen transition zones will result, provided that gas phase re-supply of oxygen is limited due to the low gas saturation. The shape and gradient of these transition zones will reflect the overall oxygen consumption rate as well as the diffusive water phase transfer of oxygen. At the same time they will in turn limit oxygen consuming processes in the aggregates and indirectly stimulate anoxic processes. The resulting differences in oxygen availability and redox conditions will create different conditions for degradation of organic substances. The other situation is the one of generally high water contents, e.g. by high groundwater table, strong rain events or snow melt, heavy irrigation or even permanently high water stagnation. Here, oxygen consuming processes will deplete the oxygen reservoir after reaching high water saturation in patches depending on the biogeochemical properties of the soil. One example here is the respiration by plant roots set by the structure of the root system. On the opposite, roots of wetland plants could even locally introduce oxygen (to be rapidly consumed by respiration processes in the rhizosphere). With our coupled non-invasive imaging set up we are able to resolve interfaces between aerobic and oxygen-deficit regions and we are able to determine oxygen levels in areas of oxygen depletion. Moreover, the underlying water content, as one of the key drivers for the appearance of the oxygen patterns can be measured in high spatial and temporal resolution.

## References

- Abrash H I, Shih D, Elias W and Malekmehr F 1989 A Kinetic-Study of the Air Oxidation of Pyrogallol and Purpurogallin. *Int J Chem Kinet* 21, 465-476.
- Baleizao C, Nagl S, Schaferling M, Berberan-Santos M N and Wolfbeis O S 2008 Dual fluorescence sensor for trace oxygen and temperature with unmatched range and sensitivity. *Anal Chem* 80, 6449-6457.
- Borisov S M, Lehner P and Klimant I 2011a Novel optical trace oxygen sensors based on platinum(II) and palladium(II) complexes with 5,10,15,20-meso-tetrakis-(2,3,4,5,6-pentafluorophenyl)-porphyrin covalently immobilized on silica-gel particles. *Anal Chim Acta* 690, 108-115.
- Borisov S M, Seifner R and Klimant I 2011b A novel planar optical sensor for simultaneous monitoring of oxygen, carbon dioxide, pH and temperature. *Anal Bioanal Chem* 400, 2463-2474.
- Borisov S M, Vasylevska A S, Krause C and Wolfbeis O S 2006 Composite luminescent material for dual sensing of oxygen and temperature. *Advanced Functional Materials* 16, 1536-1542.
- Carminati A and Fluhler H 2009 Water Infiltration and Redistribution in Soil Aggregate Packings. *Vadose Zone J* 8, 150-157.
- Carminati A, Kaestner A, Lehmann P and Fluhler H 2008 Unsaturated water flow across soil aggregate contacts. *Advances in Water Resources* 31, 1221-1232.
- Carminati A, Moradi A B, Vetterlein D, Vontobel P, Lehmann E, Weller U, Vogel H J and Oswald S E 2010 Dynamics of soil water content in the rhizosphere. *Plant Soil* 332, 163-176.
- Carraway E R, Demas J N and Degraff B A 1991a Luminescence Quenching Mechanism for Microheterogeneous Systems. *Anal Chem* 63, 332-336.
- Carraway E R, Demas J N, DeGraff B A and Bundt M 1991b Photophysics and Photochemistry of Oxygen Sensors Based on Luminescent Transition-Metal-Complexes. *Anal Chem* 63, 337-342.
- Deinert M R, Parlange J Y, Steenhuis T, Throop J, Unlu K and Cady K B 2004 Measurement of fluid contents and wetting front profiles by real-time neutron radiography. *J Hydrol* 290, 192-201.
- Dexter A R 1997 Physical properties of tilled soils. *Soil Till Res* 43, 41-63.
- Doona C J and Kustin K 1993 Kinetics and Mechanism of Pyrogallol Autoxidation - Calibration of the Dynamic-Response of an Oxygen-Electrode. *Int J Chem Kinet* 25, 239-247.
- Fuller Z J, Bare W D, Kneas K A, Xu W Y, Demas J N and DeGraff B A 2003 Photostability of luminescent ruthenium(II) complexes in polymers and in solution. *Anal Chem* 75, 2670-2677.
- Glud R N, Santegoeds C M, De Beer D, Kohls O and Ramsing N B 1998 Oxygen dynamics at the base of a biofilm studied with planar optodes. *Aquatic Microbial Ecology* 14, 223-233.



- Hamamoto S, Moldrup P, Kawamoto K and Komatsu T 2009 Effect of Particle Size and Soil Compaction on Gas Transport Parameters in Variably Saturated, Sandy Soils. *Vadose Zone J* 8, 986-995.
- Hassanein R K 2006 CORRECTION METHODS FOR THE QUANTITATIVE EVALUATION OF THERMAL NEUTRON TOMOGRAPHY. Diss. ETH No. 16809.
- Hinsinger P, Bengough A G, Vetterlein D and Young I M 2009 Rhizosphere: biophysics, biogeochemistry and ecological relevance. *Plant Soil* 321, 117-152.
- Horn R and Peth S 2009 Soil structure formation and management effects on gas emission. *Biologia* 64, 449-453.
- Jensen S I, Kuhl M, Glud R N, Jorgensen L B and Prieme A 2005 Oxidic microzones and radial oxygen loss from roots of *Zostera marina*. *Mar Ecol-Prog Ser* 293, 49-58.
- Klimant I, Meyer V and Kuhl M 1995 Fiberoptic Oxygen Microsensors, a New Tool in Aquatic Biology. *Limnol Oceanogr* 40, 1159-1165.
- Kristensen A H, Thorbjorn A, Jensen M P, Pedersen M and Moldrup P 2010 Gas-phase diffusivity and tortuosity of structured soils. *J Contam Hydrol* 115, 26-33.
- Lazik D, Krauss G, Geistlinger H and Vogel H-J 2008 Multi-scale optical analyses of dynamic gas saturation during air sparging into glass beads. *Transport in Porous Media* in press.
- Lipiec J, Walczak R, Witkowska-Walczak B, Nosalewicz A, Slowinska-Jurkiewicz A and Slawinski C 2007 The effect of aggregate size on water retention and pore structure of two silt loam soils of different genesis. *Soil Till Res* 97, 239-246.
- Mayr T, Borisov S M, Abel T, Enko B, Waich K, Mistlberger G and Klimant I 2009 Light Harvesting as a Simple and Versatile Way to Enhance Brightness of Luminescent Sensors. *Anal Chem* 81, 6541-6545.
- Menon M, Robinson B, Oswald S E, Kaestner A, Abbaspour K C, Lehmann E and Schulin R 2007 Visualization of root growth in heterogeneously contaminated soil using neutron radiography. *Eur J Soil Sci* 58, 802-810.
- Mills A and Lepre A 1997 Controlling the response characteristics of luminescent porphyrin plastic film sensors for oxygen. *Anal Chem* 69, 4653-4659.
- Neale C N, Hughes J B and Ward C H 2000 Impacts of unsaturated zone properties on oxygen transport and aquifer reaeration. *Ground Water* 38, 784-794.
- Niemet M R and Selker J S 2001 A new method for quantification of liquid saturation in 2D translucent porous media systems using light transmission. *Advances in Water Resources* 24, 651-666.
- Oswald S E, Griepentrog M, Schirmer M and Balcke G U 2008a Interplay between oxygen demand reactions and kinetic gas-water transfer in porous media. *Water Research* 42, 3579-3590.
- Oswald S E, Menon M, Carminati A, Vontobel P, Lehmann E and Schulin R 2008b Quantitative imaging of infiltration, root growth, and root water uptake via neutron radiography. *Vadose Zone J* 7, 1035-1047.
- Parkin T B 1987 Soil Microsites as a Source of Denitrification Variability. *Soil Sci Soc Am J* 51, 1194-1199.

- Pierret A, Kirby M and Moran C 2003 Simultaneous X-ray imaging of plant root growth and water uptake in thin-slab systems. *Plant Soil* 255, 361-373.
- Precht E, Franke U, Polerecky L and Huettel M 2004 Oxygen dynamics in permeable sediments with wave-driven pore water exchange. *Limnol Oceanogr* 49, 693-705.
- Refsgaard J C, Christensen T H and Ammentorp H C 1991 A Model for Oxygen-Transport and Consumption in the Unsaturated Zone. *J Hydrol* 129, 349-369.
- Rennert T, Totsche K U, Heister K, Kersten M and Thieme J 2012 Advanced spectroscopic, microscopic, and tomographic characterization techniques to study biogeochemical interfaces in soil. *J Soil Sediment* 12, 3-23.
- Rudolph N, Esser H G, Carminati A, Moradi A B, Hilger A, Kardjilov N, Nagl S and Oswald S E 2012 Dynamic oxygen mapping in the root zone by fluorescence dye imaging combined with neutron radiography. *J Soil Sediment* 12, 63-74.
- Schröder C R, Polerecky L and Klimant I 2007 Time-resolved pH/pO<sub>2</sub> mapping with luminescent hybrid sensors. *Anal Chem* 79, 60-70.
- Sharma P, Poulsen T G and Kalluri P N V 2009 Gaseous Oxygen Uptake in Porous Media at Different Moisture Contents and Airflow Velocities. *Journal of the Air & Waste Management Association* 59, 676-682.
- Stich M I J, Fischer L H and Wolfbeis O S 2010 Multiple fluorescent chemical sensing and imaging. *Chem Soc Rev* 39, 3102-3114.
- Totsche K U, Eusterhues K and Rennert T 2012 Spectro-microscopic characterization of biogeochemical interfaces in soil. *J Soil Sediment* 12, 1-2.
- Totsche K U, Rennert T, Gerzabek M H, Kogel-Knabner I, Smalla K, Spiteller M and Vogel H J 2010 Biogeochemical interfaces in soil: The interdisciplinary challenge for soil science. *J Plant Nutr Soil Sc* 173, 88-99.
- Votrubova J, Cihlarova M, Amin M H G and Hall L D 2003 Recurrent ponded infiltration into structured soil: A magnetic resonance imaging study. *Water Resources Research* 39.
- Whalley W R, Riseley B, Leeds-Harrison P B, Bird N R A, Leech P K and Adderley W P 2005 Structural differences between bulk and rhizosphere soil. *Eur J Soil Sci* 56, 353-360.
- Young I M and Crawford J W 2004 Interactions and self-organization in the soil-microbe complex. *Science* 304, 1634-1637.
- Young I M, Crawford J W and Rappoldt C 2001 New methods and models for characterising structural heterogeneity of soil. *Soil Till Res* 61, 33-45.

## Chapter 5

# Coupled denitrification and anaerobic biodegradation monitored using nitrate-sensitive fluorescence imaging<sup>4</sup>

*Microbial biodegradation of contaminants in natural and engineered environments is governed by gradients of nutrient and electron acceptor availability which evolve over time in response to water flow, contaminant migration and spatial variations in microbial activity. In this study we combined analytical, modelling and imaging techniques to calibrate a rhodamine-based, nitrate-sensitive fluorescence tracer capable of noninvasive monitoring of the evolution of biodegradation in experimental plumes under anaerobic, nitrate-reducing conditions. A microbial consortium cultured from a contaminated groundwater borehole was inoculated with acetate (200-300 mg L<sup>-1</sup>) at a rate of 8.6  $\mu\text{L min}^{-1}$  in a thin-bed sand pack under steady, saturated, anaerobic flow at 0.13 mL min<sup>-1</sup> for 5 days. Nitrate and acetate in samples obtained along the length of the plume and at the outlet, combined with biomass assays at the end of the experiment, indicated that anaerobic biodegradation of acetate with nitrate as a terminal electron acceptor had occurred. These data were used to constrain a 2D reactive transport model for the biodegrading plume which showed close agreement with measurements of nitrate concentrations within the sand in calibrated fluorescence images. The nitrate-sensitive tracer is a potential tool for noninvasive monitoring of spatial gradients in nitrate concentration during anaerobic biodegradation and/or denitrification in porous media under a range of boundary conditions.*

**Keywords:** bench scale, intensity, non-invasive, optical sensor, plume, sand

---

<sup>4</sup> An article with equivalent content is submitted to Water Research as:

H.C. Rees, J.W. Bridge, N. Rudolph, S.E. Oswald and S.A. Banwart (2013): Coupled denitrification and anaerobic biodegradation monitored using nitrate-sensitive fluorescence imaging

My contribution was the numerical modeling for the existing imaging experiment and contributes about 15% of the work.

## 5.1 Introduction

Nitrate ( $\text{NO}_3^-$ ) is present in almost every natural and engineered water environment. As an essential plant macronutrient, nitrates are a major export from intensive agriculture and also form a significant component of domestic and industrial wastewaters. Resulting excess concentrations of  $\text{NO}_3^-$  in groundwater and surface waters present a substantial ecological hazard through eutrophication and direct toxicity (Wakida and Lerner, 2005; Rivett et al., 2008; Mastrocicco et al., 2011). Minimisation of nitrate loads to receiving waters is a critical objective for environmental regulation worldwide where industrial agriculture and large-scale wastewater treatment exist (UNEP, 2012).

Removal of  $\text{NO}_3^-$  from soil by denitrifying microbes is a fundamental part of the nitrogen cycle. Enhancement of microbial denitrification for water resource protection is an important research theme in ecological engineering (Schipper et al., 2010; Warneke et al., 2011; Tanner et al., 2012) and is a critical process in wastewater treatment (Winkler et al., 2012). Heterotrophic denitrification, in which  $\text{NO}_3^-$  acts as a terminal electron acceptor enabling the microbial utilisation of carbon sources, also plays an important role in the biodegradation of organic pollutants (Yoshida, 2011) and in the evolution of the complex subsurface biogeochemical environments encountered in the management of industrial and nuclear contaminated sites (Thorpe et al., 2012).

Studies of contaminant plumes in field and laboratory-scale experiments have highlighted the sensitivity of both biodegradation rates and microbial community structure to spatial gradients in the availability of carbon sources and electron acceptors including nitrate (Watson et al., 2005; Rees et al., 2007). These gradients in turn are determined in part by rates of consumption and utilization by the microbial consortia, such that the spatial distribution of microbial activity is governed by dynamic equilibria which evolve and respond to changing boundary conditions (Oates et al., 2005). These complex system characteristics are crucial to the optimization of engineered denitrification and anaerobic biodegradation systems (Herbert, 2011), the resilience of such systems to fluctuations in environmental conditions or input streams, and the long-term accuracy of models predicting the microbial consortia implicit in the success of contaminant remediation by natural attenuation (Thorpe et al., 2012).

A key step in understanding the performance and dynamics of these systems is the ability to monitor the gradients in conditions at fine spatial resolution and without disturbance, i.e. non-destructively and, ideally, noninvasively. The imperative for real-time, high-resolution data to improve process modelling, optimize efficiency and predict

performance under changing conditions is well recognized in agriculture and contaminant hydrology (Sinfield et al., 2010; Eschenbach and Well, 2011) and by the wastewater treatment community. Several spectrophotometric, electrochemical and biological sensor technologies have been demonstrated for the *in situ* measurement of nitrate (Sinfield et al., 2010). Here, we apply two-dimensional imaging of a nitrate-sensitive rhodamine-based fluorophore (Mohr and Wolfbeis, 1996a) to quantify  $\text{NO}_3^-$  concentrations during anaerobic biodegradation of an acetate plume in a laboratory-scale reactor containing anaerobic, saturated quartz sand. We show that the fluorophore, fixed in a polymer coating on the sand, enables monitoring of the spatial dimensions of the degrading plume. Measurements of spatial gradients in nitrate concentration were obtained from image data calibrated against independent samples, which compared reasonably well with a two-dimensional reactive transport model for anaerobic biodegradation. We discuss a range of potential environmental and engineering applications for the nitrate tracer in laboratory studies and *in situ* sensing.

## 5.2 Experimental section

The general apparatus and procedures for fluorescence imaging of solute and particle reactive transport in thin bed sand packs have been described elsewhere (Huang et al., 2003; Rees et al., 2007; Bridge et al., 2009). Modifications and additional materials specific to this study are described here. All chemicals and reagents were obtained from Sigma-Aldrich UK unless otherwise stated.

### 5.2.1 Preparation of the nitrate-sensitive membrane

The basic preparation has been described previously (Mohr and Wolfbeis, 1996a, 1996b) and modified for use here. The following chemicals were mixed in a glass flask: 45 mg polyvinyl chloride (PVC); 0.21 mL bis-(2-ethylhexyl)sebacate (DOS); 0.909 mg tridodecylmethylammonium chloride (TDMACl); 1 mg Rhodamine B octadecylester perchlorate (RBOE); and 27.3 mL tetrahydrofuran (THF). This mixture was added to 750 g sterile high purity quartz sand (212-300  $\mu\text{m}$  diameter, 99.9%  $\text{SiO}_2$ ) and mixed until the sand was evenly coated. Coated sand was stored in the dark at 4 °C and used within 3 months of preparation. The membrane coating emits visible-light fluorescence under blacklight ultra-violet illumination (peak output wavelength 350-380 nm). The fluorescence intensity of the membrane in a phosphate buffer is directly proportional to nitrate concentration (Mohr and Wolfbeis, 1996a, 1996b). Before use the coated sand was conditioned in 0.1 M sodium nitrate

for 45 minutes then washed several times with plain buffer (20 mM sodium phosphate buffer with pH 7.13).

### **5.2.2 Growth medium and inoculums**

Preparation of biofilm on quartz sand is described elsewhere (Rees et al., 2007). Cultured cells for biofilm production were grown in an anaerobic chamber in mineral media (10 mM NaH<sub>2</sub>PO<sub>4</sub> and 10 mM Na<sub>2</sub>HPO<sub>4</sub>; NaCl, 0.017 g L<sup>-1</sup>; NaHCO<sub>3</sub>, 0.014 g L<sup>-1</sup>; MgSO<sub>4</sub>, 0.013 g L<sup>-1</sup>; NaNO<sub>3</sub> 0.069 g L<sup>-1</sup>, pH 7.0) with the addition of acetate (200-300 mg L<sup>-1</sup>) at room temperature for approximately 48 hours with stirring. Biofilm coated sand was produced following the method described by (Rees et al., 2007).

### **5.2.3 Set up and operation of the flow cell**

The basic experiment has been described previously (Huang et al., 2003) along with modifications (Rees et al., 2007) which are further developed here to describe the use of the RBOE-coated sand. Experiments were carried out in a Perspex flow cell (see Figure 1) which was wet-packed with a premixed (in a sterile glass beaker) 50:50 slurry of RBOE-coated sand, and biofilm-coated sand in mineral medium. A constant flow rate of 0.13 mL min<sup>-1</sup> was applied using a peristaltic pump (WM502U, Watson-Marlow) to create a uniform flow field within the sand pack. A syringe pump (KD220, KS Scientific) was used to inject the mineral media plus carbon source (200-300 mg L<sup>-1</sup> acetate) into this flow field at a constant relatively small flow rate of 8.6 µL min<sup>-1</sup>.

Two sets of experiments were performed under anaerobic conditions within an anaerobic chamber. Fluorescence images were obtained at the end of each experiment run (after 5 days). In the first set of experiments triplicate flow cells were set up and run as described. A fourth sterile flow cell acted as a control. The second set of experiments in triplicate flow cells with a fourth sterile flow cell as a control was set up as described except that the RBOE-coated sand was excluded and replaced with uncoated, sterile quartz sand which was mixed 50:50 with the biofilm coated quartz sand in order to assess the effects, if any, of the fluorescence membrane on microbial activity.

### **5.2.4 Chemical analyses**

Samples were taken from within the sand pack via septum ports (Figure 5.1) as described previously (Rees et al., 2007) and analysed for nitrate using ion chromatography

(DX-120, Dionex). Acetate and pH levels in the inflow, outflow, and injection solutions were measured using ion chromatography and a pH meter (HI9321, Hannah).

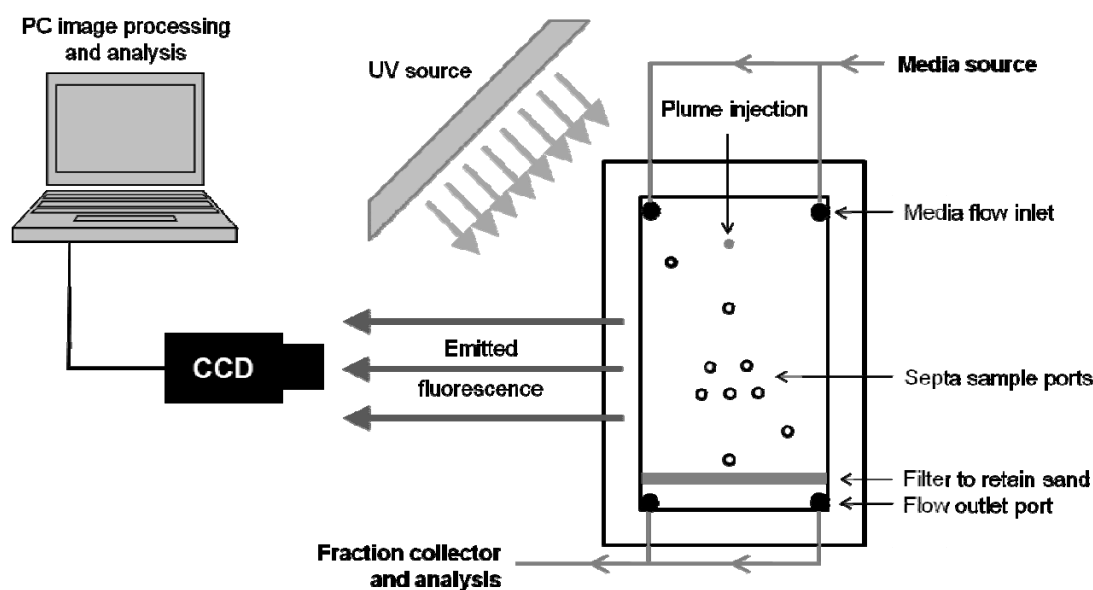


**Fig. 5.1:** Experimental setup showing 20 x 10 x 0.5 cm flow cell, injection and sampling ports, UV illumination and detection of visible-light fluorescence from RBOE membrane

### 5.2.5 Fluorescence imaging of nitrate

Images of the plume after 5 days were taken using a monochrome CCD camera (KP-D581, Hitachi) fitted with a long pass lens filter which excluded the UV excitation light and transmitted only the visible-light emission signal. Image data were stored on PC using an image grabber and processed and analysed using open-source ImageJ software.

### 5.2.6 Nitrate tracer calibration

Nitrate concentrations obtained after 5 days from the septum ports located along the centre-line of the vertical flow field in each triplicate flow cell (Figure 5.1) were plotted against the intensity of RBOE fluorescence averaged over a 1 cm<sup>2</sup> region of interested centered on the location of each port. Least-squares regression was used to obtain a calibration relationship giving nitrate concentration as an empirical function of fluorescence intensity within the range of intensities recorded in the experiments.

### 5.2.7 Reactive transport modelling

Numerical modelling was carried out using Visual Modflow 4.3. A sub-module RT3D2.5 was used to simulate the reactive transport and to obtain the nitrate distribution as a function of growth and decay of the microbial biomass using the dual-Monod model (McGee et al., 1972) to describe anaerobic microbiological degradation. The reaction rate terms in the advection-dispersion equation for transport are:

$$\frac{dC}{dt} = -X \times \frac{\mu_m}{Y_{X/C}} \times \frac{C}{K_C + C} \times \frac{N}{K_N + N} = -X \times k_{\max} \times \frac{C}{K_C + C} \times \frac{N}{K_N + N} \quad [1]$$

$$\frac{dN}{dt} = -X \times F \times \frac{\mu_m}{Y_{X/C}} \times \frac{C}{K_C + C} \times \frac{N}{K_N + N} = -X \times F \times k_{\max} \times \frac{C}{K_C + C} \times \frac{N}{K_N + N} \quad [2]$$

$$\begin{aligned} \frac{dX}{dt} &= X \times \mu_m \times \frac{C}{K_C + C} \times \frac{N}{K_N + N} - X \times d \\ &= X \times Y_{X/C} \times k_{\max} \times \frac{C}{K_C + C} \times \frac{N}{K_N + N} - X \times d \end{aligned} \quad [3]$$

where  $C$  is the carbon source (acetate) concentration ( $\text{mg L}^{-1}$ ),  $N$  is nitrate concentration ( $\text{mg L}^{-1}$ ),  $X$  is the initial biomass ( $\text{mg dry cell L}^{-1}$ ),  $\mu_m$  is the maximum specific growth rate ( $\text{s}^{-1}$ ),  $Y_{X/C}$  is the growth yield for the carbon source ( $\text{mg dry cell weight/ mg acetate consumed}$ ),  $F$  is the stoichiometric ratio of nitrate to acetate in the degradation reaction ( $\text{mg nitrate consumed/ mg acetate consumed}$ ),  $K_C$  is the half-saturation constant for the carbon source ( $\text{mg acetate L}^{-1}$ ),  $K_N$  is the half-saturation constant for nitrate ( $\text{mg acetate L}^{-1}$ ), and  $d$  is the death rate for the microbial population  $X$  ( $\text{s}^{-1}$ ). Transport parameter values used in the model were based on those used previously for similar laboratory flow experiments (Rees et al., 2007) and those determined for anaerobic degradation using nitrate as a terminal electron acceptor (Watson et al., 2005) and are shown in Table 5.1. The numerical solution method was based on a hybrid method of characteristics scheme with implicit solver. It should be noted that RT3D does not require the maximum specific growth rate,  $\mu_m$ , as the input value but uses a maximum substrate utilization rate,  $k_{\max}$  ( $\text{s}^{-1}$ ), as given at the right side of Equations 1-3. We used  $k_{\max}$  as a regression parameter to fit the model to the nitrate and acetate data from the experiments.



**Table 5.1:** Summary of transport and kinetic biodegradation parameters.

Parameter	Value
Inner model size (mm)	100 × 200 × 5
Porosity (-)	0.45
Transverse dispersivity (mm)	0.04
Longitudinal dispersivity (mm) <sup>a</sup>	0.40
Pore water velocity (mm s <sup>-1</sup> )	1.027 × 10 <sup>-2</sup>
Bulk density of porous medium (mg mm <sup>-3</sup> )	1.46
Equivalent inlet diameter (mm)	14
Initial nitrate concentration $N$ (mg L <sup>-1</sup> )	33.54
Inlet acetate concentration $C$ (mg L <sup>-1</sup> )	320.58
Substrate utilisation rate $k_{max}$ (s <sup>-1</sup> )	Fitted
Ratio $F$ of nitrate / acetate (mg mg <sup>-1</sup> )	1.34
Growth yield $Y_{x/c}$ (mg dry cell weight / mg substrate)	0.4
Half saturation constant acetate $K_C$ (mg L <sup>-1</sup> )	29.5
Half saturation constant for nitrate $K_N$ (mg L <sup>-1</sup> )	0.5
Initial total biomass $X$ (mg dry cell weight L <sup>-1</sup> )	15.3
Microbial death rate $d$ (s <sup>-1</sup> )	1.54 × 10 <sup>-5</sup>

### 5.2.8 Biological analyses

Biological samples were obtained by destructive sampling of the flow cells following the imaging step at the end of the experimental run, followed by sonication of 0.2 g sand samples to remove attached cells. Active cells were elucidated using 5-cyano-2,3-ditolyl tetrazolium chloride (CTC) staining (Rodriguez et al., 1992) and total counts were performed using DAPI (4'6-diamidino-2-phenylindole) (Porter and Feig, 1980). Protein analysis was carried out on both 0.2 g unsonicated sand (to obtain total protein) and on 0.2 g sand that had previously been sonicated to remove cells (to allow calculation of total cell numbers present) using a modified Lowry assay following the manufacturer's method (Sigma-Aldrich, UK). The basic procedure for microbial community analysis by PCR-TGGE has been described previously (Rees et al., 2007) and utilises the 'touchdown' PCR method (Don et al., 1991). PCR products were purified and concentrated using Qiagen quick-spin columns (Qiagen Ltd., Crawley, UK) according to the manufacturer's instructions. The products were then analysed by TGGE on a 12 % acrylamide gel with a temperature gradient of 45-60 °C.

## 5.3 Results and discussion

### 5.3.1 Chemical analyses at sample ports

Chemical analysis of samples taken from the flow cells at the end of the 5-day experimental run were performed on both sets of experiments (with and without RBOE tracer) and showed a decrease in acetate concentration from the inlet to the outlet (Table 5.2). Nitrate concentration decreased with distance along the vertical flow line from inlet to outlet, but remained constant in sample ports to either side of the central flow path (Table 5.2).

**Table 5.2:** Summary of chemical measurements in background inflow, outlet and plume inlet.

RBOE	Sample location <sup>a</sup>	Nitrate (mg L <sup>-1</sup> ± SD)	Acetate (mg L <sup>-1</sup> ± SD)	pH (± SD)
Present	Initial	33.54 ± 1.64	-	7.30 ± 0.00
	Background	33.54 ± 1.64	-	7.43 ± 0.09
	Inlet	24.67 ± 2.07	320.58 ± 19.96	7.39 ± 0.009
	Outflow	9.90 ± 2.04	20.55 ± 14.28	9.46 ± 0.10
Not Present	Initial	29.05 ± 2.28	-	7.30 ± 0.00
	Background	29.05 ± 2.28	-	7.19 ± 0.22
	Inlet	36.04 ± 0.68	366.77 ± 19.24	7.49 ± 0.03
	Outflow	6.26 ± 2.28	10.82 ± 4.10	9.34 ± 0.13

<sup>a</sup> Initial averages were time zero samples (taken from a separate flow cell in each experiment). Background data from ports located away from the vertical flow line between the inlet and outlet (see Figure 5.1). All data are averages across 3 replicate flow cells.

### 5.3.2 Nitrate concentrations in the flow cell

The log mean fluorescence intensity recorded at the location of each septum port was regressed against the nitrate concentration measured at that port to obtain a linear calibration ( $r^2 = 0.91$ ) within the range of the samples (Figure 5.2). This regression was used to calibrate image data yielding two-dimensional data arrays of nitrate concentration which clearly show the location and dimensions of the nitrate-depleted plume (Figure 5.3a). Granularity in the image data arises in part from local variations in optical transmissivity in the sand (Bridge et al., 2006). Edge effects occurred where the intensity of excitation light from the UV lamp was shaded by the frame of the flow cell – these reduced the intensity of resultant RBOE

fluorescence and hence calibrated measurements were restricted to the central 75 x 128 mm region of the flow cell (Figure 5.3).

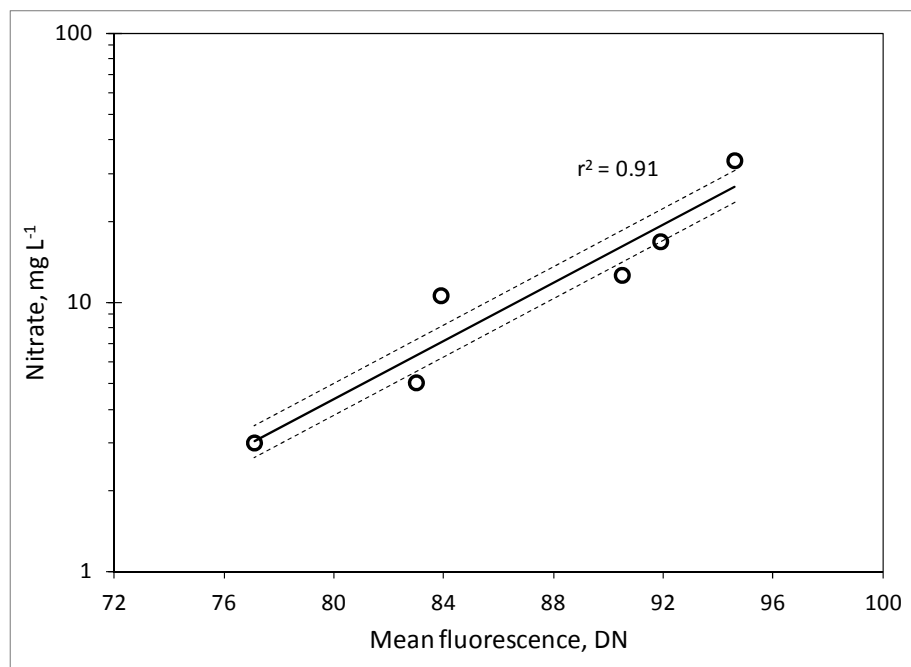


**Fig. 5.2.** Calibration between mean fluorescence measured in image data and nitrate concentration measured in samples obtained at six septum ports. Dashed lines indicate 95% confidence intervals on the regression (solid line).

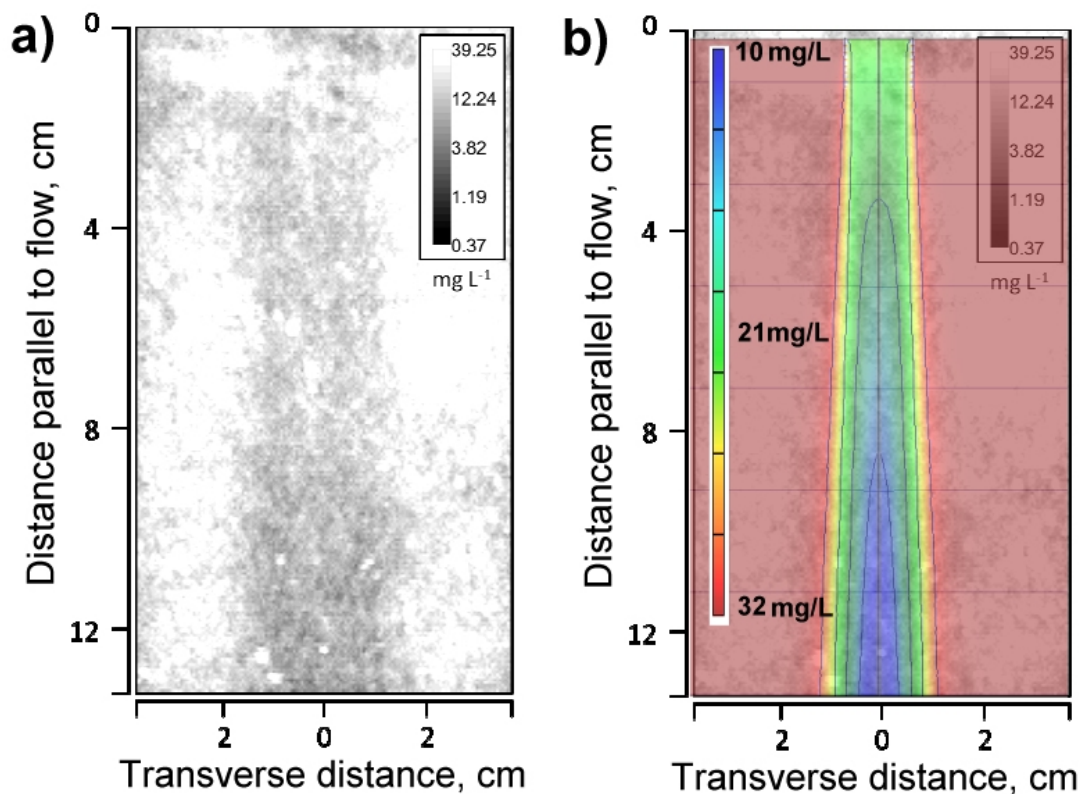


**Fig. 5.3.** a) Calibrated image data showing variations in  $\text{NO}_3^-$  concentration within a flow chamber 5 days after starting injection of the acetate + nitrate plume. b) Image data shown in (a) with model output at  $k_{max}$   $0.000135 \text{ s}^{-1}$  overlaid at the same scale.

### 5.3.3 Numerical simulations

The anaerobic biodegradation was modelled numerically as described, with values of fitting parameter  $k_{max}$  in the range  $1.0 \times 10^{-4} \text{ s}^{-1}$  to  $2.0 \times 10^{-4} \text{ s}^{-1}$ . Figure 5.4 shows selected model output as transverse profiles across the plume at a distance of 90.5 mm from the inlet in comparison with both calibrated image data and sampled nitrate concentrations. Best fit between the model and sampled nitrate concentrations was obtained with  $k_{max} = 1.35 \times 10^{-4} \text{ s}^{-1}$ . In two-dimensions, the calibrated image data and the modelled plume dimensions agreed qualitatively very well (Figure 5.3b) although Figure 4 indicates that the image data tended to underpredict nitrate concentrations as they increased to the background level ( $33.54 \pm 1.64 \text{ mg L}^{-1}$ ). Reference to Figure 5.2 confirms that the calibration function loses resolution as nitrate concentration increases (note the log scale on the y-axis). This would serve to enhance any potential effects of variations in optical transmissivity of the sand (noted previously) or of any leaching or photobleaching of the dye.

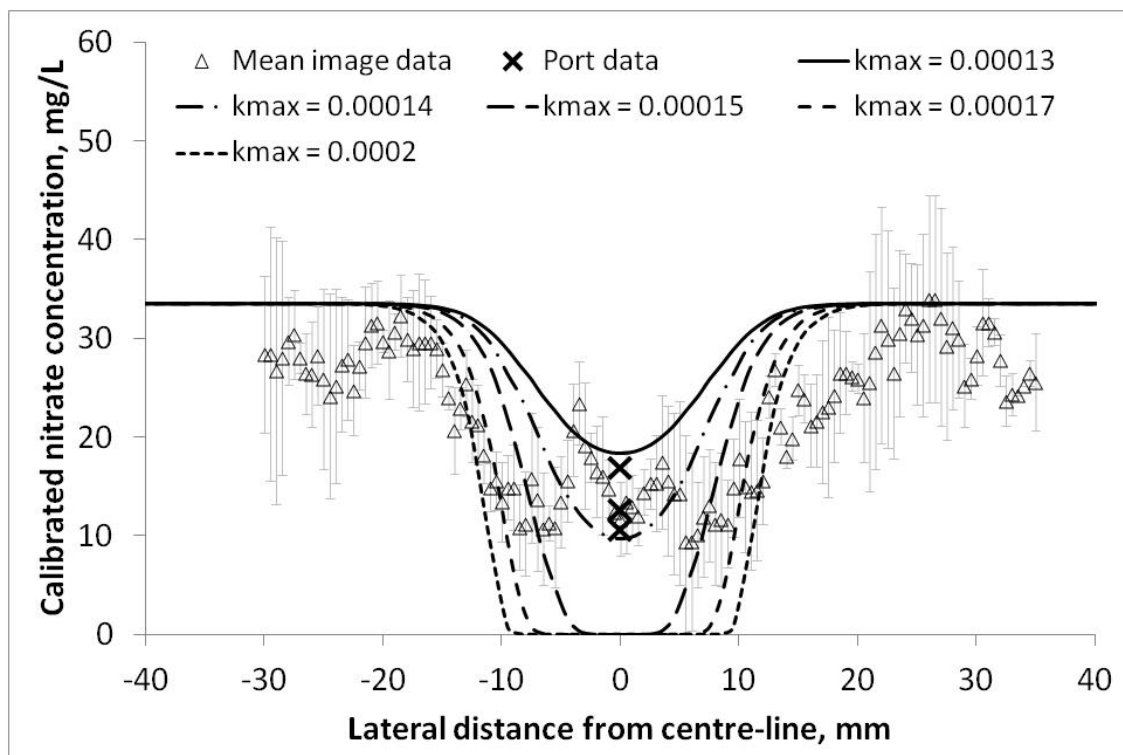


**Fig. 5.4.** Comparison between calibrated image data (triangles) and model output (lines) for a range of values of  $k_{max}$  ( $s^{-1}$ ). Transects are taken at 90.5 mm vertical distance from the inlet. Crosses indicate independently measured sample port nitrate concentrations at 45, 90 and 135 mm from the inlet. Error bars on image data are one standard deviation for image values averaged over three neighbouring pixels.

### 5.3.4 Microbial analysis

As with previous work on aerobic reactors using the same flow cell system but with an oxygen tracer  $Ru(phen)_3Cl_2$  in place of RBOE (Rees et al., 2007), results from biological analysis of sand samples illustrated the variation in total biomass present across the flow cells at time zero (Figure 5.5). Between-replicate variability in protein data meant no statistically-significant interpretation of differences between sample ports was possible. However, total (DAPI-stained) and active (CTC-stained) cell counts showed that active cells typically comprised less than 2 % of the total cell counts (Table 5.3). There were significantly higher levels of cell activity within the source and fringe areas of the acetate plume compared to that of the core and consistently higher, although not statistically separable, active cell counts in the plume fringe compared to the background. There were no significant differences between experiments with and without the RBOE nitrate-sensitive coating, indicating that the fluorescence sensor did not affect microbiological activity in this system.

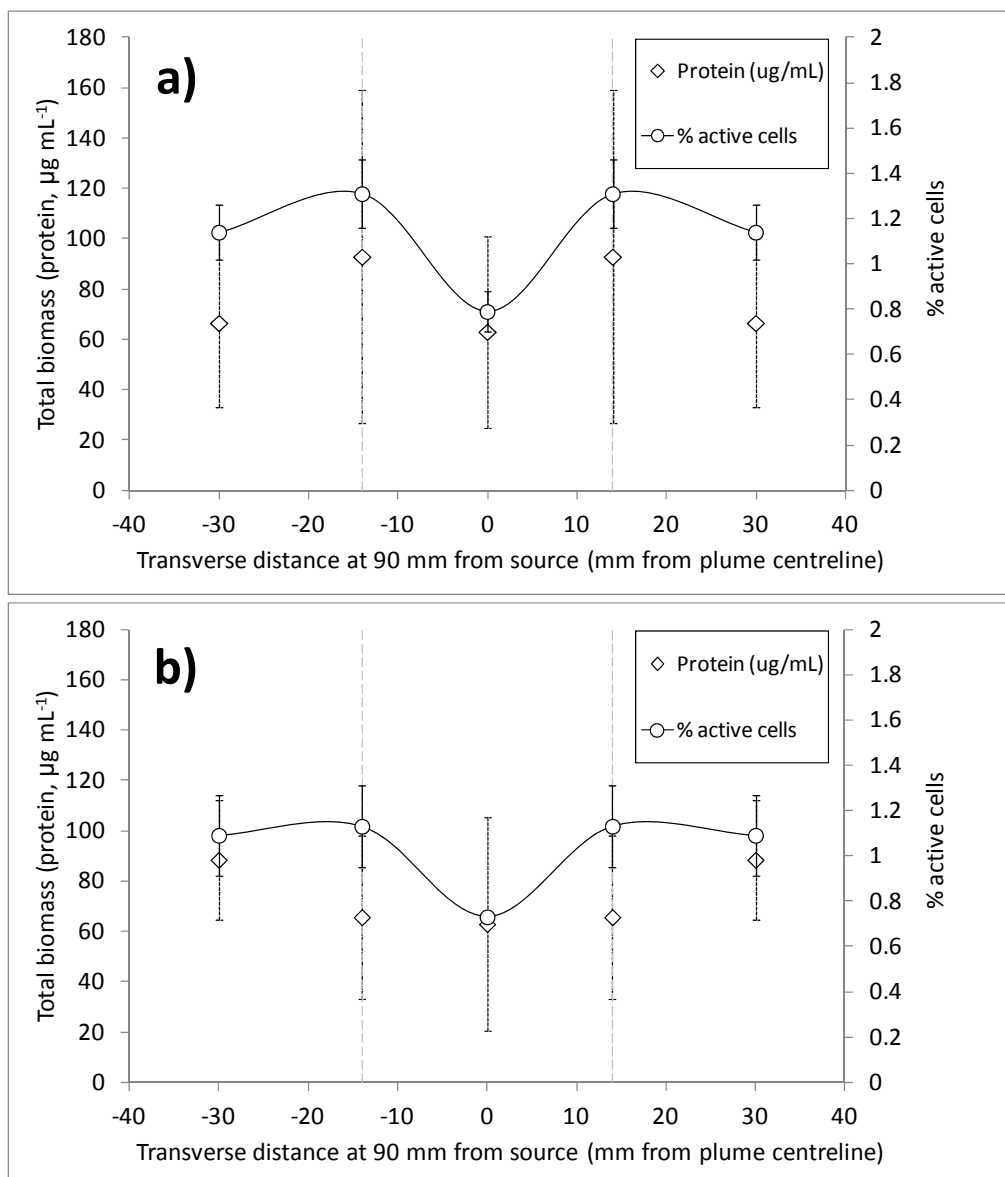


**Fig. 5.5.** Protein ( $\mu\text{g mL}^{-1}$ ) and % active cells measured 5 days after injection commenced in samples from septa ports at 90 mm from the inlet in experiments with a) RBOE sand coating and b) no RBOE sand coating. Error bars are standard deviations among experiment replicates. Dashed vertical lines indicate approximate plume boundaries observed in image data.

### 5.3.5 Microbial community structure

TGGE was used to obtain the microbial community structure generated from 16S rRNA gene amplicons amplified from (i) the subsamples from the flow cells, (ii) the growth culture used as the inoculum, and (iii) the original MW7 borehole water source. The community structure is shown in Figure 5.6. Within the resolution limits of the technique, MW7 water contained four distinct amplicons (Figure 5.6, bands A to D), fewer than those seen when grown aerobically (Rees et al., 2007). Although some variation was observed at

five days, the acetate-grown community was reasonably characteristic of the region of the plume: background (non-plume) regions retained 50 to 100 %; fringe regions 25 to 75 %; core regions 75 to 100 %, and injection regions 50 to 100 % of the original community structure, with all bands being lost at some point and some being more susceptible than others. Band C was lost most frequently.

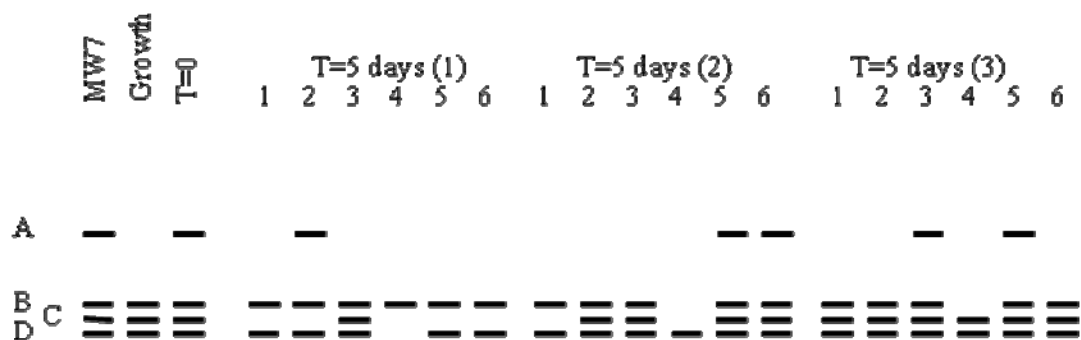


**Fig. 5.6.** Diagrammatic representation of TGGE gels for a 5 day experiment with RBOE. Amplicons present in the borehole water used as the original inocula (lane MW7), the growth culture used to create the biofilm (lane Growth), and samples from a replicate cell at the start of experiments (lane T=0) are shown. For T = 5 days, the amplicons present in flow cells 1 to 3 (cell labels in parentheses) at six sampling points are shown. The samples were taken systematically across a plume transect: samples 1 and 5 are non-plume regions, samples 2 and 4 are plume fringe areas, sample 3 is the plume core, and sample 6 is taken at the carbon source inlet. Gels were run at a gradient of 45-60°C.

### 5.3.6 Extent and character of anaerobic biodegradation

In the short timescale of this study, the results of the TGGE suggest that changes in community structure were limited and that they occurred once the community was established on the quartz matrix rather than during the development of the inocula. Changes in activity in response to gradients in carbon source and nitrate concentration across the plume probably occurred through increased or decreased expression of function within the existing community rather than through dramatic shifts in functional groups, given the already-limited diversity of the groundwater community at the start of the experiment (Rees et al., 2007). The pattern of cell activity observed here was seen previously, though more pronounced, in aerobic experiments (Rees et al., 2007) and is consistent with the conceptual model of plume biodegradation where activity is greatest in the fringes and source area and depleted in the core, due to differential distributions of electron acceptor and carbon source (e.g. Gutierrez-Neri et al., 2009). The best-fit value for  $k_{max}$  is an order of magnitude larger than that reported by Watson et al. (2003) for degradation of acetate with nitrate as a terminal electron acceptor,

but that experiment included multiple reaction pathways in the degradation of toxic phenol whereas the current work used acetate and nitrate as the sole substrates for anaerobic growth.

### 5.3.7 Potential of RBOE as a nitrate sensor

The fluorescent RBOE membrane coated on the quartz sand successfully enabled measurement of the dimensions of the nitrate-depleted plume (Figure 5.3) and provided a reasonable although qualitative estimate of nitrate concentrations and gradients within the plume (Figure 5.4). It is likely that the logarithmic calibration characteristic of the imaging setup used here may be responsible for underestimation of higher nitrate concentrations. Mohr and Wolfbeis (1996) report an ideally linear relationship between fluorescence intensity and nitrate concentration in the range 0.62 - 62 mg L<sup>-1</sup>, suggesting that the rapidly decreasing sensitivity of the image data with increasing nitrate concentration above about 20 mg L<sup>-1</sup> is likely due to detector saturation (Bridge et al., 2006). Photobleaching is considered unlikely for RBOE both due to the short exposure time (cells were not exposed to light during the 5 day incubation period) and the photostable nature of the dye containing ester groups (Mohr and Wolfbeis 1996). Leaching of the dye from the sand coating during the 5-day flow period cannot be discounted, although firstly, the calibration is based on data and image measurements made *in situ* at the end of the experiment, and secondly, the use of a lipophilic dye-PVC membrane combination is chosen in part for its characteristic reduction in the amount of dye leaching (Weidgans et al., 2004).

Subject to these system-specific considerations, which are the subject of further methodological development to optimise both detector sensitivity and dye performance, the RBOE-coated sand nevertheless provides a convenient and potentially sensitive method for monitoring nitrate concentrations during anaerobic biogeochemical reactions in two dimensional porous media systems. This new application mode complements the potential of the RBOE sensor for use in optode and nanoparticle sensors deployable *in situ* in laboratory or field settings (Davis et al., 2005; Mohr and Wolfbeis 1995; McDonagh et al., 2008). Crucially, the application described here enables effectively continuous measurement over 2D spatial domain, rather than point measurements at discrete locations. Our choice of uniform, steady flow approximating a one-dimensional system enabled simplification of the modelling and facilitated comparison between model, analytical and image-derived nitrate concentrations. Although the requirement for a phosphate buffer places some constraint on the range of experiments possible, there is clear potential for use of the RBOE sensor



encapsulated in a membrane coating on a translucent porous medium to monitor nitrate gradients and constrain numerical simulations of denitrification reactions in more complex, non-steady state laboratory systems over time. In this respect it can be added to a growing range of 2D imaging techniques for non-invasive monitoring of, for example, oxygen (Rudolph et al., 2012), pH (Rudolph et al., 2013), colloids (Bridge et al., 2009), microbes (Bottomley et al., 2002) and radionuclides (Corkhill et al., 2013).

## 5.4 Conclusion

We have demonstrated the use of an RBOE nitrate-sensitive membrane sand coating sensor system to monitor spatial gradients in nitrate during anaerobic biodegradation of acetate in which nitrate is employed as a terminal electron acceptor. Chemical and microbiological analyses confirmed that biodegradation of acetate had occurred within the 5-day period of the experiment, and the experimental data showed spatial variations and were fitted using model parameters that were consistent with previous models of biodegrading contaminant plumes. There was good spatial correlation between the plume boundaries predicted by the model and those derived from calibrated image data. Further work is required to optimize the imaging conditions and calibration function for the nitrate-sensitive sensor in application to more complex biogeochemical systems, for example investigating the evolution of denitrifying activity over time and under pulsed flow, or pulsed input conditions more typical of environmental and engineered systems.

**Acknowledgements** HCR and the experiment work were supported by a grant from the UK Biotechnology and Biological Sciences Research Council (BBSRC grant E15832). The authors acknowledge the support of Prof Roger Pickup (CEH Lancaster) and Prof David Lerner (Sheffield) in the origination and development of this work.

## References

- Bottomley, P.J., Yarwood, R.R., Rockhold, M.L., Niemet, M.R., Selker, J.S., 2002. Noninvasive quantitative measurement of bacterial growth in porous media under unsaturated-flow conditions. *Applied and Environmental Microbiology* 68 (7), 3597-3605.
- Bridge, J.W., Banwart, S.A., Heathwaite, A.L., 2006. Noninvasive quantitative measurement of colloid transport in mesoscale porous media using time lapse fluorescence imaging. *Environmental Science & Technology* 40 (19), 5930–5936.
- Bridge, J.W., Heathwaite, A.L., Banwart, S.A., 2009. Measurement of Colloid Mobilization and Redeposition during Drainage in Quartz Sand. *Environmental Science & Technology* 43 (15), 5769–5775.
- Corkhill, C.L., Bridge, J.W., Hillel, P., Gardner, L.J., Banwart, S.A., Hyatt, N.C., 2013. Technetium-99m Transport and Immobilisation in Porous Media: Development of a Novel Nuclear Imaging Technique. In: MRS Proceedings. MATERIALS RESEARCH SOCIETY.
- Davis, F., Collyer, S.D. and Higson, S.P.J. (2005) The construction and operation of anion sensors: Current status and future perspectives. *Anion Sensing* 255, 97-124.
- Don, R.H., Cox, P.T., Wainwright, B.J., Baker, K., Mattick, J.S., 1991. “Touchdown” PCR to circumvent spurious priming during gene amplification. *Nucleic acids research* 19 (14), 4008.
- Eschenbach, W., Well, R., 2011. Online measurement of denitrification rates in aquifer samples by an approach coupling an automated sampling and calibration unit to a membrane inlet mass spectrometry system. *Rapid communications in mass spectrometry*: RCM 25 (14), 1993–2006.
- Gutierrez-Neri, M., Ham, P.A.S., Schotting, R.J. and Lerner, D.N. (2009) Analytical modelling of fringe and core biodegradation in groundwater plumes. *Journal of Contaminant Hydrology* 107(1-2), 1-9.
- Herbert, R.B., 2011. Implications of non-equilibrium transport in heterogeneous reactive barrier systems: evidence from laboratory denitrification experiments. *Journal of contaminant hydrology* 123 (1-2), 30–9.
- Huang, W.E., Oswald, S.E., Lerner, D.N., Smith, C.C., Zheng, C., 2003. Dissolved oxygen imaging in a porous medium to investigate biodegradation in a plume with limited electron acceptor supply. *Environmental science & technology* 37 (9), 1905–11.
- Mastrocicco, M., Colombani, N., Salemi, E., Castaldelli, G., 2011. Reactive Modeling of Denitrification in Soils with Natural and Depleted Organic Matter. *Water, Air, & Soil Pollution* 222 (1-4), 205–215.
- McDonagh, C., Burke, C.S. and MacCraith, B.D. (2008) Optical chemical sensors. *Chemical Reviews* 108(2), 400-422.

- Mohr, G.J. and Wolfbeis, O.S. (1995) Optical Sensing of Anions Via Polarity-Sensitive Dyes - a Bulk Sensor Membrane for Nitrate. *Analytica Chimica Acta* 316(2), 239-246.
- Mohr, G.J., Wolfbeis, O.S., 1996a. Optical nitrite sensor based on a potential-sensitive dye and a nitrite-selective carrier. *The Analyst* 121 (10), 1489.
- Mohr, G.J., Wolfbeis, O.S., 1996b. Effects of the polymer matrix on an optical nitrate sensor based on a polarity-sensitive dye. *Sensors and Actuators B: Chemical* 37 (1-2), 103–109.
- Oates, P.M., Castenson, C., Harvey, C.F., Polz, M., Culligan, P., 2005. Illuminating reactive microbial transport in saturated porous media: demonstration of a visualization method and conceptual transport model. *Journal of contaminant hydrology* 77 (4), 233–45.
- Porter, K.G., Feig, Y.S., 1980. The use of DAPI for identifying and counting aquatic microflora. *Limnology and Oceanography* 25 (5), 943–948.
- Rees, H.C., Oswald, S.E., Banwart, S. a, Pickup, R.W., Lerner, D.N., 2007. Biodegradation processes in a laboratory-scale groundwater contaminant plume assessed by fluorescence imaging and microbial analysis. *Applied and environmental microbiology* 73 (12), 3865–76.
- Rivett, M.O., Buss, S.R., Morgan, P., Smith, J.W.N., Bemment, C.D., 2008. Nitrate attenuation in groundwater: a review of biogeochemical controlling processes. *Water research* 42 (16), 4215–32.
- Rodriguez, G.G., Phipps, D., Ishiguro, K., Ridgway, H.F., 1992. Use of a Fluorescent Redox Probe for Direct Visualization of Actively Respiring Bacteria. *Applied and Environmental Microbiology* 58 (6), 1801.
- Rudolph, N., Esser, H.G., Carminati, A., Moradi, A.B., Hilger, A., Kardjilov, N., Nagl, S., Oswald, S.E., 2012. Dynamic oxygen mapping in the root zone by fluorescence dye imaging combined with neutron radiography. *Journal of Soils and Sediments* 12 (1), 63–74.
- Rudolph, N., Voss, S., Moradi, A.B., Nagl, S., Oswald, S.E., 2013. Spatio-temporal Mapping of Local Soil pH Changes Induced by Roots of Lupin and Soft-rush. *Plant and Soil*. in review.
- Schipper, L.A., Robertson, W.D., Gold, A.J., Jaynes, D.B., Cameron, S.C., 2010. Denitrifying bioreactors—An approach for reducing nitrate loads to receiving waters. *Ecological Engineering* 36 (11), 1532–1543.
- Sinfield, J.V., Fagerman, D., Colic, O., 2010. Evaluation of sensing technologies for on-the-go detection of macro-nutrients in cultivated soils. *Computers and Electronics in Agriculture* 70 (1), 1–18.
- Tanner, C.C., Sukias, J.P.S., Headley, T.R., Yates, C.R., Stott, R., 2012. Constructed wetlands and denitrifying bioreactors for on-site and decentralised wastewater treatment: Comparison of five alternative configurations. *Ecological Engineering* 42 (null), 112–123.

- Thorpe, C.L., Morris, K., Boothman, C., Lloyd, J.R., 2012. Alkaline Fe(III) reduction by a novel alkali-tolerant *Serratia* sp. isolated from surface sediments close to Sellafield nuclear facility, UK. *FEMS microbiology letters* 327 (2), 87–92.
- UNEP, 2012. GEO5: Global Environment Outlook - Environment for the future we want.
- Wakida, F.T., Lerner, D.N., 2005. Non-agricultural sources of groundwater nitrate: a review and case study. *Water research* 39 (1), 3–16.
- Warneke, S., Schipper, L.A., Matiasek, M.G., Scow, K.M., Cameron, S., Bruesewitz, D.A., McDonald, I.R., 2011. Nitrate removal, communities of denitrifiers and adverse effects in different carbon substrates for use in denitrification beds. *Water research* 45 (17), 5463–75.
- Watson, I.A., Oswald, S.E., Mayer, K.U., Wu, Y.X. and Banwart, S.A. (2003) Modeling kinetic processes controlling hydrogen and acetate concentrations in an aquifer-derived microcosm. *Environmental Science & Technology* 37(17), 3910-3919.
- Watson, I. a, Oswald, S.E., Banwart, S. a, Crouch, R.S., Thornton, S.F., 2005. Modeling the dynamics of fermentation and respiratory processes in a groundwater plume of phenolic contaminants interpreted from laboratory- to field-scale. *Environmental science & technology* 39 (22), 8829–39.
- Weidgans, B.M., Krause, C., Klimant, I. and Wolfbeis, O.S. (2004) Fluorescent pH sensors with negligible sensitivity to ionic strength. *Analyst* 129(7), 645-650.
- Winkler, M.-K.H., Kleerebezem, R., van Loosdrecht, M.C.M., 2012. Integration of anammox into the aerobic granular sludge process for main stream wastewater treatment at ambient temperatures. *Water research* 46 (1), 136–44.
- Yoshida, T., 2011. Acetate biodegradation by anaerobic microorganisms at high pH and high calcium concentration. *Journal of environmental radioactivity* 102 (2), 170–7.

## **Chapter 6**

# **General discussion and conclusions**

## 6.1 General remarks

The work presented is a new approach to study the distribution of oxygen and pH *in situ* of an area in order of 1 dm<sup>2</sup>. The described fluorescence foil imaging method is a unique tool to non-invasively map a variety of processes in soils with a time-scale from minutes and hours to weeks. The observed time scale depends on the dynamic behaviour of the biogeochemical parameter of interest. Root exudation for example varies with root age (young roots of lupin tend to acidify their vicinity whereas the older root parts tend to alkalize the rhizosphere), bulk soil properties and show strong spatio-temporal changes. The soil pH in the immediate vicinity of the root surface varied greatly along the root length, with the most acidic point being at 0.6 – 3.4 mm behind the root tip.

After developing the fluorescence dye imaging method to map the changes of oxygen concentration in soil-root systems, we combined it with highly sensitive neutron radiography to monitor the water content distribution of the same sample at nearly the same time (chapter 3). Since the fluorescence imaging approach is two-dimensional and only requires a thin sensor layer, the combination with neutron radiography is feasible because the attenuating effect of the foil is moderate and can be accounted for in the neutron intensity images. The oxygen dynamics in the root-zone developed from local, patchy pattern within the first 2 hours to a diffuse pattern which covers the total sensor foil area. The oxygen depletion could be observed over 48 hours caused by high water saturation and limited supply of oxygen via gas phase. Therefore, the major advantage of this combined approach is that the oxygen dynamics and changing patterns of oxygen depletion and oxygen availability can be interpreted in a more profound and meaningful way. However, the main drawback of neutron radiography is the limited number of neutron beam lines, and thus limited access to beam time and the cost of the infrastructure to operate a suited neutron beam line and imaging system. Nevertheless, for the first time optical fluorescence imaging was successfully coupled with neutron radiography.

We successfully applied the method to soil – root – systems (chapter 3) and to a structured soil (chapter 4). Structured soils are of interest because in finer-grained layers or aggregates soil metabolic activities (essentially transferring O<sub>2</sub> into CO<sub>2</sub>) can decline the oxygen concentrations and oxygen transition zones will result, provided that gas phase re-supply of oxygen is limited. Limited gas phase re-supply appears due to strong rain events or heavy irrigation which can lead to high soil water content. Intense oxygen consumption due to biological activities in soil will also deplete the oxygen reservoir. For the first time we

visualized oxygen depletion in aggregates and layers of fine-grained material with high water holding capacity (chapter 4).

Microbial biodegradation of contaminants in natural and engineered environments is governed by gradients of nutrient and electron acceptor availability which evolve over time in response to water flow, contaminant migration and spatial variations in microbial activity. Another variant of the fluorescence imaging technique was combined with a numerical modeling study (chapter 5) where we used imaging data as input to simulate biodegradation under anaerobic, nitrate-reducing conditions. In two-dimensions, the calibrated image data and the modeled plume dimensions agreed qualitatively very well although we found indications that the image data tended to underpredict nitrate concentrations as they increased to the background level. This would serve to enhance any potential effects of variations in optical transmissivity of the sand or of any leaching or photobleaching of the dye.

## **6.2 Evaluation of the fluorescence imaging method**

Special fluorescent dyes are the basis for sensor foil production. A great advantage of fluorescence imaging is the broad range of adaptability. Published results include sensors sensitive to metal ions or to changes in temperature, nitrate, glucose, potassium, carbon dioxide (Carofiglio et al. 2006, Mohr & Wolfbeis 1995, Schröder et al. 2007a, Thibon & Pierre 2009). Besides oxygen and pH, temperature, glucose or CO<sub>2</sub> gradients are other important biogeochemical parameters which could be imaged in porous media. This offers assessment of soil structure, sediments, roots and microbes. Moreover, due to a simple experimental set up and a high mobility, the fluorescence imaging technique has the great advantage of combining it with other techniques (see chapter 3 & 4). Nevertheless, the method can be used for example in rhizothrons to study the dynamic behaviour of root exudation and root respiration for different plant species and plant ages. Rhizothrons are usually tiltable that forces the roots to grow along the walls which makes the root system visible without neutron radiography.

Our imaging approach is based on the measurements of the fluorescence intensity. The advantage of this approach is the simple and inexpensive instrumentation (camera, filters and lamps). Spatial resolution of down to 200 µm can be achieved while covering an area of about 100cm<sup>2</sup> in each image which is obtained within only a few seconds. Moreover, intensity based measurements offer the possibility to map different parameters since there are various sensor dyes available (Stich et al. 2010). The drawbacks of intensity based imaging include limited photostability of the indicator dyes (Schröder et al. 2007b). The choice of the fluorescent dye

influences the photostability, for example metalloporphyrins dyes with fluoro-substituents typically show increased photostability (Schröder et al. 2007b). Nevertheless, it is essential to cover the plant container because photobleaching can be reduced and the root growth is not constrained. Inaccuracies may also arise from camera drift (Borisov et al. 2006) or non-homogeneous lighting (Liebsch et al. 2000). Camera drift can be reduced by using a cooled camera system where the chip is cooled to  $-15^{\circ}\text{C}$  or less to avoid thermal noise to a large degree. The examples show that the choice of the imaging setup and the sensor dyes are the most important steps in fluorescence foil imaging.

In comparison, lifetime based measurements need special cameras (acquisition time in the  $\mu\text{s}$  range) and read out devices (fiber optics) which makes the lifetime based measurements expensive. Additionally lifetime sensing is limited due to the number of indicator that possesses long fluorescence lifetimes (Stich et al. 2010). Nevertheless, lifetime based measurements are self-referenced and independent of the intensity of the excitation light (Baleizao et al. 2008), therefore have the strong advantage of being more independent of spatial or temporal changes of the dye and foil material. Both methods, intensity and lifetime based imaging have one major drawback. Since the  $pO_2$  is measured via the sensor dye we cannot distinguish between dissolved oxygen present in the water phase and gaseous oxygen. However, by means of Henry's Law we can calculate the concentration of dissolved oxygen from the partial pressure. The pH is defined as the negative decadal logarithm of the activity of hydronium ions in solution. Comparable to other pH measurement our fluorescence imaging methods needs at least partial liquid phase to facilitate interchange of  $\text{H}^+$ . pH can thus only be measured if a water phase is present. In our experiments we were able to detect pH changes with local water contents down to 5% in a sandy soil.

Possible errors can result from sensor foil production. The dye with corresponding solvents and matrices should be stirred overnight to guarantee that all particles are dissolved and the sensor cocktail is homogeneous. Moreover, the knife-coating device should be placed onto a flat table to prevent variations in sensor foil thickness. For quality reasons and to ensure a constant thickness of the sensor foil we measure the thickness with a disk micrometer.

Besides simple, inexpensive instrumentation and high flexibility our method offers the possibility to use a variety of soil matrices. The dynamic oxygen imaging can be conducted starting from sandy soils to loamy soils. We performed experiments with a sandy soil with low organic carbon content as well as soils with high clay contents which are under agricultural use. The dynamic pH imaging was proved to be effective in sandy matrix. This



should also apply to non sandy soil material, but with some limitations on dynamic range and accuracy. However, this setup needs to be tested.

## 6.3 Outlook

### 6.3.1 Sensor Improvements

The fluorescence imaging methods presented in this thesis proved to be a valuable non-invasive tool for measuring the concentration of oxygen and the pH values. The ongoing development of optical sensors offers the opportunity to map other parameters in the future, e.g. temperature, CO<sub>2</sub> or glucose. To improve the developed fluorescence imaging method the most crucial considerations are:

- I. **Signal enhancement:** Signal enhancement is one of the major tasks in sensor improvement. Reasons are the need to improve the signal-to-noise ratio, to minimize the influence of the background fluorescence, to reduce the thickness of the sensing film, and to apply simple readout systems (Mayr et al. 2009). An additional reflective layer made of titanium dioxide dissolved in silicone can act as scattering area to increase intensity of the luminescence collected in the oxygen sensing layer (Baleizao et al. 2008). Alternatively, light harvesting can be the method of choice to increase signal intensity. Light harvesting amplifies the signal intensity by the addition of antenna dyes with a higher brightness (Mayr et al. 2009). In addition to signal enhancement, light harvesting can extend the Stokes' shift and facilitate the separation of excitation and emission light (Mayr et al. 2009).
- II. **Multisensor systems:** Chemical multisensory cannot be constructed by simply mixing the respective sensor chemistries due to several problems: (i) many indicators display broad absorption and emission bands that often overlap and unambiguous assignment is difficult; (ii) if two luminescence probes are located in close proximity, fluorescence resonance energy transfer can occur which is highly undesirable (Stich et al. 2010). Indicators incorporated into nano- or microparticles can overcome these problems. Up to date, several kinds of dual sensors have been introduced and generally based on lifetime measurements, e.g. O<sub>2</sub>/temperature, O<sub>2</sub>/pH, O<sub>2</sub>/CO<sub>2</sub>. Triple sensors include monitoring of glucose, oxygen and temperature or of pH, oxygen and temperature (Stich et al. 2010). Recently, for the first time a quadruple sensor was presented, able to monitor oxygen concentrations, CO<sub>2</sub>, pH and temperature simultaneously (Borisov et al. 2011).

However, these suggested improvements require advanced knowledge in chemical synthesis of multiple fluorescent foils and the sensing and imaging remains a challenging task. Additionally the determination of lifetimes in the ns range involves more sophisticated instrumentation. The compatibility and mutual solubility of dyes and polymers and the need for unambiguously separating optical signals are only two critical aspects (Stich et al. 2010).

### **6.3.2 Applications currently tested**

The combination with highly sensitive neutron radiography enabled us to simultaneously determine two or more parameters of interest. An essential feature is the high flexibility and the capability to link the fluorescence imaging method to other disciplines and analysis methods. The prospering use of our developed fluorescence imaging method is exemplified by the following ongoing pilot studies:

1. We recently combined fluorescence foil imaging with matrix-assisted laser desorption ionization imaging mass spectrometry (MALDI). Here we can gain insights into the degradation of the commonly used fungicide metalaxyl at the root surface in the rhizosphere of white lupine. Preliminary results indicate that oxygen concentration is a crucial point. Metalaxyl concentration mapped at the root surface of secondary roots increases with decreasing oxygen concentration. We did not detect a pH decrease in the vicinity of the roots caused by the acid metabolite that is the first degradation product of metalaxyl. In a next step we will couple local pH and oxygen dynamics given by fluorescence imaging with neutron radiography and metabolite analysis (MALDI). We hope to understand the complex interplay of root density, water content distribution, root exudation, root respiration and metalaxyl degradation in a single root system.
2. We coupled fluorescence imaging with gas chromatography (GC) analysis to gain insights into the biodegradation of chitin and the involved pattern of oxygen depletion. The preliminary results indicate that the fluorescence imaging set up is appropriate to map microbial induced oxygen consumption under variable saturated conditions. Under water saturated conditions the oxygen sensor seems to be more sensitive compared to the results measured with gas chromatography: the sensor foil shows oxygen depletion within the porous matrix whereas the headspace GC measurements still indicate oxygen concentration around 19 %. The reason is the reduced oxygen transfer from the water to the gas phase. We aim to

visualize oxic and anoxic micro-zones at the mm scale and relate this pattern to microbial community analysis. We will relate the patchy structure of oxygen availability to chitinolytic bacteria in soil-like matrices.

3. Our oxygen sensing foils are used to study the oxygen distribution in streambed profiles. The aim was to get insights into the interactions of groundwater and surface water. The oxygen sensitive foils are glue onto Plexiglas tubes and inserted into the streambed. Because of limited space in the tubes the approach is to measure the fluorescence lifetime instead of the fluorescence intensity. A conventional fibre-optic oxygen meter (PreSens GmbH) was used for measuring  $pO_2$  profiles across the streambed.

## 6.4 Synthesis

The systematic structural characterisation and functional exploration of biogeochemical interfaces in soils have been identified as emerging challenge in soil science (Totsche et al., 2010). We established a non-invasive fluorescence imaging technique to directly quantify the distribution and changes of oxygen, pH and the water content distribution. This imaging setup can help to clarify the formation and architecture of interfaces induced by oxygen consumption, pH changes and water content distribution. The formation of interfaces at the plant root – soil interface but also interfaces formed by the interaction of soil structure, oxygen consumption and water content can be monitored. The distinctive strength is the high flexibility and the capability to link the fluorescence imaging method to other disciplines and analysis methods.

## References:

- Baleizao C, Nagl S, Schaferling M, Berberan-Santos MN, Wolfbeis OS (2008): Dual fluorescence sensor for trace oxygen and temperature with unmatched range and sensitivity. *Anal Chem* 80, 6449-6457
- Borisov SM, Vasylevska AS, Krause C, Wolfbeis OS (2006): Composite luminescent material for dual sensing of oxygen and temperature. *Advanced Functional Materials* 16, 1536-1542
- Borisov SM, Seifner R, Klimant I (2011): A novel planar optical sensor for simultaneous monitoring of oxygen, carbon dioxide, pH and temperature. *Anal Bioanal Chem* 400, 2463-2474
- Carofiglio T, Fregonese C, Mohr GJ, Rastrelli F, Tonellato U (2006): Optical sensor arrays: one-pot, multiparallel synthesis and cellulose immobilization of pH and metal ion sensitive azo-dyes. *Tetrahedron* 62, 1502-1507
- Liebsch G, Klimant I, Frank B, Holst G, Wolfbeis OS (2000): Luminescence lifetime imaging of oxygen, pH, and carbon dioxide distribution using optical sensors. *Applied Spectroscopy* 54, 548-559
- Mayr T, Borisov SM, Abel T, Enko B, Waich K, Mistlberger G, Klimant I (2009): Light Harvesting as a Simple and Versatile Way to Enhance Brightness of Luminescent Sensors. *Anal Chem* 81, 6541-6545
- Mohr GJ, Wolfbeis OS (1995): Optical Sensing of Anions Via Polarity-Sensitive Dyes - a Bulk Sensor Membrane for Nitrate. *Anal Chim Acta* 316, 239-246
- Schröder CR, Neurauder G, Klimant I (2007a): Luminescent dual sensor for time-resolved imaging of pCO<sub>2</sub> and pO<sub>2</sub> in aquatic systems. *Microchimia Acta* 158, 205-218
- Schröder CR, Polerecky L, Klimant I (2007b): Time-resolved pH/pO<sub>2</sub> mapping with luminescent hybrid sensors. *Anal Chem* 79, 60-70
- Stich MIJ, Fischer LH, Wolfbeis OS (2010): Multiple fluorescent chemical sensing and imaging. *Chem Soc Rev* 39, 3102-3114
- Thibon A, Pierre VC (2009): A Highly Selective Luminescent Sensor for the Time-Gated Detection of Potassium. *J Am Chem Soc* 131, 434-+
- Totsche KU, Rennert T, Gerzabek MH, Kogel-Knabner I, Smalla K, Spiteller M, Vogel HJ (2010): Biogeochemical interfaces in soil: The interdisciplinary challenge for soil science. *J Plant Nutr Soil Sc* 173, 88-99

# Supporting information for Plant & Soil article on Spatio-temporal Mapping of Local Soil pH Changes Induced by Roots of Lupin and Soft-rush

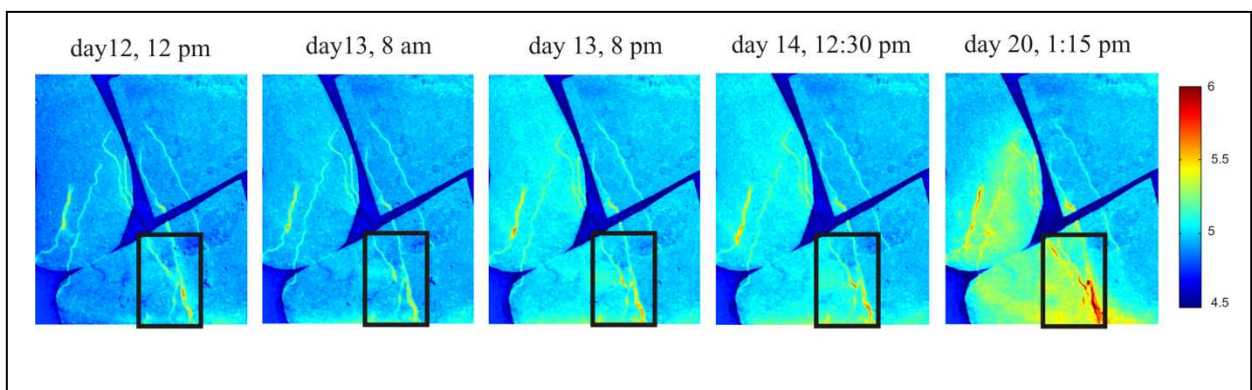


Figure S1: Time series of pH distribution during root growth in containers planted with soft-rush. Constantly dark blue areas result from gaps between fluorescence emitting foil patches and pH cannot be evaluated there. The black rectangle outlines the zoom region shown in Fig. 4 of the main article.

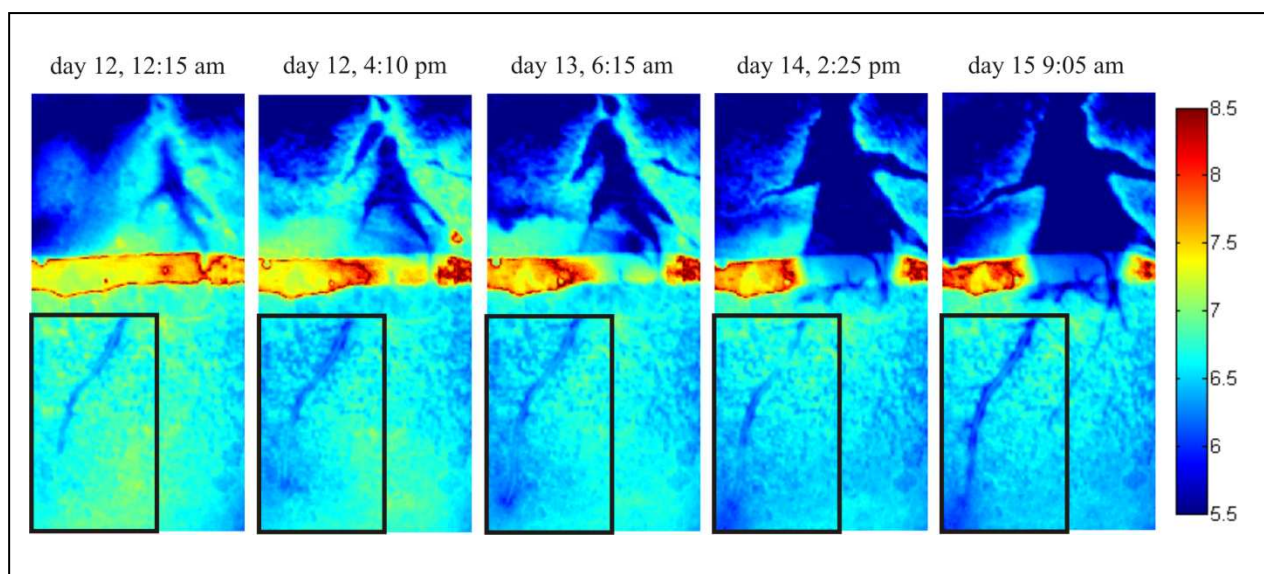


Figure S2: Time series of pH distribution during root growth in containers planted with white lupin. Color coding represent calibrated pH values for sand material. In the centre there is a horizontal layer of fine material, white color and high water saturation; there the pH calibration is not strictly valid and thus yellow and red color does not indicate a basic pH. Nevertheless, also there relative changes with time are detectable and show an acidification from days 12 to day 15 in its centre where most roots are located.

Table T1: Effects of soft-rush and two lupine species on rhizosphere and bulk soil pH.

<b>Plant species</b>	<b>Mean pH rhizosphere</b>	<b>Mean pH bulk soil</b>
<i>J. effusus</i>	$5.98 \pm 0.09$	$4.83 \pm 0.12$
	$5.82 \pm 0.22$	$4.83 \pm 0.04$
	$5.92 \pm 0.05$	$4.83 \pm 0.04$
<i>L. albus</i>	$6.36 \pm 0.07$	$6.69 \pm 0.10$
	$6.38 \pm 0.09$	$6.62 \pm 0.13$
<i>L. angustifolius</i>	$6.39 \pm 0.24$	$6.77 \pm 0.21$
	$6.53 \pm 0.07$	$6.69 \pm 0.24$

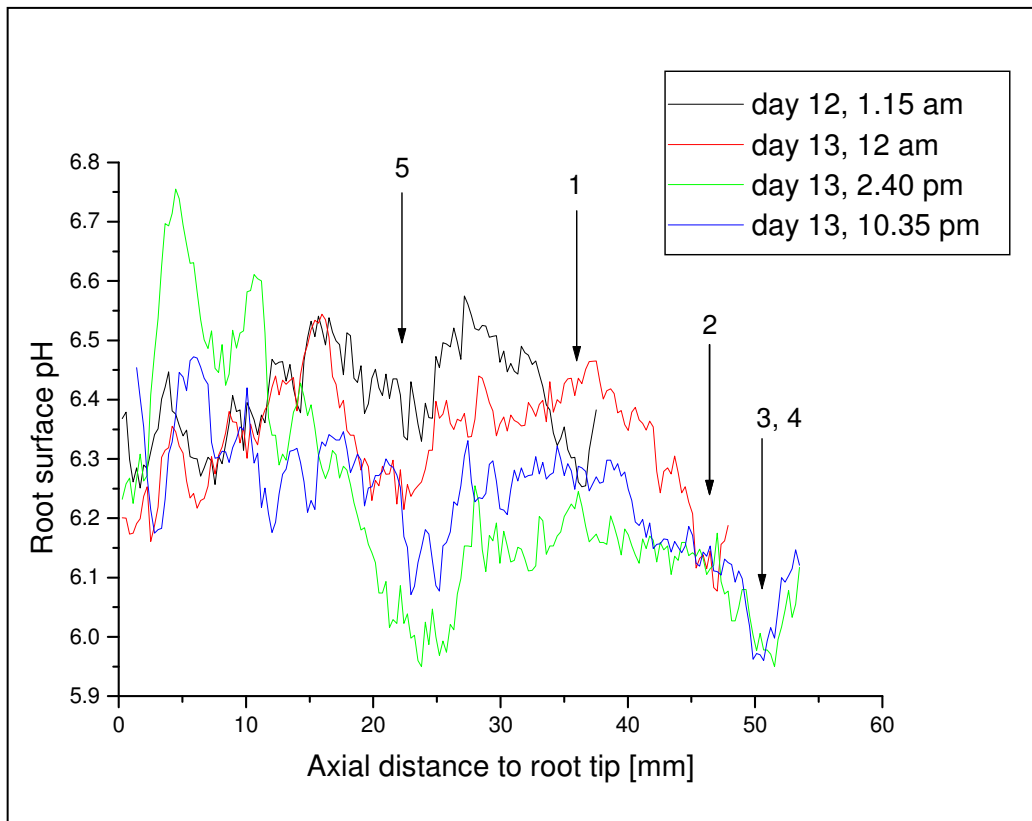


Figure S3: Time series of pH profile along the growing tap root for white lupin over a course of 46 h. The profiles show pH as a function of axial distance from branching point in the direction of the growing root tip. The root tip is proceeding downward from distances of around 38 mm distance to 56 mm. The vertical arrows 1 – 4 indicate the area just behind the root tip whereas arrow 5 indicates a newly branching root. The profiles were captured by tracking the root surface pH along the root axis starting from the branching point and represent measurements at every 0.28 mm distance.

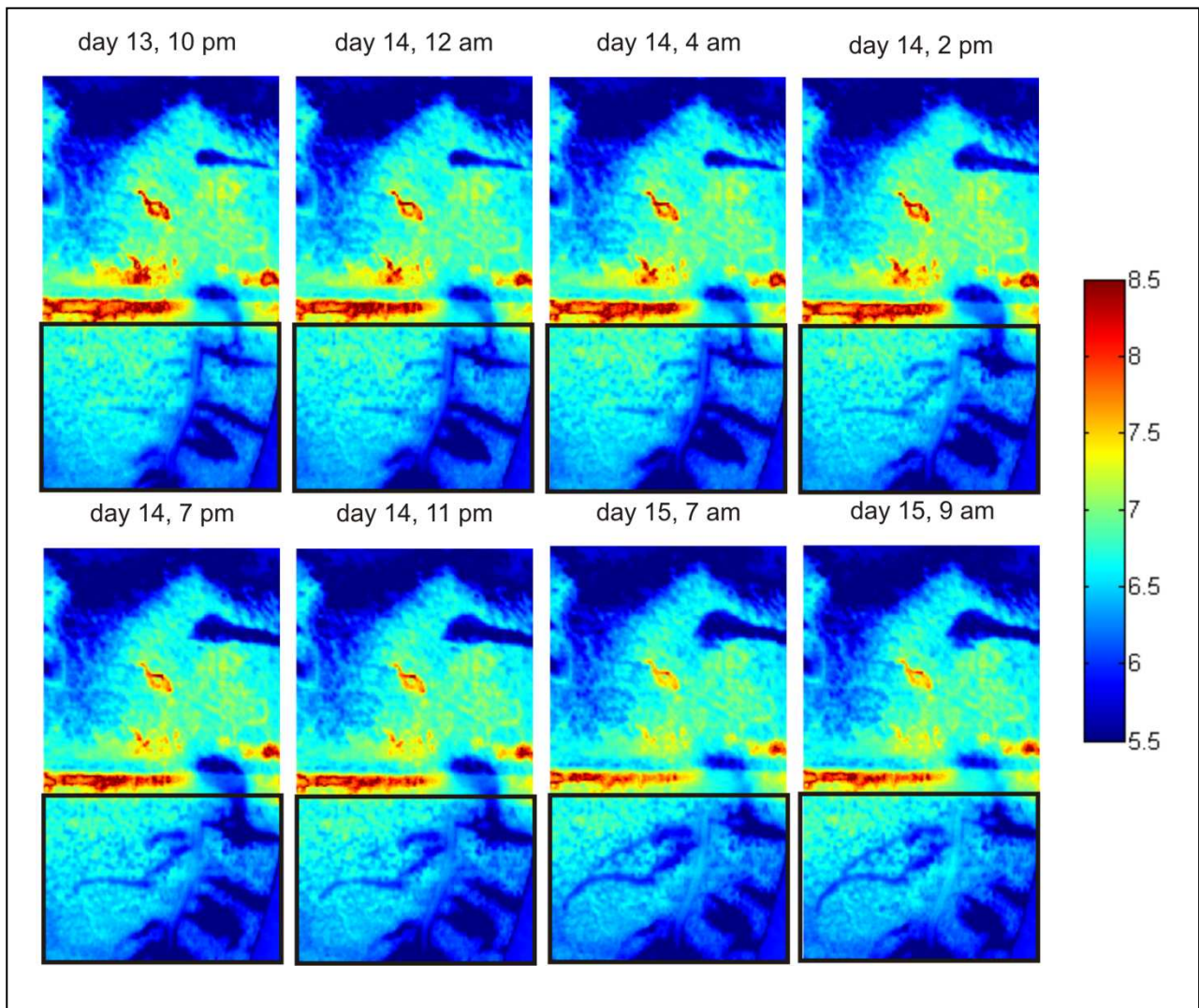


Figure S4: Time series of pH distribution in the container with a narrow-leaved lupin. Color coding represent calibrated pH values for sand material. In the centre there is a horizontal layer of fine material, white color and high water saturation; there the pH calibration is not strictly valid and thus yellow and red color does not indicate a basic pH. Nevertheless, also there relative changes with time are detectable and show a varying acidification from days 13 to day 15 in its centre where most roots are located. The black rectangle outlines the zoom region shown in Fig. 6 of the main article.



# Curriculum Vitae

Name	Nicole Rudolph-Mohr, born Rudolph
Address	Mühlenstr. 3, 14482 Potsdam
Email	nrudolph@uni-potsdam.de
1980	Born 29 February in Belzig
1986-1992	Elementary School, Niemegek
1992-1999	Secondary School „Gymnasium am Burgwall“ Treuenbritzen, Abitur
1999-2007	Academic studies in Environmental Engineering, Technical University of Berlin, Thesis: Influence of the complexation of paramagnetic cations by organic ligands on the proton relaxation time of water, first degree as Dipl.-Ing.
2008-2009	PhD student within the SPP 1315 “Biogeochemical Interfaces in Soils”, Institute of Earth and Environmental Science, Helmholtz Centre for Environmental Research, Leipzig
2010-2011	PhD student within the SPP 1315 “Biogeochemical Interfaces in Soils”, Institute of Earth and Environmental Science, University of Potsdam
2012-2013	Research assistant within the second phase of DFG-SPP 1315 “Biogeochemical Interfaces in Soils” Institute of Earth and Environmental Science, University of Potsdam

# Danksagung

Writing this PhD thesis was not only the work of myself, there were other persons involved in this project, supporting me in the one or other way. I would thank all of them. Especially I thank ...

- Sascha Oswald who gave me the opportunity and freedom to work on a very interesting scientific question, for the discussions, and specially for the big work to review my thesis and supporting me in publishing the papers.
- Ahmad Moradi and Andrea Carminati for scientific discussions, for the efforts in reviewing the papers of my thesis and for being supportive office mates and friends
- The participants of the SPP 1315 “Biogeochemical interfaces in Soils” for interesting discussions, promising collaborations, and for giving me the opportunity to test the developed imaging method in different research disciplines
- Hanna Esser for her support during several neutron experiments and her help to not become crazy during that time
- Andre Hilger, Nikolay Kardijlov, Eberhard Lehmann and Peter Vontobel for showing me the big world of neutron imaging and for their technical help during the neutron experiments
- Stefan Nagl for his support and his knowledge about sensor foils